# INTERFACIAL MOMENTUM AND MASS TRANSFER IN TWO-PHASE FLOWS

by

Ashwanth Kumar Reddy Salibindla

A dissertation submitted to The Johns Hopkins University in conformity with the requirements for the degree of Doctor of Philosophy.

Baltimore, Maryland

July, 2020

# Abstract

The process by which a mixture of fluids of different phases transfer mass and momentum across a deformable interface constitutes one of the most basic multi-phase flow problems that occur in many natural and industrial applications. However, a lack of consistent experimental framework to resolve this complex interplay between two fluid phases at different length and time scales severely limits our understanding of this problem. This is in part due to the inadequacy of applying classical experimental facilities designed for single-phase flows directly to two-phase flows as well as the limit of many existing diagnostic systems. Therefore, the goal of this thesis is to provide an experimental framework that consists of two key components: experimental apparatus that can isolate the momentum and mass transfer between two phases and diagnostic systems that can probe these parameters. In addition, to cover different flow regimes, two types of multi-phase flows will be introduced and each one will come with its own apparatus and diagnostic system.

The first part of this thesis focuses on the momentum transfer between gas

bubbles and surrounding turbulence, which is an unclosed term in the two-fluid model. Most previous work assumes spherical bubbles with idealized drag, lift, and added mass forces, even though gas bubbles could be deformed by surrounding turbulence, exhibiting different momentum transfer between the two phases and ultimately modulating the macro-scale spatial distribution of bubbles and their mean rise velocity. By leveraging this inherent connection between the interfacial and macro-scale quantities, we develop a method to determine the drag and lift forces of bubbles in turbulence by measuring the bubble rise velocity, which shows a dramatic change in turbulence that was thought to be impossible. This dramatic change is later connected to the changes in both lift and drag forced modulated by turbulence-induced deformation.

In addition, after determining the lift and drag coefficients of deformable bubbles, we have also successfully measured the added-mass force, which is an unsteady force that contributes significantly to the random motion of bubbles in turbulence. It is well known that this force is sensitive to the geometrical information, such as the shape and orientation of an object, in turbulence. Given the complexity of these two quantities in turbulence, this coefficient is often assumed to be impractical to measure. By following the same framework and constraining it using macro-scale bubble acceleration variance, we showed that the added mass coefficient should gradually drop as the bubble aspect ratio increases due to the preferential alignment of the slip acceleration between the

two phases and the bubble major axis.

The second multi-phase flow problem is in the opposite limit where the liquid-liquid two-phase flows mix together through Rayleigh-Darcy convective instability in a Hele-Shaw cell, which is motivated primarily by the geological sequestration of anthropogenic $CO_2$. In particular, we use a surrogate system to investigate how the layered heterogeneity and anisotropy found in underground saline aquifers affect the mass transfer rate between the two phases, $CO_2$ and brine. Due to the density and refractive-index mismatch between the two phases, the shadowgraph technique was used to obtain 2D quantitative measurements of the mixing efficiency. Surprisingly, a 10% reduction in bulk permeability resulted in as much as 80% reduction in the mixing efficiency. Based on the experimental results, a model was developed to predict this behavior of two-phase mass transfer on the properties of heterogeneity.

**Primary Reader and Advisor:** Dr. Rui Ni

**Secondary Readers:** Dr. Joseph Katz & Dr. Rajat Mittal

# Acknowledgments

If I recall the first meeting with my advisor (Dr. Rui Ni) back in February 2015, it was a time when I was pursuing a Master of Science degree and very anxious about finding a thesis advisor. A week after our meeting, I was elated to receive an email from Rui extending an offer to join his lab as a Ph.D. student, that I accepted without much hesitation. Thus, began my journey towards achieving a doctorate degree. I will always remember the words that Rui had said during our first meeting, "you will be working with me rather than for me and we are in this long journey together". They left a profound impression on me and set the tone for the next five years of my Ph.D., that I have thoroughly enjoyed.

I realize that the completion of my thesis was only possible due to significant contributions and great support that I have received from many people over the past five years. Here, I would like to thank a few in particular.

ACKNOWLEDGMENTS

Rui, thank you for your constant support and guidance during this journey, especially during the times when I felt lost and needed your supervision. I admire your ability to always be involved and constantly help me to push myself, bringing out the best of my potential. I have learnt a lot from you, particularly on how to think like a researcher and communicate scientific ideas. You have been an ideal advisor and thank you for creating such a great work environment.

I want to specially thank Ashik Masuk, who has been a fellow colleague and a close friend throughout my Ph.D. We have had a unique journey together from joining the lab as the first Ph.D. students, to switching universities halfway through our Ph.D. I will always cherish our intellectual and emotional discussions. You have been a constant support system that I could always rely on.

I also want to thank all my fellow colleagues at Penn State: Shiyong Tan, Jikang Shen, Gökhan Akarsalan, Zeynep Kaymak, Morgan Austin and Kristov George, and my colleagues at Johns Hopkins: Yinghe Qi, Juan Sebastian Rubio Lopez, Xu Xu and Taehoon Kim for your help with constructing and perfecting the experimental setups, writing data processing codes, performing data analysis and all the intellectual discussions that have played a substantial role in the current work. I would also like to extend my thanks to the undergraduate students: Rabin Subedi, Chee Hau Teoh, Jhi Loke Yong, Victor Shen,

ACKNOWLEDGMENTS

Shashank Shiva and Dongru Chen who have helped me in conducting tedious experiments and data analysis.

Finally and most importantly, I want to thank my mother, Elizabeth Salibindla, my father, Jaipaul Salibindla, and my sister, Swetha Boyapati. You have been very supportive and encouraging throughout my education and I am really fortunate to be loved so dearly.

# Contents

# List of Tables

# List of Figures

# Chapter 1

# Introduction

Two-phase flows typically come in various combinations of the three fundamental phases. They are ubiquitous in many natural and industrial systems. Some examples include industrial flows like fluidized beds (solid-gas; Rüdisüli et al. (2012)) and bubble columns in reactors (gas-liquid; Besagni, Inzoli, and Ziegenhein (2018)), or natural flows like sediment transport in rivers (solid-liquid; Merritt, Letcher, and Jakeman (2003)) and oil spills in the ocean (liquid-liquid; Gong et al. (2014)). Such two-phase flows are common and well-studied, yet predicting their behavior remains difficult. Developing such predictive models for real-world applications requires a thorough understanding of the physics involved and validation through experimental evidence. Our goal is to improve these analyses by making models constrained by reliable experimental data. Therefore, in the current work, we perform experiments to

explore two multi-phase flow systems including, (i) the dynamics of a gas-liquid system, where finite-sized deformable air bubbles are dispersed in turbulent water, and (ii) mass transfer in a liquid-liquid system, where water and propylene glycol (PPG) mix together via dissolution-driven convection in a porous medium.

Modeling two-phase systems, such as the ones described above, is more difficult than modeling single-phase systems due to the complex non-linear interactions between the two phases. Two-phase flows introduce additional terms in the average macroscopic conservation of the mass, momentum, and energy equations to account for the interfacial transfer of these fundamental quantities. Based on the derivations from Ishii and Mishima (1984) and Enwald, Peirano, and Almstedt (1996), if one ignores the surface tension, the averaged conservation equations of mass and momentum for phase $k$ takes the form

Mass conservation:

$$\frac{\partial}{\partial t}(\alpha_k \rho_k) + \nabla \cdot (\alpha_k \rho_k \mathbf{u}_k) = \dot{\Gamma}_k \tag{1.1}$$

$$\sum_{k=1}^{2} \dot{\Gamma}_k = 0 \tag{1.2}$$

| **Variable** | **Non-dimensional form** |
|---|---|
| Length | $\nabla^* = \nabla \times L$ |
| Velocity | $\mathbf{u}_k^* = \mathbf{u}_k/U$ |
| Time | $t^* = t/(L/U)$ |
| Density | $\rho_k^* = \rho_k/\langle\rho_k\rangle$ |
| Gravity | $\mathbf{g} = \hat{\mathbf{g}}/g$ |
| Stress | $\overline{\overline{\mathbf{T}}}_k^{Re} = \overline{\overline{\mathbf{T}^*}}_k^{Re}/(\langle\rho_k\rangle U^2)$, $\overline{\overline{\mathbf{T}}}_k = \overline{\overline{\mathbf{T}^*}}_k/(\langle\rho_k\rangle U^2)$ |
| Mass generation | $\dot{\Gamma}_k^* = \dot{\Gamma}_k/(\langle\rho_k\rangle L/U)$ |
| Interfacial momentum transfer | $\mathbf{M}^*{}_{k\mathbf{I}} = \mathbf{M}_{k\mathbf{I}}/(\langle\rho_k\rangle U^2/L)$ |

**Table 1.1:** Non-dimensionalized variables for mass and momentum conservation equations in two-phase flows

Momentum conservation:

$$\frac{\partial}{\partial t}(\alpha_k\rho_k\mathbf{u}_k) + \nabla\cdot(\alpha_k\rho_k\mathbf{u}_k\mathbf{u}_k) = \nabla\cdot(\alpha_k(\overline{\overline{\mathbf{T}}}_k + \overline{\overline{\mathbf{T}}}_k^{Re})) + \alpha_k\rho_k\mathbf{g} + \mathbf{M}_{k\mathbf{I}} \tag{1.3}$$

$$\mathbf{M}_{k\mathbf{I}} = -\langle\overline{\overline{\mathbf{T}}}\cdot\nabla X_k\rangle \tag{1.4}$$

Here, $\alpha_k$ is the average phase indicator function; $X_k$ is the phase indicator function; $\rho_k$, the density of phase $k$; $\dot{\Gamma}_k$, the mass generation rate per unit volume of phase $k$, which becomes important when the fluids are miscible but can be ignored otherwise; $\mathbf{u}_k$ is the mass-averaged phase velocity; $\overline{\overline{\mathbf{T}}}_k$ and $\overline{\overline{\mathbf{T}}}_k^{Re}$ are the average and fluctuating Reynolds stress tensors; and $\mathbf{M}_{k\mathbf{I}}$ is the interfacial momentum transfer term.

Using appropriate non-dimentionalization from table 1.1, the two conservation equations can be rewritten as

$$\frac{\partial}{\partial t^*}(\alpha_k \rho_k^*) + \nabla^* \cdot (\alpha_k \rho_k^* \mathbf{u}_k^*) = \dot{\Gamma}_k^* \tag{1.5}$$

$$\frac{\partial}{\partial t^*}(\alpha_k \rho_k^* \mathbf{u}_k^*) + \nabla^* \cdot (\alpha_k \rho_k^* \mathbf{u}_k^* \mathbf{u}_k^*) = \frac{1}{Re} \nabla^* \cdot (\alpha_k (\overline{\overline{\mathbf{T}^*}}_k + \overline{\overline{\mathbf{T}^*}}_k^{Re})) + \frac{1}{Fr^2} \alpha_k \rho_k^* \hat{\mathbf{g}} + \mathbf{M^*}_{k\mathbf{I}} \tag{1.6}$$

where, $Re = \langle \rho_k \rangle UL/\mu_k$ is the Reynolds number and $Fr = U/\sqrt{gL}$ is the Froude number.

Closure models are often needed in order to make the two unclosed interfacial exchange terms in equations 1.5 and 1.6 solvable. Developing realistic closure models is a key challenge. With this in mind, we develop models backed by experimental evidence for two such systems. In one system, gas bubbles rise in turbulent water, where momentum transfers between the two fluids ($Re \gg 1$) without much mass transfer. In the second system, water and propylene glycol mix together in a porous medium, where the mass transfer between the fluids is important but the momentum exchange can be ignored ($Re \ll 1$).

## IMMISCIBLE TWO-PHASE FLOWS IN TURBULENT MEDIUM

In the limit when the inertial force dominates the viscous force, which is the case in turbulent environments, $Re \gg 1$, equation 1.6 becomes

$$\frac{\partial}{\partial t^*}(\alpha_k \rho_k^* \mathbf{u}_k^*) + \nabla^* \cdot (\alpha_k \rho_k^* \mathbf{u}_k^* \mathbf{u}_k^*) - \frac{1}{Fr^2}\alpha_k \rho_k^* \hat{\mathbf{g}} = \mathbf{M}^*{}_{k\mathbf{I}} \tag{1.7}$$

Equation 1.7 demonstrates that the interfacial momentum transfer term cannot be ignored and plays an important role in determining the overall flow dynamics. For the particular case of dispersed two-phase flows, Ishii and Mishima (1984) and Enwald, Peirano, and Almstedt (1996) expanded this term, neglecting the stress fluctuations and instead taking the interfacially averaged pressure and stress of phase $k$, to give

$$\mathbf{M}_{k\mathbf{I}}^d = n_p(\mathbf{F}_D + \mathbf{F}_L + \mathbf{F}_{AM} + \mathbf{F}_B + \mathbf{F}_{Ot}) \tag{1.8}$$

Here, $\mathbf{F}_D$, $\mathbf{F}_L$, $\mathbf{F}_{AM}$, $\mathbf{F}_B$ and $\mathbf{F}_{Ot}$ are the drag, transverse lift, added-mass, Basset history and other forces respectively acting on a single particle and $n_p$ is the number of particles per unit volume of the flow.

Subsequently, using a Lagrangian framework and following the dispersed particle, Magnaudet and Eames (2000) built upon equation 1.8 and proposed a governing force balance equation for finite-sized bubbles as:

$$\mathbf{F}_b = V_b(\rho_b)\frac{D\mathbf{u}_b}{Dt} = \mathbf{F}_D + \mathbf{F}_L + \mathbf{F}_{AM} + \mathbf{F}_g + \mathbf{F}_P + \mathbf{F}_B$$
$$= \frac{\rho_l}{2}AC_D(\mathbf{u}_l - \mathbf{u}_b)|\mathbf{u}_l - \mathbf{u}_b| + \rho_l C_L(\mathbf{u}_l - \mathbf{u}_b) \times (\nabla \times \mathbf{u}_l) + \rho_l V_b C_A(\frac{D\mathbf{u}_l}{Dt} - \frac{D\mathbf{u}_b}{Dt})$$
$$+V_b(\rho_l - \rho_b)g\hat{\mathbf{e}}_z - \frac{1}{2}V_b\nabla P_w + 6(D/2)^2\sqrt{\pi\rho_l\mu_l}\int_0^t \frac{\left(\frac{D\mathbf{u}_l}{Dt} - \frac{D\mathbf{u}_b}{Dt}\right)}{\sqrt{(t-\tau)}}\mathrm{d}\tau \tag{1.9}$$

Here, the phase subscripts $k = 1\ \&\ 2$ for liquid water and air bubbles are replaced by $l$ and $b$ respectively. Thereby, $\rho_l$ and $\rho_b$ are the density of water and air, respectively; $\mu_l$ is the dynamic viscosity of water; $g$, the gravitational constant; $V_b$ is bubble volume; $A$ is the projected area of a sphere with an equivalent volume of the bubble of diameter $D$; $\mathbf{u}_b$ and $\mathbf{u}_l$ are the velocity of the bubble and unperturbed ambient water taken at the centre of the bubble; similarly, $\frac{D\mathbf{u}_b}{Dt}$ and $\frac{D\mathbf{u}_l}{Dt}$ are the material accelerations of the bubble and surrounding water.

It is important to note that due to the interfacial averaging of stresses, the model introduces three closure parameters. Namely, the drag ($C_D$), lift ($C_L$), and added-mass ($C_A$) coefficients. Consequently, it is imperative to probe the three coefficients in order to solve equation 1.9 and determine the phase interactions. Historically, these closure parameters were found to depend on measurable quantities of the flow. These include the particle's shape, size, orientation, void fraction, and particle based Reynolds number ($Re_b = \frac{\rho_l|\mathbf{u}_b - \mathbf{u}_l|D}{\mu_l}$).

However, it is usually very difficult to reliably measure all of these quantities for two-phase flows due to considerable challenges in experimentats.

Determining the model coefficients becomes particularly challenging for finite-sized deformable bubbles in turbulence subject to strong fluctuations, where the bubble shape and orientation are coupled with the surrounding flows. In such conditions, additional quantities like the Eötvös ($Eo = \frac{\rho_l g D^2}{\sigma}$) and Weber ($We = \frac{\rho u'^2 D}{\sigma}$) numbers that determine the bubble deformability due to buoyancy and surrounding flow inertia respectively were found to be of supreme importance; here, $\sigma$ corresponds to the surface tension between air and water and $u'$ is the turbulence fluctuation velocity. In such cases, however, due to experimental and computational constraints in the past, existing research has been limited to turbulence energy levels where bubbles deform primarily due to the buoyancy forces rather than turbulence-induced fluctuations i.e, $Eo \gg We$ (Poorte and Biesheuvel, 2002; Prakash et al., 2012; Lu and Tryggvason, 2013; Loisy and Naso, 2017). Therefore, the current experimental setup was carefully designed to generate strong turbulence, where the turbulence-induced deformations can dominate the buoyancy effects. Consequently, in chapters 4 and 5, the data collected from such experiments provided a robust framework to develop closure models for the drag, lift and added-mass coefficients.

## MISCIBLE TWO-PHASE FLOWS IN POROUS MEDIUM

In the opposite limit when $Re \ll 1$ and $Fr \ll 1$, i.e., the inertial forces are much smaller than the viscous and gravitational forces, equation 1.6 can be rewritten as

$$\nabla^* \cdot (\alpha_k(\overline{\overline{\mathbf{T}^*}}_k + \overline{\overline{\mathbf{T}^*}}^{Re}_k)) + \frac{Re}{Fr^2}\alpha_k\rho_k^*\hat{\mathbf{g}} = 0 \tag{1.10}$$

This is typically the case for low-$Re$ two-phase flows in a porous medium, where the inertial forces are negligible and one can usually ignore the momentum exchange term. In such a scenario, a balance between the buoyancy force that drives the flow and viscous force that resists the flow eventually determines the flow dynamics. On one hand, if the viscous force dominates, then any instabilities in the flow are damped and the flow remains stationary, until the conditions change. On the other hand, if the buoyancy force dominates, then any instabilities in the flow can grow strong enough to drive the flow (Riaz et al., 2006). Although one can ignore the momentum exchange term in this case, if the two fluids are miscible, then the interfacial mass transfer term, $\dot{\Gamma}_k^*$ in equation 1.5 becomes very important.

$$\frac{\partial}{\partial t^*}(\alpha_k\rho_k^*) + \nabla^* \cdot (\alpha_k\rho_k^*\mathbf{u}_k^*) = \dot{\Gamma}_k^* \tag{1.11}$$

One example of such a case is observed during the geological sequestration of anthropogenic $CO_2$ in underground saline aquifers (Riaz and Cinar, 2014). $CO_2$ is injected into these aquifers is lighter than the brine solution and typically accumulates at top of the aquifer. However, unlike the air-water fluid pair, these two fluids are miscible and therefore, $CO_2$ slowly diffuses into brine at their interface. Interestingly, the $CO_2$-brine mixture at the interface is heavier than the brine solution itself, resulting in an unstable configuration, where heavier fluid sits on the top of a lighter one. This type of instability has been studied as a Rayleigh-Bénard convection problem and the key dimensionless number, Rayleigh number $Ra = \frac{\Delta\rho g H K}{\rho \nu D_m}$ represents the ratio of the buoyancy force to the viscous damping forces. In $Ra$, $\Delta\rho/\rho$ characterizes the ratio between the maximum density difference $\Delta\rho$ between the two-fluids mixture and the bottom fluid with density $\rho$; $K$ represents the permeability of the porous medium; $H$ is the height of the reservoir; $D_m$ is the mass diffusivity and $\nu$ is the viscosity of the mixture. If $Ra$ is high enough, then the instabilities at the interface can grow and drive a convective mixing of the two fluids. Due to convection, the dissolution time of $CO_2$ into brine is significantly reduced when compared to diffusive mixing alone, which potentially reduces the risk of $CO_2$ leaking back to the surface over time.

Typically, these underground aquifers are riddled with heterogeneities characterized by multiple layers of alternating high and low porosities, which can

significantly affect the efficiency of such convective mixing (Farajzadeh et al., 2011; Agartan et al., 2015). Therefore, to create models that can predict the explicit dependence of this mass transfer rate on the parameters of heterogeneity, we conducted experiments in a 2D Hele-Shaw cell embedded with latex discs. By placing a single line of these discs horizontally in the cell, we could replicate the layered heterogeneous porous medium typically found in the aquifers and still give access to perform optical measurements like the shadowgraph imaging.

In order to guide the reader through this thesis, the following section §1 provides a brief summary of the topics covered in each chapter including the description of experimental apparatus and diagnostic systems (chapter 2), the details of data processing codes (chapter 3), and the modeling of closure parameters in the interface exchange terms (chapters 4 to 6).

---

## A BRIEF GUIDE THROUGH THIS THESIS

In chapter 2, we first review the existing turbulent two-phase experimental setups and their diagnostic systems. Consequently, we introduce our experimental setup (called vertical octagonal non-corrosive stirred energetic turbulence, V-ONSET) that was specifically designed and built to study the dynamics

of finite-sized deformable bubbles in intense ambient turbulence. The diagnostic system of V-ONSET uses particle shadow technique to extract simultaneous, three dimensional (3D) information of both the phases at high spatio-temporal resolutions. This is made possible via six synchronized high-speed cameras, each with a dedicated light emitting diode (LED) that simultaneously casts shadows of bubbles as well as nearby tracer particles in the continuous water phase around bubbles.

After capturing the images with six cameras, they need to be merged together in order to acquire the 3D information of the two phases. As the first step, the images captured by each camera were processed to separate bubbles and particles based on a median size filter. After separation, the 3D geometries of bubbles were reconstructed by merging the bubble images from all six cameras based on the virtual camera based visual hull (VCVH) technique developed by Masuk, Salibindla, and Ni (2019). On the other hand, the continuous phase is probed via an in-house open source Lagrangian particle tracking (OpenLPT) code (Tan et al., 2020a,b) based on the Shake-The-Box (STB) algorithm developed by Schanz, Gesemann, and Schröder (2016). The details of this code, including its structure and performance on synthetic and experimental data sets are discussed in chapter 3.

In an attempt to provide realistic closure models for the interfacial momentum transfer term in equation 1.8, we used this high-resolution 3D Lagrangian

information to investigate the hydrodynamic forces, specifically the drag, lift and added-mass coefficeints of finite-sized deformable bubbles in ambient turbulence. To this end, in chapter 4, we used the mean rise velocity of bubbles in conjunction with the mean vertical fluid velocity around them to determine the lift and drag coefficients of bubbles, along with their dependence on the turbulence Weber number (which controls the deformation of bubbles) and particle-based Reynolds number respectively.

In addition to the drag and lift coefficients, the added-mass coefficient is a third model parameter that is introduced in equation 1.8. Conventionally, it is very difficult to model this coefficient as it is a part of the unsteady force term that necessitates the measurements of second-order statistics like the Lagrangian accelerations of both the phases and turbulence velocity gradients. These statistics are very sensitive to noise and thus pushes the limits of 3D flow measurements in multi-phase flow systems to the extreme. Nevertheless, using our novel V-ONSET setup and its flow diagnostic system, we could reliably extract this information and model the dependence of the added-mass coefficient on the bubble shape and orientation, which is discussed in detail in chapter 5.

Chapters 2 to 5 of this thesis focus on the experimental setup, the flow diagnostic systems, and closure models of the momentum exchange term for immiscible air-water system in high-$Re$ turbulent flows. In contrast, chapter 6

focuses on the mixing efficiency of two miscible fluids in the opposite limit of low-$Re$ Rayleigh-Darcy regime in porous medium. In this chapter, we explicitly investigate the effects of heterogeneity present in the underground porous medium on the mixing efficiency of two fluids that mix via dissolution-driven convection. Such a mechanism is widely observed during carbon sequestration in underground saline aquifers. This experimental study uses a Hele-Shaw cell with inserted latex discs of different sizes in order to replicate the layered heterogeneity observed in such aquifers. Moreover, shadowgraph technique was used as a flow diagnostic system to identify the interface between the two miscible fluids with mismatched densities. As the two fluids mix together, the lighter fluid on the top slowly dissolves into the heavier fluid and their interface moves upwards during this process until it eventually disappears when both the fluids are completely mixed. This rise velocity of the interface was used to calculate the mass transfer rate. Finally, based on the collected experimental data, a model is proposed to predict the dependence of mixing rate on the properties of heterogeneity.

# Chapter 2

# A review of turbulent multi-phase experimental setups and their diagnostic systems

Dispersed multi-phase flows are widespread in both natural (Wyngaard, 2010; Deane and Stokes, 2002) and industrial settings (Launder, 1991; Michiyoshi and Serizawa, 1986; Jakobsen, 2008) and such flows are often very turbulent. Some examples include air bubbles entrained in breaking waves, particles ejected from volcanic eruptions, fluidized beds, or bubbly flows in nuclear reactors. If one wants to investigate them experimentally and provide robust data-based models, the experimental data sets in turbulent multi-phase flows that can probe the multi-scale interplays between different phases are very difficult to obtain. This is partly due to the inadequacy in adapting the classical

single-phase flow setups directly to turbulent multi-phase problems. Consequently, one needs to be more strategic in designing the experimental setups for turbulent multi-phase systems depending on the particular quantities that need to be examined.

With the aim of providing some insights into the workings of existing turbulent multi-phase flow setups, the following section introduces some common facilities that have been used in the past (section §2). Later on, section §2 gives a brief description of the current experimental setup called the vertical octagonal non-corrosive stirred energetic turbulence (V-ONSET) that was specifically designed to explore the unclosed terms of the interfacial momentum equation for finite-sized deformable bubbles in intense ambient turbulence. Moreover, section §2 gives a brief introduction of the commonly used diagnostic systems to quantify dispersed multi-phase flows over a wide range of void fractions. This is followed by a description of the optical measurement system that was employed in the V-ONSET to obtain time-resolved 3D Lagrangian measurements of the dispersed bubble and continuous water phases simultaneously.

# CHAPTER 2. MULTI-PHASE EXPERIMENTAL SETUPS AND THEIR DIAGNOSTIC SYSTEMS

## TURBULENT MULTI-PHASE EXPERIMENTAL SETUPS

The facilities that are classically used to investigate dispersed turbulent multi-phase flows can be broadly classified into flows with (i) shear-driven turbulence, where the turbulence exhibits a sharp gradient; and (ii) homogeneous isotropic turbulence, where the turbulent properties are uniform in space. A third type of system that will not be discussed here are the bubble columns, which typically have a high concentration of the dispersed phase that induces pseudo-turbulence as they move through the continuous medium. For a comprehensive review on such flows, the readers are advised to refer to a recent review by Besagni, Inzoli, and Ziegenhein (2018).

Shear turbulence is common in flows along a frictional boundary because the slow flow near the boundary is sheared by the faster flow; like high-speed winds over the ground or flow near the hull of a ship. To experimentally investigate such flows, among the shear-driven setups, Taylor-Couette (TC) system (Gils et al., 2011; Anantharaman, 2019) is the most commonly used one, where the working fluid is placed between two concentric hollow cylinders and either one or both the cylinders rotate about a common center to generate a shear-driven flow between them. At lower Reynolds numbers, the flow in the cylinder gap forms Taylor vortices but with increasing Reynolds number, the instabilities grow strong enough to generate turbulence. Particles or bubbles

were the most common dispersed phases that were studied in TC systems to probe dynamics like their phase distributions (Murai, Oiwa, and Takeda, 2005; Verschoof et al., 2016), translation and rotational dynamics (Anantharaman, 2019; Ravelet, Delfos, and Westerweel, 2010), turbulence modulation (Ravelet, Delfos, and Westerweel, 2010), and most importantly, the drag reduction (Mehel, Gabillet, and Djeridi, 2006; Gils et al., 2013; Bakhuis et al., 2018). In addition, effects of wall roughness (Verschoof et al., 2018), hydrophobic surfaces (Bullee et al., 2020) and use of rigid fibers (Bakhuis et al., 2019) in TC flows were some other unique studies that provided insights into the drag reduction mechanisms. However, in shear-driven flows, the mean spatial gradients in turbulent properties play an important role in determining small-scale interfacial effects which translates to macroscopic transport properties like the interfacial area concentration and drag reduction. This limits the applicability of such systems. Therefore, multi-phase systems with homogeneous isotropic turbulence have been extensively used to understand the fundamental mechanisms that drive the interfacial momentum transfer between different phases in turbulence with spatially uniform properties.

Homogeneous isotropic turbulence (HIT) has attracted a lot of attention in the multi-phase community, due to its universality, mathematical simplicity and statistical repeatability of experiments, which makes modeling much easier and more robust. Experimental studies like the mean rise velocity of bub-

bles (Poorte and Biesheuvel, 2002; Prakash et al., 2012; Wang and Maxey, 1993b; Aliseda and Lasheras, 2011) and the mean settling velocity of heavy particles (Wang and Maxey, 1993a; Aliseda et al., 2002; Yang and Shy, 2003), their acceleration statistics (La Porta et al., 2001; Voth et al., 2002; Calzavarini et al., 2009), or concentration distributions (Squires and Eaton, 1991; Wood, Hwang, and Eaton, 2005) have provided insights into the fundamental mechanisms that are at play.

A common technique that has been widely used to generate HIT in a laboratory environment is by running the working fluid through grids. When the flow passes through these grids, which can be either passive (Aliseda and Lasheras, 2011) or active (Poorte and Biesheuvel, 2002; Villermaux, Sixou, and Gagne, 1995; Mercado et al., 2012), they introduce grid-sized disturbances into the flow. These disturbances spread downstream and eventually mix together to create a homogeneous isotropic turbulence. The energy dissipation rates reported in literature for a grid-based setup with water as a working fluid are listed in table 2.1 with a highest reported value of $7 \times 10^{-3}$ $m^2/s^3$ (Ravelet, Delfos, and Westerweel, 2010). Table 2.1 also lists some other similar HIT setups, where the Lagrangian energy module (LEM) setup with 12 propellers placed symmetrically around a octahedron structure has the highest energy of $3.6 \times 10^{-2}$ $m^2/s^3$ (Zimmermann et al., 2010).

However, we realized that the energy dissipation rates in these HIT sys-

tems used for multi-phase studies are much lower when compared to real flow situations like the oceans (O(10) $m^2/s^3$ Deane and Stokes (2002)). The reason for this is because most prior studies have focused on understanding the multi-phase dynamics in high-$Re_\lambda$ turbulence ($Re_\lambda = u'\lambda/\nu$), which is very important for single phase flows but not in turbulent multi-phase flows, where the dispersed phase primarily responds to turbulence structures at their own length scales. Here, $\lambda$ is the Taylor micro-scale, $\nu$ is the kinematic viscosity, and $u'$ is the velocity scale that is typically associated with eddies of size $L$ (the integral length scale) (Frisch, 1995). Furthermore, in such weak turbulent cases, buoyancy forces often dominate the bubble deformations due to large density differences ($\Delta\rho = \rho_l - \rho_g$) between water and air. Keeping in mind that the objective of the current study is to experimentally investigate the unclosed terms of interfacial momentum transfer in equation 1.9 for bubbles deforming by turbulence fluctuations rather than buoyancy, one can perform a simple comparison between the buoyancy force, $F_g = \Delta\rho g D$ and turbulent induced forces in HIT, $F_t = \rho_l u'^2 = 2.13\rho_l(\epsilon D)^{2/3}$ (assuming inertial range scaling; Kolmogorov (1949)) on bubbles of diameter, $D = 2$ mm. This comparison shows that the required average turbulence energy dissipation rate, $\epsilon$ should be close to 0.57 $m^2/s^3$ for turbulence to dominate bubble deformations. Therefore, the current experimental setup, called the V-ONSET was designed to generate homogeneous isotropic turbulence with an $\epsilon$ of the order of $O(0.1)$ $m^2/s^3$, which is

atleast an order of magnitude higher than the previous setups.

| Turbulence generation | $\epsilon$ ($m^2/s^3$) | $Re_\lambda$ |
|---|---|---|
| Active grid - Twente water tunnel (Mercado et al., 2012) | $7.9 \times 10^{-4}$ | $160 - 265$ |
| Rotating grids (Ravelet, Delfos, and Westerweel, 2010) | $7 \times 10^{-3}$ | 300 |
| Oscillating grids (Villermaux, Sixou, and Gagne, 1995) | $1.3 \times 10^{-4}$ | $170 - 300$ |
| One sided synthetic jets (Variano and Cowen, 2008) | $10^{-3}$ | 314 |
| Two sided synthetic jets (Bellani and Variano, 2014) | $4.65 \times 10^{-5}$ | 334 |
| Propeller-based forcing (Icosahedron shape) (Zimmermann et al., 2010) | $3.6 \times 10^{-2}$ | 330 |
| High-speed jets (V-ONSET) (Masuk et al., 2019) | $1 \times 10^{-1} - 5 \times 10^{-1}$ | $110 - 300$ |

**Table 2.1:** Comparing the energy dissipation rate and turbulence Reynolds number of turbulent multi-phase experimental facilities with water as a working fluid.

---

## THE V-ONSET EXPERIMENTAL SETUP

As we are particularly interested in studying the dynamics of finite-sized air bubbles which are very buoyant and rise quickly through water, the V-ONSET

setup was designed to be a vertical water tunnel. Three key features of this setup that sets it apart from previously existing turbulent multi-phase setups include, (i) relatively high-energy homogeneous isotropic turbulence; (ii) a controllable mean flow; and (iii) its flow diagnostic system. In this section, we focus on the first two features of the V-ONSET. The flow diagnostic system will be discussed later in section §2.0.3 of this chapter after introducing some commonly used dianostic systems in section §2.

The current experimental setup has a modular design consisting of nine major components to construct a 2.73 m tall closed-loop vertical water tunnel as show in figure 2.1. Figure 2.1(a) shows a photo of the tunnel and figure 2.1(b) shows a schematic of the same, where each component is labeled individually for clarity. The purpose of these components can be broadly classified into either generating turbulence with desired characteristics or maintaining a controlled mean flow.

Seeking inspiration from the turbulent multi-phase setups in Variano and Cowen (2008) and Bellani and Variano (2014) that use synthetic jets to generate HIT with a negligible mean flow, in the V-ONSET setup, turbulence is generated by shooting high-speed synthetic jets into the test-section. However, unlike the previous setups that use submersible pumps to shoot jets, in the current setup, we used a system comprising of the pressure tank and the jet array that can shoot jets at much higher speeds. The jet array is a 3D printed

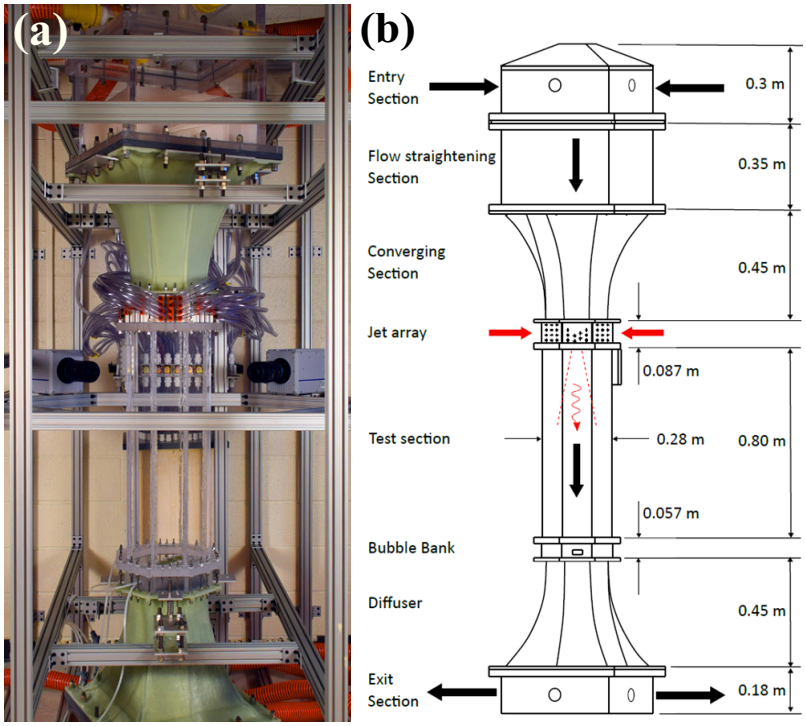


**Figure 2.1:** (a) A picture and (b) a schematic of the V-ONSET turbulent multi-phase experimental setup

object made of nylon glass beads and sits on top of the test-section as shown in figures 2.1(a & b). It consists of an array of 88 nozzles. Figure 2.2(a) shows an image of the jet array, where the square spaces allow the mean flow to pass through them and jets shoot from the 5 mm diameter circular holes. On the other hand, the pressure tank is made of 2 inch thick PVC pipe and has a cylindrical structure with two plates glued at the top and bottom. The top plate has 88 connectors as shown in figure 2.2(b), where each fitting is individually connected to the circular nozzles of the jet array via a solenoid valve (figure 2.2(c)). Opening and closing these solenoid valves controls the jet injection pattern, which effectively changes the turbulence characteristics in the tunnel (Pérez-Alvarado, Mydlarski, and Gaskin, 2016). The advantage of using this system over the submersible pumps for injecting the jets is that the power source, i.e the pressure tank is moved out of the tunnel. Therefore, unlike in Variano and Cowen (2008) and Bellani and Variano (2014), we can achieve high jet speeds just by increasing the water pressure in the pressure tank. Using a 2 horse power pump, we could achieve jet speeds as high as 12 m/s, an order of magnitude higher than previously reported 0.6 m/s. Furthermore, the injection length scale for turbulence, i.e. the distance between two adjacent nozzles in the jet array was also reduced to 2.1 cm in comparison to 7 cm in Variano and Cowen (2008). Given that the turbulence energy dissipation rate scales with fluctuation velocity, $u'$ and injection length-scale, $l$ as $\sim u'^3/l$, we could thus

increase $\epsilon$ to 0.5 $m^2/s^3$. The Kolmogorov length ($\eta$) and time scales ($\tau_\eta$) of the system are 38 $\mu$m and 1.4 ms, respectively. Integral length scale, $L$ is 3.2 cm and the fluctuation velocity $u' = 0.25$ m/s. Finally, $Re_\lambda$ is kept at around 346 in our system.

In addition to the turbulence generated by synthetic jets, the V-ONSET is also capable of having a controlled downward mean flow. The mean flow control system was specifically designed to counter the rise velocity of buoyant air bubbles in the tunnel and increase their residence time in the measurement volume so as to collect longer statistics from each experiment. Extra care has been taken to make sure that the mean flow is laminar and streamlined in the vertical direction so that the turbulence is only generated via synthetic jets injected into the tunnel. During experiments, mean flow enters the tunnel through the top and then flows through a honeycomb followed by a converging section. The honeycomb structure straightens the flow and the converging section accelerates it vertically, thereby removing any secondary flows in the lateral directions. This straightened mean flow then enters the octagonal test-section after passing through the square holes of the jet array (as shown in figure 2.2(a)), where it mixes with the turbulence generated by the synthetic jets. For symmetry, there is a diverging channel followed by an exit section at the bottom of the tunnel.

Air bubbles were injected into this system via capillary needles located at

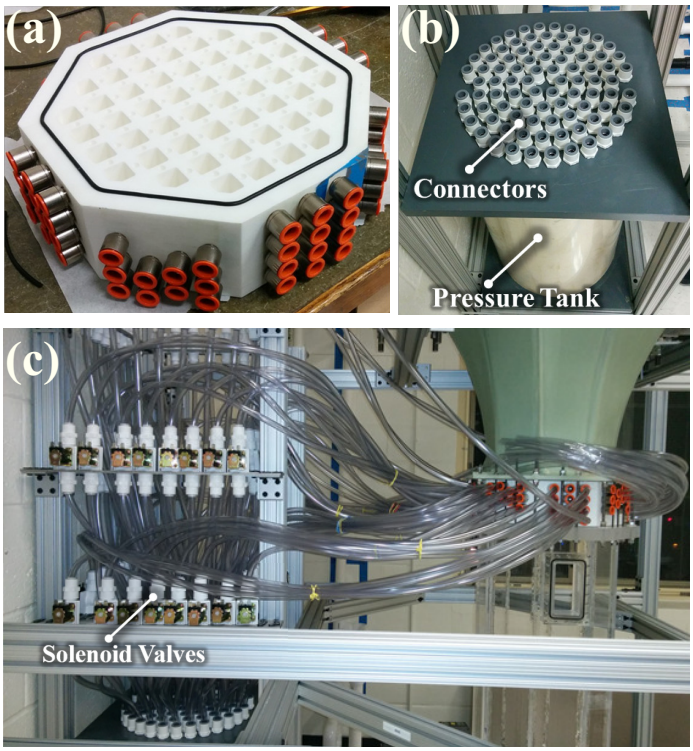


**Figure 2.2:** Photos of the turbulence generation system in V-ONSET including, (a) the 3D printed jet array; (b) the pressure tank; and (c) the connections between them via computer-controlled solenoid valves.

the bottom of the test section. Varying the needle size and airflow rates allows for the injection of bubbles of different sizes. These bubbles rose up into the center of the test section, although rather slowly due to the downward mean flow, where they interacted with the homogeneous isotropic turbulence generated by the jet array. Moreover, the carrier phase was seeded with 50-micron tracer particles that were used to quantify local flows around bubbles. More details of this setup and its flow characteristics can be found in Masuk et al. (2019).

The dynamics of bubbles and their interaction with surrounding turbulence was captured by a specially designed optical diagnostic system consisting of six high-speed cameras. But before discussing the details of the V-ONSET diagnostic system in §2.0.3, the following section summarizes some common systems that have been used to quantify the flow in multi-phase facilities.

---

## MULTI-PHASE FLOW DIAGNOSTIC SYSTEMS

The type of diagnostic system that one uses to study multi-phase flows depends on multitude of factors including but not limited to (i) the physical and optical parameters of the two phases; (ii) the void fraction of dispersed phase; (iii) the size and complexity of the system; (iv) how invasive is the measurement

system; (v) required spatio-temporal resolutions; (vi) two or three dimensional measurements; and (vii) desired quantities to be measured like the void fraction distribution, particle size and shapes, flow velocity, interfacial area, and flow topology to name a few. Unfortunately, no single system exists that can be used for all types of multi-phase flows, as each one of them have their own advantages and limitations.

### 2.0.1 Optical systems

For multi-phase facilities that have an optical access to the flow and relatively low void fractions (typically below 5% for gas-liquid and 1% for particle-laden flows) with a high transparency, the optical-based systems are an ideal choice for flow measurements. They use either the opacity of one of the phases (like solid particles in air) or refractive index mismatch between different phases (like air bubbles in water) to measure the flow characteristics. The most common optical based systems that have found success in multi-phase measurements include fiber optical probes (FOP) for single point measurements, or particle based systems like Laser doppler velocimetry (LDV), particle shadow velocimetry (PSV), and flourescent particle image velocimetry (FPIV) for two or three dimensional simultaneous flow measurements.

Fiber optical probe is a common intrusive tool for two-phase studies, which relies on the refractive index mismatch between the phases (Miller and Mitchie,

1970). A typical optical probe consists of two optical fibres inserted into the flow where one acts as a light source and the second one acts as a receiver. Due to the refractive index mismatch, the amount of light entering the receiver depends on the phase surrounding the probe tip, which is then calibrated to identify each phase. The advantage of this sensor over other typical intrusive methods like conductivity probes is that the size of optical probes are much smaller, making them less invasive. Furthermore, using fibre-optical sensors, the size, chord length and shape of the dispersed phase can also measured by systematically placing multiple probes in the flow (Li et al., 2012). However, they can only provide single point measurements and will modify the flow itself. Hagemeier et al. (2015) compared the velocity measurements from optical probes with other non-intrusive optical methods like the particle-based systems in fluidized beds and reported that FOP had the highest temporal resolution and is the most economical choice for continuous flow monitoring but the estimated particle velocities were always lower than the actual values due to their invasive nature. Furthermore, another comparison study by Prakash et al. (2019) in gas-solid-liquid three phase systems estimated that on an average, the FOP velocity measurements were 20% lower than non-intrusive systems.

Non-intrusive optical methods such as particle image velocimetry (PIV) or particle tracking velocimetry (PTV) have seen a lot of success in visualizing single-phase flows (Schanz, Gesemann, and Schröder, 2016; Westerweel, Elsinga,

and Adrian, 2013). Both these optical methods rely on seeding tracer particles into the flow. By using either laser-induced scattering or light emitting diodes (LED) for back-lighting, the tracer particles are captured on cameras for further processing. However, in two-phase flows, the presence of the second phase can hinder the optical access to the tracer particles due to the opacity or refractive index mismatch between the two phases. This is especially problematic at a high concentration of the dispersed phase. Nevertheless, such optical diagnostic systems have been successfully implemented for two phase flows with a few modifications. These modifications can be broadly classified into flourescent particle image velocimetry (FPIV) and particle shadow velocimetry (PSV).

The FPIV technique uses fluorescent particles in combination with a laser beam to visualize the flow. Flourescent particles, unlike the dispersed phase particles, emit light at a wavelength that is different from that of the incident laser light. Therefore, by using appropriate light pass filters, one can separate the two phases. However, the reflections caused by the interface still limits the use of this method to low void fractions. This is clearly seen in figure 2.3(a) that is taken from Zhou, Doup, and Sun (2013), where bubbles in the flow reflect the light and appear as dull white blobs. Zhou, Doup, and Sun (ibid.) used the 2D FPIV method for bubbly flows to quantify the carrier phase and developed an image processing technique that can remove the noise caused by the dispersed bubbles for up to void fractions of 18%. In addition to bubbly

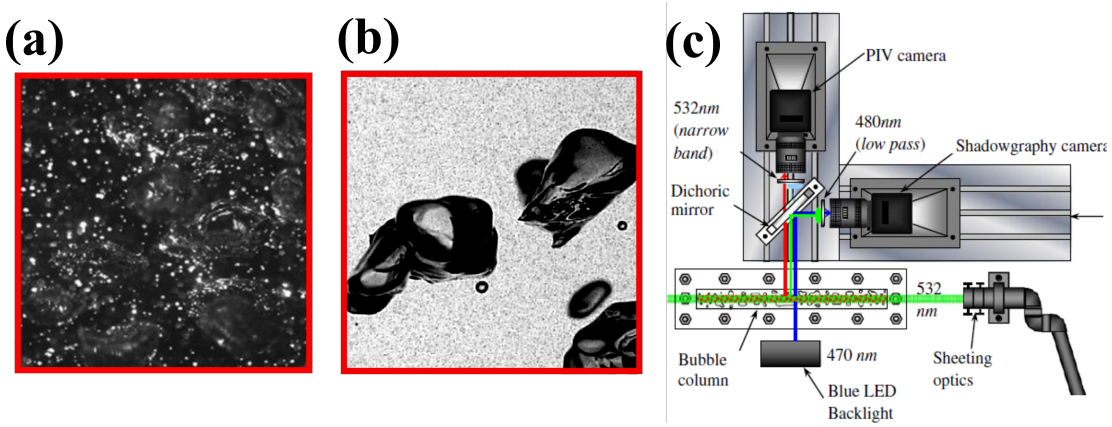


**Figure 2.3:** Images taken from (a) Zhou, Doup, and Sun (2013) captured using the FPIV technique for a bubbly flow with 18% void fraction and (b) Hessenkemper and Ziegenhein (2018) captured using the PSV method in a thin rectangular bubble column with 10% void fraction; (c) A schematic of the experimental setup from Sathe et al. (2010) that uses two cameras along with a dichoric mirror to simultaneously capture FPIV and PSV images of a bubbly column flow.

flows, the FPIV method has been fruitfully applied to a wide range of multi-phase flows including thin liquid-film flows (Charogiannis, An, and Markides, 2015), jet flows (Hu et al., 2000), stratified oil-water pipe flows (Ibarra et al., 2018), and even turbulent scalar mixing (Law and Wang, 2000).

Unlike FPIV, the PSV method uses a light emitting diode (LED) for back-lighting, which casts a shadow of the tracer and dispersed particles onto the cameras image. Using an LED instead of a laser significantly reduces the setup cost. A major advantage of using PSV over FPIV is that in addition to the particle shadows, it also casts a shadow of the outline of dispersed phase, which can be used to determine their shapes (example figure 2.3(b) taken from Hes-

senkemper and Ziegenhein (2018)). This is especially useful for studying the interfacial dynamics in bubbly flows. For example, Bröder and Sommerfeld (2007) performed simultaneous measurements in bubble columns to get the 2D bubble shapes along with the velocity field around bubbles. Ziegenhein et al. (2020) performed experiments in a circular bubble column and successfully used the PSV method for simultaneous 2D measurements at void fractions of up to 7.55 %. Furthermore, by restricting the flow to a thin rectangular bubble column, Hessenkemper and Ziegenhein (2018) reported that they could go up to gas fractions of 10% with minimum loss of information.

However, a major disadvantage of PSV that limits its usage is the low signal to noise ratio when compared to FPIV. This is attributed to the low-intensity blurry shadows cast by particles outside the depth of field of the cameras but still in the path of incident back lighting (Tan et al., 2020b). Therefore, it is a common practice to use PSV in combination with FPIV, where the laser and LED produce light at different wavelengths in order to separate them using optical filters. For example, Lindken and Merzkirch (2002) used a single camera in conjunction with an optical filter to combine the FPIV and shadowgraph images of gas bubbles and separated the two phases using a size and intensity image-processing filter. As shown in figure 2.3(c), Sathe et al. (2010) took it a step further with the help of two cameras and a dichoric mirror to measure the shape, size, velocity and acceleration of a swarm of spherical cap bubbles

rising in a quiescent medium along with the liquid velocities right up to the bubble interface. However, one needs to keep in mind that it is not straightforward to avoid a cross-talk between the two phases and the biggest challenge is the image processing in order to isolate the two phases with minimal interference between them. A comprehensive description of disadvantages in using an optical system for multi-phase flows has been discussed in Poelma (2020), including the cross-talk between the two phases, signal to noise ratios and biased statistics. Data losses of up to 20% have been reported due to the presence of second phase even at void fractions as low as 0.5% (Poelma, Westerweel, and Ooms, 2006). Ziegenhein and Lucas (2016) talks about the sampling bias for 2D PSV in a bubble column as the bubble shadows block the flow measurements and creates a bias in getting the velocity information of the continuous flow using PIV. In order to tackle this problem, they introduced a hold processor which holds the camera image until all the PIV windows are filled with atleast one information from the tracers and then they average the information over the hold time. Although they showed that this reduces the statistical bias in the measurements, we speculate that it comes at a cost of reduced temporal resolution.

To overcome these limitations, one commonly used method is refractive index matching, where either one or both the phases are modified in order to match their refractive index. The advantage is that the dispersed phase, al-

though present in the flow, does not refract any light passing through them. Using this method, two-phase flows have been optically resolved successfully for up to 50% void fraction in oil-water/glycerol flows (Voulgaropoulos and Angeli, 2017). However, it is not always possible to find fluids that can be refractive index matched, especially when one of the phases is a gas, due to a significant difference in their refractive indices. Therefore, all these systems that have been reported in literature so far are either liquid-liquid or solid-liquid flows. Furthermore, finding suitable combination also restricts the parameter space like the density or viscosity ratios of the two phases.

Flows like turbulence are however three dimensional in nature and therefore, it is essential to extend the flow measurements to the third dimension in order to unveil their complex behaviors. This is usually achieved by combining images from two or more cameras that capture the flow from different directions and then putting them together to provide a 3D map of the flow properties. In addition, there are some single projection 3D measurement systems like holography (Katz and Sheng, 2010) that uses the diffraction property of light and light-field (or plenoptic) imaging (Truscott et al., 2017) that uses a specialized camera with an array of lens that can capture the angle of incident light rays in addition to their intensity.

### 2.0.2 Electrical systems

A common technique that has been used extensively, especially for flows with very high void fractions (up to 86% (Angeli and Hewitt, 2000)) involves placing electrical probes like the conductive (Angeli and Hewitt, 2000; Nasr-El-Din, Shook, and Colwell, 1987; Costigan and Whalley, 1997; Paglianti and Pintus, 2001) or capacitive probes (Abouelwafa and Kendall, 1980; Strizzolo and Converti, 1993; Jaworek, Krupa, and Trela, 2004; Strazza et al., 2011) into the flow. They have been very effective in measuring parameters such as the local void fraction (Le Corre et al., 2003), interfacial area concentration (Kataoka, Ishii, and Serizawa, 1986; Revankar and Ishii, 1992; Wu and Ishii, 1999) and sometimes even the velocity of both phases (Jin et al., 2008; Manera et al., 2009) using multi-probe systems. The working principle of these probes includes the measurement of electrical properties (either the conductivity or capacitance) of each phase and calibrating the sensors to detect which phase is in contact with the probes. Such probes have been used in two-phase systems like oil-water (Angeli and Hewitt, 2000; Tan et al., 2015) or air-water (Revankar and Ishii, 1992; Kim et al., 2000) mixtures, where the electrical properties of both the phases are significantly different from each other. A major advantage of using this method is their high temporal resolution and signal to noise ratios. However, they can only perform single-point measurements and are an invasive technique which can modify the flow itself.

An extension of the electrical probes for flow measurement are wire-mesh sensors, which improves upon the spatial resolution of the electrical systems. As the names suggests, this involves placing a grid of these electrodes in the cross-section of the flow as show in figure 2.4(a). They have the same working principle as the probes, where they detect the electrical properties of each phase in contact with the mesh. The advantage of using a mesh instead of a probe is that they can also measure the void fraction distribution profiles across the flow (Da Silva et al., 2010, 2011; Barnea, Roitberg, and Shemer, 2013; Abdulkadir et al., 2014). Moreover, by placing more than two such grids along the flow direction, the measurements can be extended to the third dimension (Ito et al., 2011; Peña and Rodriguez, 2015). In addition to the void fraction, based on the temporal information, wire-mesh sensors have the capability to measure the size or shape of the dispersed phase (Peña and Rodriguez, 2015) along with their velocities (Schubert et al., 2010; Hoppe, Grahn, and Schütz, 2010; Tompkins, Prasser, and Corradini, 2018). They are sometimes combined with thermo-couple sensors to provide the temperature distribution profiles (Dudlik et al., 2008; Silva, Schleicher, and Hampel, 2009). However, as these sensors are significantly larger than the probes, they are much more intrusive and can alter the flow significantly. Nevertheless, they have been widely used in two-phase flow measurements.

In an effort to use the electrical properties of the two phases and mea-

sure the flow properties non-intrusively, especially for pipe flows, the probes and wire sensors were replaced with electrodes that are wrapped around the outer surface of the pipe (figure 2.4(b)). These electrodes are used to perform tomographic measurements and provide a cross-sectional image of the two phases along a 2D slice. They have been effective in obtaining the distribution of the two phases along a 2D cross-sectional slice of the pipe. In addition to the 2D phase distributions, electrical tomography systems have also been successfully implemented in measuring the individual phase velocities using two sets of electrodes placed along the flow direction. This is done by performing a cross-correlation of the two images (Warsito, Marashdeh, and Fan, 2007; Saoud, Mosorov, and Grudzien, 2017). Nevertheless, the spatial resolution is limited by the electrode size. Also, the electrode packings in such systems have many technological problems including geometric difficulties with their arrangements and field-cancellation by metallic parts and inserts, making them a less preferable choice for two-phase flow measurements.

### 2.0.3 Radiation based systems

For many multi-phase systems, especially at higher void fractions, the presence of dispersed phase adds turbidity to the flow, which makes it difficult to perform optical measurements. One solution to this problem is using systems like the electrical probes that was discussed earlier in section 2.0.2. How-

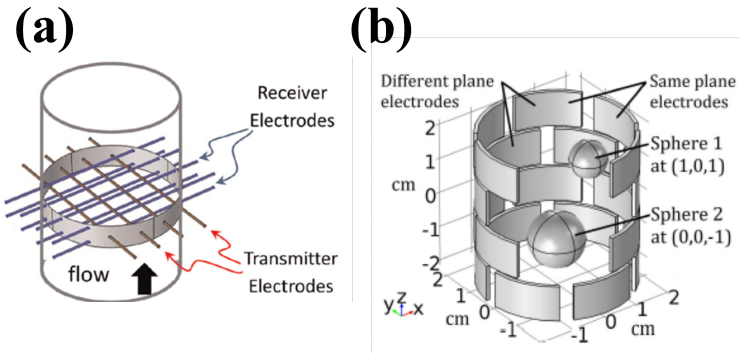


**Figure 2.4:** A schematic comparing the arrangement of electrodes in (a) the intrusive wire-mesh sensor (reproduced from Peña and Rodriguez (2015)) and (b) the non-intrusive electrical capacitance tomography system (reproduced from Chowdhury, Marashdeh, and Teixeira (2016));

ever, the measurements from such systems are usually intrusive and limited to either local void fractions, phase distributions, or sometimes local phase velocities. Therefore, this section briefly talks about the radiation based non-intrusive methods that have been developed to measure flow parameters like the velocity maps, similar to what the PSV and FPIV techniques could do for optically accessible flows. They include techniques like the X-ray imaging and magnetic resonance imaging (MRI), both of which are adapted from medical diagnostic systems.

An advantage of using X-rays over visible light is that, unlike the visible light, X-rays penetrate through objects in straight lines (i.e. the refractive index is close to one for most materials) and their absorption depends on the path-length integrated density of the materials that they pass through. Based

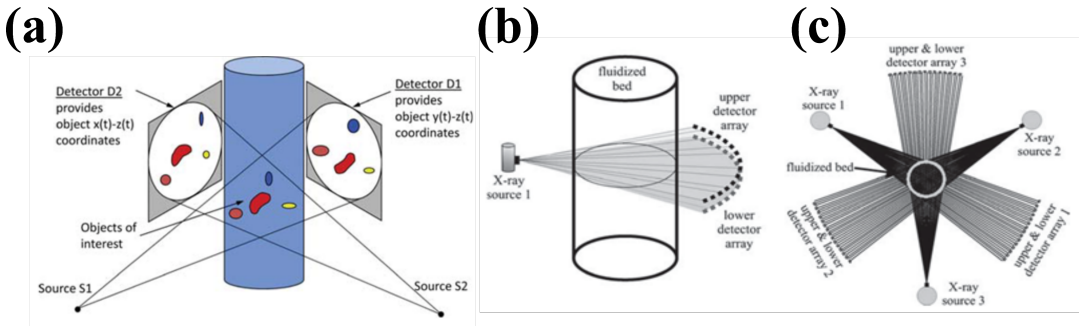


**Figure 2.5:** A schematic of (a) the X-ray stereography system; (b) the front view, and (c) the top view of ultrafast X-ray computed tomography system, all taken from Heindel (2011)

on these two properties of X-rays, methods like X-ray radiography and X-ray computed tomography have been developed to quantify multi-phase flows. X-ray radiography is similar to the shadowgraph imaging technique, where a beam of X-rays are incident on the flow, which absorbs different amount of X-rays depending on the phase distribution. A receiver or detector sits on the other side that captures the energy of remaining X-rays that pass through the flow. Using this information, a 2D attenuation map of the phase distribution can be reconstructed. This can be extended to 3D mapping by using more than one source-detector pair and is usually referred to as the X-ray stereography. A schematic of X-ray stereography reproduced from Heindel (2011) with two cameras is shown in figure 2.5(a). X-ray computed tomography takes it further and uses several hundred projections from different orientations to reconstruct an image of the flow cross-section along a 2D slice. By moving the source-detector

system in the third dimension, one can produce a volumetric reconstruction of the phase distribution. However, this only provides a time averaged flow information for dynamical systems. Ultrafast X-ray computed tomography has been developed to tackle this problem by rearranging the detectors in multiplane arrays (Mudde, 2011) as shown in figures 2.5(b) and 2.5(c), so that they can obtain multi-slice images simultaneously. This significantly improved the temporal resolution from the order of several minutes to a less than a millisecond (Lau, Hampel, and Schubert, 2018; Lau et al., 2018). However, this comes at a cost of reduced spatial resolution as increasing the number of detectors causes the X-rays to merge between multiple detectors. Furthermore, the quality of 3D data also depends on the reconstruction algorithms. A much more comprehensive review of laboratory scale X-ray systems for visualizing multi-phase flows is provided by Heindel (2011). Also, Hampel (2015) specifically reviewed the X-ray tomography systems.

There is a second class of X-ray imaging called synchrotron X-ray systems, which are large facilities with energy flux typically four to five orders of magnitude higher than the laboratory-scale systems. Furthermore, they mostly produce monochromatic X-ray beams that are rather useful for quantitative diagnostics. Kastengren and Powell (2014) reviewed the performance of synchrotron systems with applications in flows with high turbidity or significant refractive index gradients.

Magnetic resonance velocimety (MRV) is another radiation-based system that uses the spin properties of atomic nuclei in order get the spatially-resolved information about a structure including multi-phase flows. The working principle of MRV requires a knowledge of quantum mechanics and will not be described here. But it is worth mentioning that MRV can measure 3D flow properties at sub-millimeter resolutions for flows in porous media with no optical access and complex multi-phase flows at void fractions much beyond the capabilities of optical systems. However, its expensiveness and complexity, the small permissible object size and the inability to measure in metallic setups currently prevent a wider utilization for studies in fluid flow measurements. Readers are suggested to read the review papers by Elkins and Alley (2007) and Bonn et al. (2008) for more insights into the performance and applications of MRV systems. Overall, Poelma (2020) presented a very good summary of the recent developments in measurement systems for opaque flows including the magnetic resonance imaging, X-ray imaging, electrical tomography and ultrasound imaging systems and compares their performance (see table 1 of Poelma (ibid.)).

# CHAPTER 2. MULTI-PHASE EXPERIMENTAL SETUPS AND THEIR DIAGNOSTIC SYSTEMS

## V-ONSET FLOW DIAGNOSTIC SYSTEM

In the V-ONSET setup, the air injection rate was maintained such that the average void fraction of bubbles in the measurement volume was about 2% at any given time in order to minimize the bubble-bubble interactions but still have enough bubbles in the measurement volume to acquire reliable statistics from each experiment. According to the discussions in section 2, at such low void fractions, particle-based optical system was found to be the best choice to obtain simultaneous three-dimensional measurements of bubbles and flow structures around bubbles.

The V-ONSET optical measurement system has six high-speed cameras, placed strategically around an octagonal test-section as shown in figure 2.6(a). The octagonal shape provides eight flat faces so that the cameras can cover the entire perimeter from different directions without the need for any liquid filled prisms that limit the view volume. The cameras were placed such that the intersection volume has dimensions of $6 \times 6 \times 6$ cm$^3$ at the center of the test section. Each camera can record images at 4000 fps with a resolution of 1 megapixel. Furthermore, all the cameras were synchronized using a trigger switch to obtain simultaneous measurements from six different directions. In order to capture the flow structures around bubbles, the continuous phase is embedded with 50 micron poly-amide tracer particles that are density matched

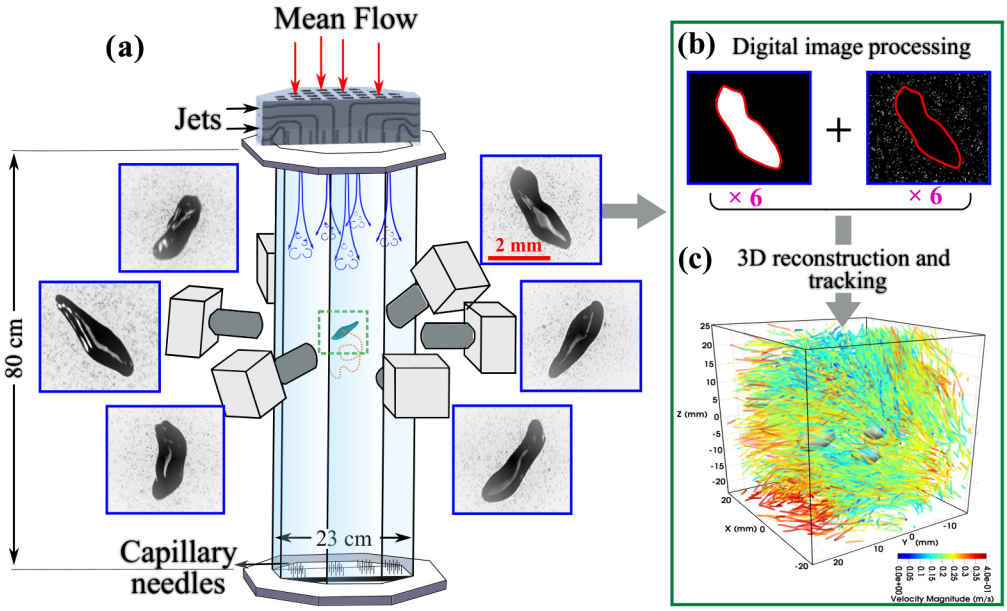


**Figure 2.6:** (a) A schematic showing the working of V-ONSET setup with turbulence generated by high speed jets shooting from the top and bubbles injected from the bottom of the octagonal test-section. It also shows the arrangement of six cameras and an example image captured by them at one time instant. Each image has a bubble and tracer particles around the bubble. (b) The captured images are then post-processed digitally to separate the projection of bubbles (left) and tracer particles (right). (c) The in-house 3D reconstruction codes described in Masuk, Salibindla, and Ni (2019) and Tan et al. (2020b) are then applied to each of these set of images to obtain the instantaneous 3D information of both the phases. Bubbles are shown as grey blobs along with its surrounding tracers that are color coded with their velocity magnitude.

with water. Each camera has a dedicated LED on the opposite side across test section that simultaneously casts a shadows of bubbles and tracer particles onto the camera image. Figure 2.6(a) shows an image captured by each camera from one of our experiments along with a schematic of the octagonal test section.

The images captured by these high-speed cameras were first processed to separate bubbles from particles based on their size and contrast. Figure 2.6(b) shows the inverted images from one of the cameras after separating the two phases. The cameras were calibrated before conducting the experiments in order to obtain their relative position for 3D reconstruction of the flow. The six time-locked images with the bubble 2D projections are then put together using a virtual camera visual hull (VCVH) reconstruction method recently developed in our lab by Masuk, Salibindla, and Ni (2019) in order to obtain their instantaneous 3D geometries. This method improves the conventional visual hull method based on the physical constraints imposed by surface tension between air and water, which tends to smooth any high-curvature regions present at the interface. The details of VCVH method are not discussed in this thesis and the readers are redirected to Masuk, Salibindla, and Ni (ibid.). On the other hand, the tracer particles, which appear to have a diameter of about three to five pixels on the camera images were tracked in 3D using our in-house OpenLPT (Tan et al., 2020a,b) based on the STB algorithm developed by Schanz, Gese-

mann, and Schröder (2016). More details about the experimental procedure including the camera calibration, the structure of the open source code and its performance on the synthetic and experimental data are presented in chapter 3. In each frame, over 7,000 tracer particles were tracked simultaneously. A snapshot of our 3D reconstructed results, including the 3D bubble geometry and the 3D tracks of surrounding tracers, is shown in figure 2.6(c).

# Chapter 3

# An open-source Shake-the-Box method and its performance evaluation

In experimental fluid dynamics, particle-based velocity measurements rely on imaging the motion of many small tracer particles that faithfully follow the flow. These images can be analyzed either by using the particle image correlation, i.e. particle image velocimetry (PIV, (Adrian, 1984)), or tracking individual particles, i.e. particle tracking velocimetry (PTV, (Papantoniou and Dracos, 1989; Nishino et al., 1989)). The particle image density is one of the most important parameters of both the systems because it determines the spatial resolution and also the quality of the results. The particle image density is typically determined by a quantity called particle per pixel (ppp). For example, 100 particles on an image made of $1000 \times 1000$ pixels results in a particle image density of $10^{-4}$ ppp. Particle tracking method started from the early work of

Chiu and Rib (1956), where they determined the 3D particle positions with the help of only two cameras. To avoid any ambiguity, the image density had to be kept really low at $10^{-5}$ ppp (Sheu et al., 1982; Chang, Wilcox, and Tatterson, 1984; Adamczyk and Rimai, 1988).

Maas, Gruen, and Papantoniou (1993) addressed this problem by using three or four cameras, and thereby improved particle image density to $10^{-4}$ ppp. Additionally, Malik, Dracos, and Papantoniou (1993) proposed to connect the particles frame by frame into tracks by minimizing the change in acceleration between consecutive frames. This algorithm was further improved by Ouellette, Xu, and Bodenschatz (2006) using a method called the four-frame best estimate (4BE) that could successfully track particles up to $10^{-3}$ ppp. The 4BE tracking method has been implemented in many systems, including convection (Ni, Huang, and Xia, 2011), porous medium flow (Shen and Ni, 2017), and animal collective motion (Ni et al., 2015b).

In order to resolve the velocity gradients of a flow that requires a very high spatial resolution, both Hoyer et al. (2005) and Ni et al. (2015a) developed the scanning particle tracking method. In both these systems, the particle image density was improved to more than 0.005 ppp at the cost of reduced temporal resolution, as instead of illuminating the entire view volume at once, it was scanned over several frames using a laser slab. Since similar number of particles can be tracked in each slab, the total particle image density is effectively

higher. But it requires a camera with a much higher frame rate to account for the loss in temporal resolution.

In comparison to PTV, the particle image density is much higher in 3D Tomographic PIV (Tomo-PIV), which can reach as high as 0.1 ppp (Kähler et al., 2016). This is because 3D Tomo-PIV only reconstructs the particle intensity field rather than isolated particles and the reconstruction allows ghost particles, even though it reduces the quality of the 3D measurements. One such reconstruction technique that has been effectively implemented is called the multiplicative algebraic reconstruction technique (MART) (Elsinga et al., 2006). Wieneke (2012) built up on the MART to switch the reconstruction from an intensity field to a particle field by using the iterative particle reconstruction (IPR). There are two innovative steps in IPR that helps reconstruct a dense particle field; (i) shaking: iteratively refines the particle 3D positions by continuously checking their reprojection with the original particle images on the camera, and (ii) intensity check: uses particle intensity information on the images to remove ghost particles.

However, IPR deals with each frame individually without any time coherence, that restricts the image density to 0.05 ppp, even in an ideal scenario with no noise in the particle images. Conversely, shake-the-Box (STB) method developed by Schanz, Gesemann, and Schröder (2016) extends the principle of IPR to the time domain and also enforces a temporal coherence of trajecto-

ries in particle reconstruction. These implementations were revolutionary, and STB is currently the state-of-the-art algorithm for time-resolved 3D velocity measurements at up to 0.125 ppp. Since its introduction, this method has been successfully implemented to measure different types of flow statistics such as velocity (Schneiders and Scarano, 2016), vorticity and dissipation (Schneiders, Scarano, and Elsinga, 2017), pressure field (Van Gent et al., 2017), as well as the coherent structure (Schlueter-Kuck and Dabiri, 2017). It was also adapted and improved by Novara et al. (2015) to a multi-pulse system, which can be used for high-speed flows. Novara et al. (2016b) modified STB to solve the issue of ghost particles at its initial phase by using two independent imaging systems.

In addition to an increase in particle density, another important benefit of the STB technique is its significantly-reduced processing time when compared to Tomo-PIV. It was reported in Schanz, Gesemann, and Schröder (2016) that the total processing time of STB for 500 images with around 12,800 particles is around 2 hours, which has greatly reduced from the processing time of 650 hours for MART. Despite this significant improvement, time-resolved measurements usually generate large datasets and the total processing time of multiple datasets that can be easily generated within seconds of experimentation is still overwhelmingly long if processed on a single desktop machine. Therefore, running such data analysis on a high-performance computing (HPC) system or a

Graphics Processing Unit (GPU) based system becomes an important step.

In order to provide an easy and open access to the STB algorithm and allow processing large amount of data, an open-source STB code has been developed and available on the GitHub repository Tan (2020 (accessed June 10, 2020)) for public use. The general principle of the open-source STB including some improvements over the conventional STB are presented in section §3. In section §3.0.2, the performance of the code and its comparison with the results reported in Schanz, Gesemann, and Schröder (2016) are carefully examined via synthetic data generated from the Johns Hopkins turbulence database. Furthermore, the current code was also tested on our experimental data. The details of the experimental procedure for data collection will be given in section §3.0.5 and section §3.0.5 will briefly discuss the performance of open-source STB on experimental data.

---

## THE OPEN-SOURCE STB

The goal of this chapter is to introduce an open-source STB code that is designed as a platform to improve the method and compare different algorithms. In addition, users can easily access the intermediate steps to conduct the uncertainty analysis. The code was written in C++, an object-based language that is

robust and versatile on different platforms. The code was originally written in the Windows system and later transferred to the Linux system. This code has been optimized to run on high-performance computing (HPC) clusters because of the growing need to analyze large datasets. Once STB is implemented on HPC, the image pre-processing and data post-processing have also been shifted to the HPC so that the entire processing time can be reduced by more than one order of magnitude. The structure of the open-source STB code is summarized in appendix A. Different choices and improvements that we have made during the development of open-source STB will be discussed in this section.

### 3.0.1 Wiener filter

Since STB relies on extrapolating an existing track to obtain the particle location in the next frame, the algorithm of extrapolation becomes important. Schanz, Gesemann, and Schröder (2016) used the Wiener filter method for this purpose and we would like to compare the performance of this filter with a simple polynomial filter to see how it affects the trajectory length and quality.

Wiener filter (Proakis and Manolakis, 2007) is a linear invariant filter in the form of

$$x(n+1) = \sum_{i=0}^{N-1} a_i s(n-i) \tag{3.1}$$

where $s(n)$ is the observed noisy process containing the signal, $x(n)$ is the out-

put at time $n$, and $N$ is the order. The parameters of Wiener filter are calculated by minimizing the mean square error (MSE) as follows:

$$a_i = \arg\min E(e^2(n)) \tag{3.2}$$

where $e(n) = x(n) - s(n)$. The known vector $S_{n-1} = [s_{n-N}, s_{n-N+1}, ..., s_{n-1}]$ is used to obtain the parameters $A_N = [a_1, a_2, ..., a_N]$ of Wiener filter by recursively updating the parameters through:

$$A_N = A_N + \mu S_{n-1}^T \cdot (s_n - A_N \cdot S_{n-1}) \tag{3.3}$$

where $\mu$ is the step length which is usually taken as $1/(S_{n-1}^T \cdot S_{n-1})$, until the estimated error $e(n) = s_n - A_N \cdot S_{n-1}$ reaches a specific precision. The next point is then predicted through equation 3.1 by using the parameters $A_N$. In the open-source STB, based on several trials, $5^{th}$-order Wiener filter is adopted to obtain the optimal prediction.

Polynomials filter uses the polynomials

$$x(n) = \sum_{i=0}^{N} b_i n^i \tag{3.4}$$

to fit data points by minimizing the MSE in the same form as in equation 3.2.

For an extremely low image density (<0.005 ppp), STB based on both the

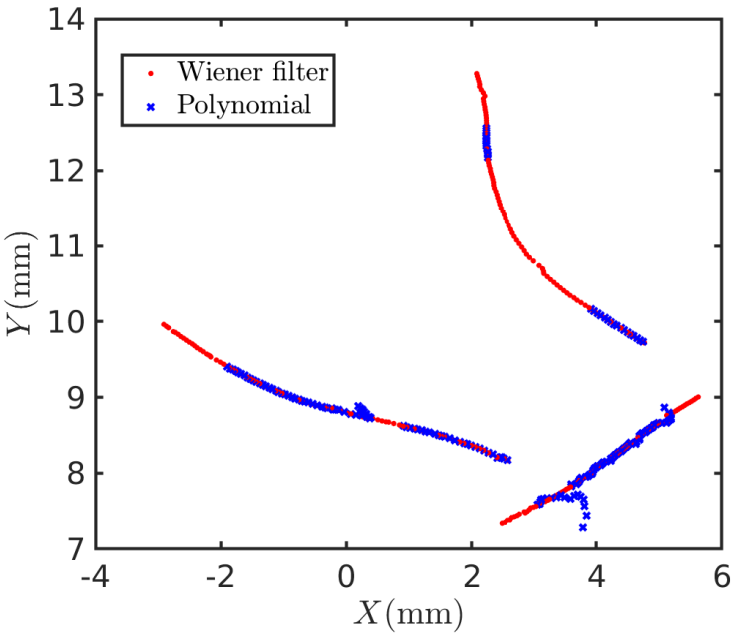


**Figure 3.1:** Sample trajectories identified by either the Wiener filter (red) or polynomials (blue) from a dataset at the particle image density of 0.0125 ppp.

Wiener filter and polynomials produces similar results with no discernible difference in either the number or the quality of trajectories. However, at higher particles densities, as shown in figure 3.1 for 0.0125 ppp, two problems for polynomials start to develop: (i) the trajectories become shorter and more broken, and (ii) two or more short particle tracks get incorrectly connected. We tried polynomials with different degrees from 3 to 10, and these two problems persisted. In comparison, the Wiener filter is more robust and produce good quality particle tracks even at a higher image density case.

The key difference between the two filters resides in their sensitivity to noise. At a high particle image density, overlapping particles lead to enhanced

position noise and ambiguity. Extrapolating from a noisy trajectory could result in a large prediction error if the noise has not been handled properly. Since the Wiener filter has proven performance in dealing with a random process, it shows a much better result in our test, which is consistent with the findings by Schanz, Gesemann, and Schröder (2016).

### 3.0.2 Linear-fit check

When either the particle image density or the image noise is high, the probability of finding a wrong track or a ghost track starts to increase. A wrong track is essentially several segments of good tracks incorrectly connected into one, and a ghost track is the track made of ghost particles. Typically ghost particles cannot be connected for many frames as they are not real, but they may still occur sometimes if the image noise is large enough. Linear-fit check is the simplest frame-by-frame examination of the trajectory quality, which is based on the assumption that the temporal resolution is so high that every four consecutive frames can be connected by a linear track with very small physical acceleration. If the measured acceleration turns out to be abnormally large, the linear-fit check will identify that. In practice, at frame number $n$, particles from four frames ($n-3$ to $n$) will be fitted with a linear function, and the difference between the last point of the track $X(n)$ and the linear-fitted result $\tilde{X}(n)$ is used as an indicator $e_f = X(n) - \tilde{X}(n)$. If $e_f$ is larger than a threshold, the

trajectory will be terminated and no longer be used for prediction, and a new track will start.

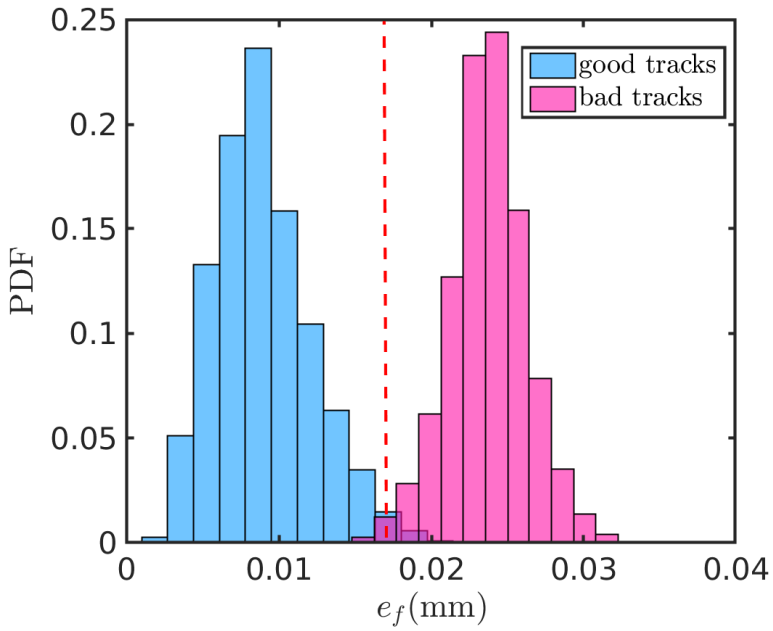


**Figure 3.2:** PDF of the linear-fit error $e_f$ for good and bad tracks

Figure 3.2 shows the PDF of good and bad tracks using an experimental dataset. For this dataset, no linear-fit check was used and the trajectory quality was evaluated after STB. The good tracks are smooth, and the bad ones are jagged because of the triangulation and shaking uncertainties. Once the tracks are categorized based on their smoothness, the PDF of $e_f$ of two groups are shown. It is clear that the bad tracks, either wrong or ghost tracks, tend to have a larger linear-fit error $e_f$, compared with the good ones. $e_f$ =0.018 mm (dashed line) seems to cleanly divide the tracks into two groups. This number is close to the calibration error, which is 0.014 mm.

In Schanz, Gesemann, and Schröder (2016), the linear-fit check only examines the last data point and decides the fate of this track based on if $e_f$ is above or below the threshold. This works well for removing most of the wrong tracks, but we found a new type of wrong track that cannot be effectively identified using this method. Those wrong tracks oscillate slightly within the threshold. Although this may be specific to experiments with large image noise in our back-lit particle tracking system, it may occur in other experimental configurations as well. To address this issue, for each track, the mean of the fitting error of all frames from 1 to $n$ is calculated and used to examine the track. For the oscillating bad track, although all the fitting errors are slightly smaller than the threshold, the mean is usually more than 60% of the threshold.

Combining both the one-point $n$ and multiple-point (1–$n$) checks provides a new advantage. We can set a large threshold in one-point check to allow the majority of the good tracks and some wrong ones to pass. This helps to make sure that the true high-acceleration events as part of the turbulence intermittency can be kept. Since the intermittent events will not last, it is unlikely that the good tracks with these events will produce a mean fit error that is as high as the bad tracks. Consequently, the wrong tracks that pass the one-point check will be removed in the multiple-point check.

## PARALLELIZATION

Although STB is much more computationally efficient than the tomographic reconstruction, its calculation is still the bottleneck of the entire experimental procedure as acquiring the high-speed video only takes seconds, transferring it only takes minutes, but STB will take hours to days depending on the number of frames, number of particles, calibration accuracy, and image noise level. Since STB involves many iterations in IPR and shaking, it is important to parallelize the code so that its performance in both, the multi-processor desktop and high-performance computing cluster can be optimized.

As listed in table 3.1, three steps are computationally expensive, stereomatching, particle-space correlation, and shaking. Each subroutine has to iterate over all the particles. Stereomatching and shaking also have to iterate over all the camera images for each particle. To simplify the discussion, we assume the number of camera is a constant of four.

If the total number of particles in each camera image is roughly equal to $N$, then the stereomatching step finds a match for each of the $N$ particles from images of all four cameras to generate 3D particle positions. For each camera, the extrusion of each particle center along the optical axis of the camera into the 3D space becomes an epipolar line, and this line can be projected onto the imaging planes of all other cameras. Within certain distance (proportional to

the calibration error) away from the epipolar line projection, $M$ particles will be found, and these are possible candidates. The complexity of the calculation grows roughly as $N^4$, as each of these candidates has to be projected back onto other cameras to confirm the match.

Another key step of STB is to establish the predictive field by using the particle-space correlation (Novara et al., 2016a); a step that identifies the velocity field based on particle displacement between two frames $n-1$ and $n$. As the displacement calculation involves correlating each particle in frame $n-1$ with another one in $n$, the calculation complexity grows as $N^2$.

The step of shaking can also be parallelized because it consists of several iterations for 3D position refinement and projections. To optimize the 3D particle location, they are iteratively "shaken" in 3D, starting from a large distance and gradually reduced to a smaller one. During each procedure, the updated 3D position will be projected onto all cameras in order to crosscheck with the actual particle images. The projection requires a 2D Gaussian calculation to represent the particle intensity profile. This calculation also scales with the total number of pixels that one particle occupies. In total, multiplying all the contributing factors results in a complex estimation of $432N$ for particles with an image diameter of 3 pixels.

Given the scope for parallelization in all the aforementioned time consuming steps of open-source STB, we adopted OpenMP for this purpose. It is not

the most efficient method, but it is easy to implement. It evenly assigns the number of loops onto every available thread, thereby reducing the processing time. A example of the total processing time for each step with one or six cores of the same desktop is listed in table 3.1. The dataset used for these tests is a synthetic data with 12,500 particles at a particle image density of 0.0125 ppp. A significant improvement of speed from parallelization can be noted in the table. For a higher particle image density, the time saved will increase even further.

**Table 3.1:** Processing time of stereomatching, particle-space correlation and shaking with parallelization

| | Stereomatching | Particle-space correlation | Shaking |
|---|---|---|---|
| Computation | $N \cdot M^4$ | $N^2$ | $432 \cdot N$ |
| One core (one thread used) (s) | 46 | 180 | 45 |
| Six cores (two threads per core) (s) | 14 | 20 | 7 |

The open-source STB can be run on different platforms, including HPC clusters. For example, the Maryland Advanced Research Computing Center(MARCC) is a cluster consisting of 23,000 cores with 2.6 GHz frequency. Besides the fact that the code can process each dataset using multiple processors on MARCC, many datasets can also be processed at the same time by submitting several jobs together through the system, which can further decrease the processing time.

PERFORMANCE EVALUATION

A performance test was conducted to evaluate different aspects of the open-source STB. Special attention has been paid to the uncertainty of the results and the efficiency of the algorithm.

### 3.0.3 Synthetic images

Synthetic images were generated by using an isotropic turbulence data from Johns Hopkins Turbulence database (JHTDB) (Li et al., 2008). Particles were tracked in the Lagrangian framework and their positions in each frame are projected onto four cameras with the image resolution 1024 $\times$ 1024 pixels. The particle intensity profile is assumed to follow a Gaussian function $I^i_{part}(x_i, y_i, p) = ae^{-(bx'^2+cy'^2)}$ with $x' = (x_i - x_{ip})\cos\alpha + (y_i - y_{ip})\sin\alpha$ and $y' = -(x_i - x_{ip})\sin\alpha + (y_i - y_{ip})\cos\alpha$. $(x_i, y_i)$ is the pixel position and $(x_{ip}, y_{ip})$ is the center of the particle $i$. Constants $a = 255$, $b = 0.9$, $c = 0.9$ and $\alpha = 0$ were used to simplify the particle intensity profile, and these parameters can be calibrated using the optical transfer function (Schanz et al., 2012) that is designed to specify the projection parameters in each sub-volume. The average diameter of particles is around 3 pixels. Three sets of synthetic images with image density of 0.0125, 0.025, and 0.05 ppp were created.

### 3.0.4 Evaluation metrics

To evaluate the quality of the tracking results, each track identified by STB will be matched with a synthetic track. Every particle on the matched track was compared with each other. Four parameters were calculated to evaluate the tracking results:

*Coverage*: For each track, coverage is the ratio between the number of frames that can be linked by STB and the ideal track length from the synthetic data.

*Matching error*: The matching error is the separation between detected and synthetic particles. It is related to both the calibration error and triangulation error.

*Fragmentation index*: This index measures the brokenness of a track. If one complete track in the synthetic data becomes two broken ones after STB, this number equals to two.

*Correctness*: This number measures the percentage of real (not ghost) particles. Ghost particles refer to particles that do not actually exist but appear during the reconstruction. A number smaller than one indicates the existence of ghost particles.

### 3.0.5 Evaluation results

Only the parameter *coverage* was discussed by Schanz, Gesemann, and Schröder (2016). In our case, the coverage reaches above 0.9991 even for images with image density as high as 0.05 ppp. Only 0.9% of particles are lost, which is slightly better than the 1.4% reported in Schanz, Gesemann, and Schröder (ibid.). This may be attributed to the improved linear fit that retains more correct tracks. The matching error is about 0.001 mm for all image densities, which is much smaller than the average particle displacement of 0.06 mm between two consecutive frames. The fragmentation index for all image densities is around 1.03, which is very close to the ideal case of 1, suggesting that STB can detect almost all tracks without any break in the ideal zero-noise synthetic datasets. Correctness is also 1 for all three cases, which is again expected for a perfect dataset.

The algorithm was tested on a simple desktop with Intel i7-8700 six-core 3.2 GHz processors. For images with 12,500 particles, the processing time per frame is around 5 s. In Schanz, Gesemann, and Schröder (ibid.), the code was run on a high-end server at that time with dual Intel Xeon E5-2680 ten-core processors at 2.8 GHz. The number of particles is 12,800, which is also similar to ours. The run time of our code is 40% faster than the one reported in Schanz, Gesemann, and Schröder (ibid.). The number of cores used in our case is smaller, but each with a higher processing frequency. Therefore this direct

comparison is not conclusive by any means because there are many things that are not controlled. But this at least suggests the performance of our code is comparable to, if not better than, the STB method reported by Schanz, Gesemann, and Schröder (2016).

The code has also been run on MARCC with ten jobs, and the processing time per frame reduces to 1.2 s. Since MARCC is relatively old cluster, the computing power of each core is significantly slower than ones in a desktop but multiple cores can be utilized to speed up the process.

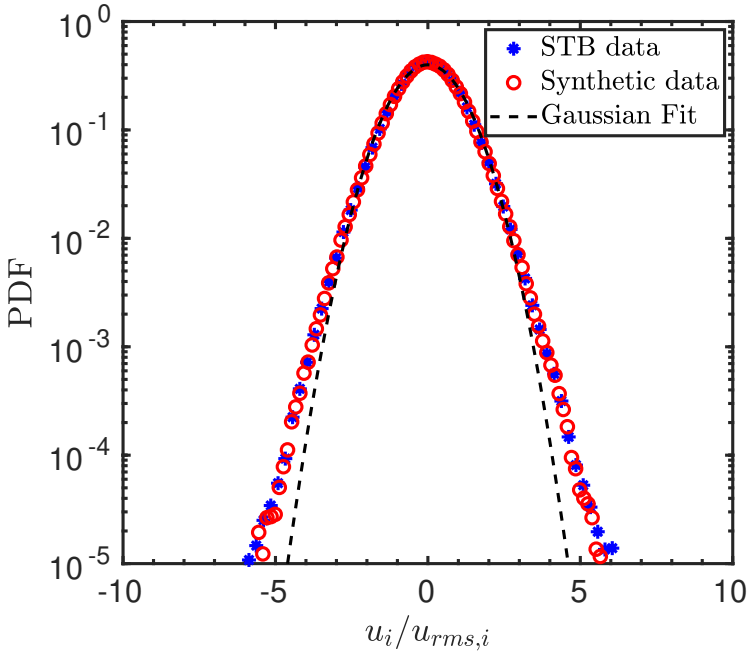


**Figure 3.3:** PDF of velocity fluctuation of both the synthetic data and the STB results at the particle image density of 0.05 ppp

The final test of comparing the probability density function (PDF) of the velocity fluctuation between the STB results and the simulation dataset with

0.05 ppp particle image density is shown in figure 3.3. It is clear that the blue symbols matches with the synthetic data very well, which shows that the open-source STB can accurately capture the flow characteristics.

---

## EXPERIMENTAL PROCEDURE

The open-source STB was applied to a dataset from the vertical water tunnel that was discussed in section 2. This tunnel was built to generate isotropic turbulence at a high energy dissipation rate. All eight faces of the octagonal test section were made of transparent acrylic plates. Four cameras were arranged around this test section with the top view shown in figure 3.4(a), along with a picture of the test section with three cameras in figure 3.4(b).

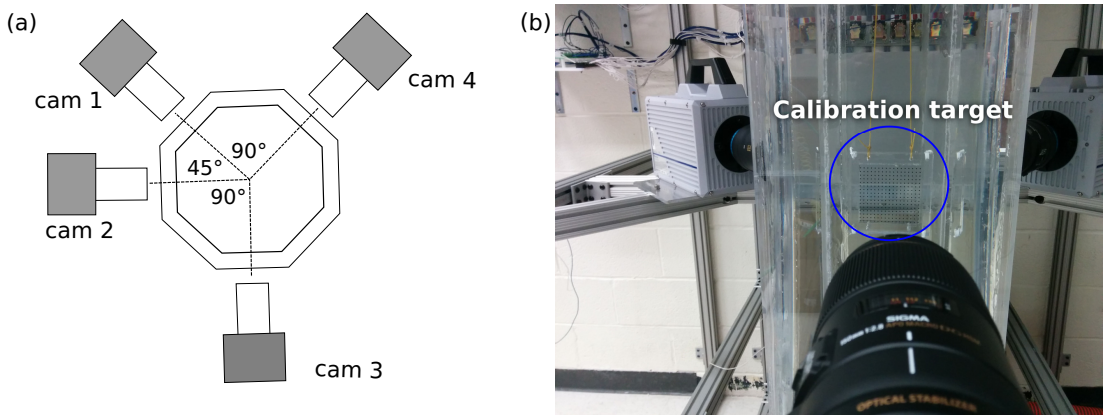


**Figure 3.4:** (a) A schematic showing the top-view of camera positions around the octagonal test section, (b) Picture of a transparent calibration target inside the setup along with the cameras and the test section

Many factors tend to affect the performance of STB, such as lighting in-

tensity, image noise, camera calibration, frame rate, particle size, and so on. Among those factors, the calibration step is the key, which requires special attention. In order to obtain accurate camera parameters for STB, an experimental procedure was designed as follows:

1. Calibrate all cameras simultaneously with a (transparent) calibration target.
2. Improve the calibration results using the Volume Self-calibration (VSC) on a dataset with a low image density of particles. Our VSC is different with the method introduced by Wieneke (2008).

   (i) Seed the flow with low-concentration of tracers so that the image density of particles on all cameras is below 0.001 ppp.

   (ii) Stir the flow and record the data; run STB on the data with a large search radius to find all the possible tracks. Keeping a low image density helps to make sure that all identified tracks are real, not ghost.

   (iii) Use the tracks that are longer than certain length to perform VSC.
3. Conduct another VSC on high-image-density datasets.

   (i) Directly conduct the actual experiment with the desired seeding density.

   (ii) Use a few frames to run STB and find tracks.

   (iii) Conduct VSC on detected tracks.

For the first step, calibration target is used. The target is an object with a

printed pattern (dots or checkerboard) of known positions on the surface(s). It helps to establish a correspondence between the 2D positions and 3D positions. With the cameras covering the entire perimeter of the test section, there will always be some cameras that have to look at the calibration pattern from the back side. For our experiments, a transparent calibration target was used. An array of dots with a spacing of 8 mm in both, $x$ and $z$ directions is laser etched on one side of the surface. The target is placed such that minimum number of cameras (only one in our case) view the target from behind. The refraction index of the material used for the target is different from that of water and thus causes calibration error. As shown in figure 3.5, for cameras vieweing the target from behind, although the blue points printed on the target have known 3D positions, they are not directly used for calibration. The positions that actually used for calibration are those "apparent points", where the extension of the light paths from the camera and target surface intersect, as shown by the red symbols. After the initial calibration, a code was used to correct the camera parameters based on the apparent points.

Tsai's model (Tsai, 1987) was used to obtain the camera transfer function in terms of camera parameters, including interior parameters, exterior parameters, and distortion coefficients. The least-square fit and nonlinear search algorithm were used to optimize the parameters on the plane where the calibration target was located. Off-plane points could have larger uncertainties

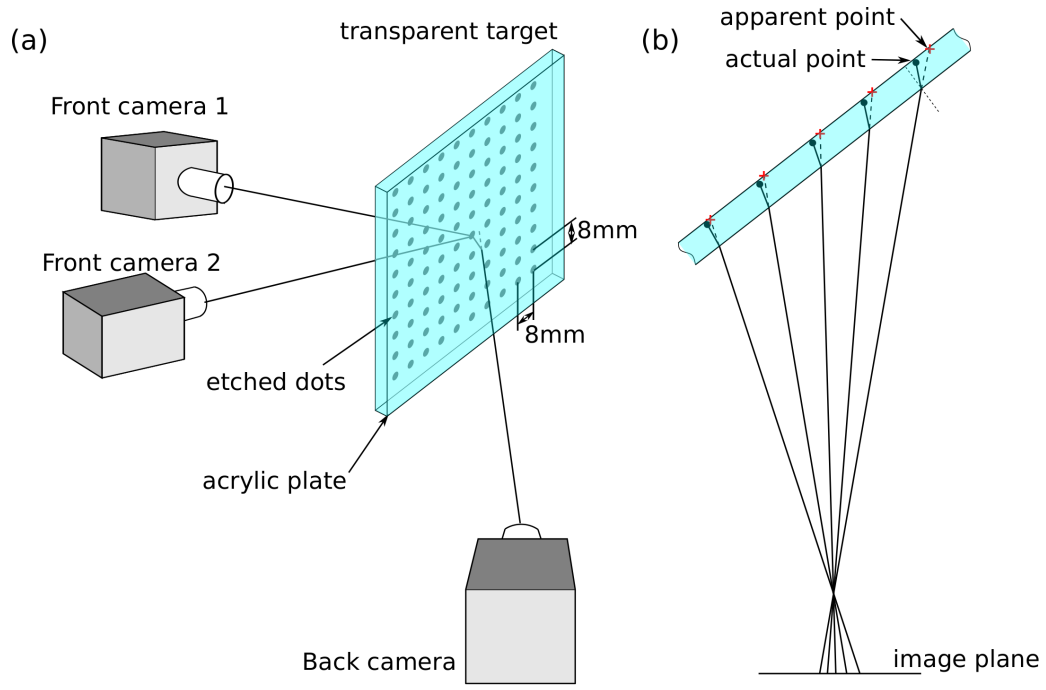


**Figure 3.5:** (a) the calibration configuration with two cameras looking at the printed dots from front and one camera viewing the pattern from behind through the transparent target (b) the difference between apparent points and actual calibration dots viewed by the back camera due to the mismatched refractive indices between the target and surrounding water.

and have to be optimized in a different way by using VSC.

Our VSC code is a non-linear optimization code to search for a set of camera parameters that help to minimize the triangulation error of all particles. To find particles with accurate positions, we require that (i) the particle image density is so low that there is no ambiguity and all particles reconstructed should be real even with a large search radius; (ii) the particles selected have to be relatively uniformly distributed throughout the entire view volume; and (iii) only particles that can be tracked for a long time will be used. After conducting VSC on the low-image-density data, the parameters should be accurate enough

to process the high-image-density data. VSC can be run one more time on the high-image-density data to further improve the camera parameters.

Figure 3.6 shows the PDF of the triangulation error $\epsilon$ before VSC and after two-rounds of VSC. The error systematically decreases from 0.0218 mm to 0.0186 mm after the low-image-density VSC, and continues to reduce to 0.0141 mm after the high-image-density VSC. The results show a significant improvement, and the level of improvement depends on the initial calibration and camera configuration.

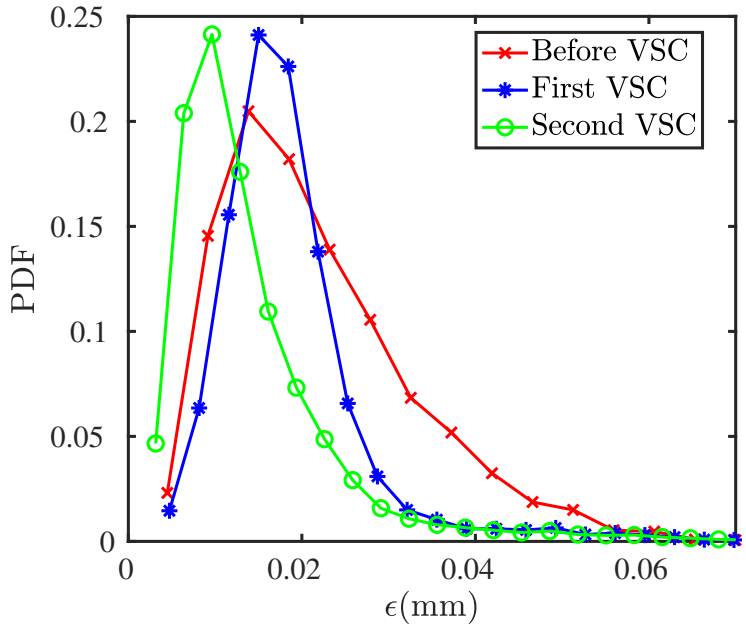


**Figure 3.6:** PDF of the triangulation error $\epsilon$ of particles after running VSC on the first low-image-density data and second high-image-density data

## PERFORMANCE ON EXPERIMENTAL DATA

An experiment was carried out in the vertical water tunnel according to the experimental procedure described in the section 3.0.5 and the data was processed with the open-source STB. The mean particle image density was 0.0195 ppp with a total of 9,600 particles in the view volume. Note that the total number of particles seem to be lower than the one reported by Schanz, Gesemann, and Schröder (2016). However, this dataset is imaged by using a back-lighting, which is subjected to higher image noise due to defocused particles outside the view volume. Trajectories over 50 frames are plotted in figure 3.7 color coded with their velocity magnitudes. Each trajectory was filtered by a Gaussian function to acquire smoothed position, velocity, and acceleration. The difference between the smoothed and raw positions is used to quantify the trajectory quality. For this test dataset, the averaged difference is around 0.01 mm, which is similar to the most probable triangulation error as shown in figure 3.6.

For each experiment, the camera memory can store 20,000 frames and for four high-speed cameras, it took about 4 seconds of data acquisition. The total data takes about 30 minutes to transfer to a local hard drive and another three hours to upload to MARCC. The processing time of one such dataset on MARCC is about one day if we run 10 jobs at the same time. If the calculation was instead directly performed on the desktop that had the data, the total run time

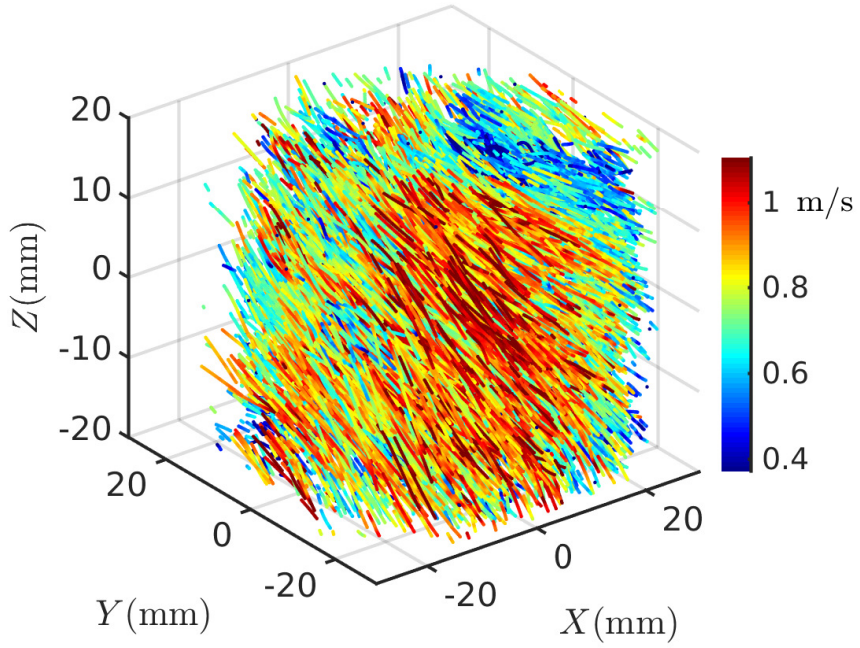


**Figure 3.7:** Sample trajectories from one experimental data at the image density of 0.0195 ppp

would be around four days, and that is only for one dataset taken within 4 s. This demonstrates the importance of performing data processing on a HPC. Another interesting finding is that the high-image-density datasets also make the post-processing slow, especially for statistics that need to take a pair of particles viz. structure function or particle dispersion statistics. Therefore, it makes sense to move the data analysis to HPC in order to make the entire process manageable.

## CONCLUSION

An open-source STB was developed and evaluated with three sets of synthetic images at the image density of 0.0125, 0.025 and 0.05 ppp. The results were evaluated with four metrics, including coverage, matching error, fragmentation index, and correctness. The evaluation shows that the open-source STB performs similarly to the original STB reported by Schanz, Gesemann, and Schröder (2016). The coverage can reach 0.999 even at an image density of 0.05 ppp. Both the fragmentation index and correctness also show that the open-source STB is robust and can produce almost perfect results for a noise-free synthetic dataset.

The advantage of the open-source STB is that it is parallelized and can be executed on a high-performance computing cluster. The resources on HPC enables running multiple data at the same time. Careful algorithm efficiency analysis and tests were conducted to evaluate the time consumed in each step. The processing time on a desktop of the open-source STB is 40% faster than the reported value on a high-end server that was used in 2016. When running on a HPC, the processing is faster by a factor of four. This number can be easily increased by running more jobs at the same time.

An in-house VSC code is also implemented for STB. The code is designed for improving camera calibration. In contrast to the VSC reported before, the de-

signed VSC needs to run on a low-image-density data before running it again on a high-image-density data in order to ensure an improvement in the calibration.

Finally, the code was tested on an experimental dataset with 0.0195 ppp particle image density on noise particle shadow images, showing promising results. We hope that this open-source STB, available for public use on the GitHub repository Tan (2020 (accessed June 10, 2020)), will be of value to the community for algorithm development, data assimilation, and uncertainty analysis.

# Chapter 4

# Lift and drag coefficients of deformable bubbles in intense turbulence determined from bubble rise velocity

*We experimentally investigate the rise velocity of finite-sized bubbles in turbulence with a high energy dissipation rate of* $\epsilon \sim 0.5\ m^2/s^3$*. In contrast to a 30-40% reduction in rise velocity previously reported in weak turbulence (the Weber number* ($We$) *is much smaller than the Eötvös number* ($Eo$); $We \ll 1 < Eo$*), the bubble rise velocity in intense turbulence shows a surprising new behavior: an abrupt transition from an order of magnitude slower to a factor of two faster than rising in an otherwise quiescent medium. This transition occurs where* $We$ *increases from below one to above one, underscoring the key role played by the turbulence-induced deformation. We also formulate a model based on bubble-*

*eddy coupling, and the results show excellent agreement with not only our data in intense turbulence but also other works in weak turbulence. The model also helps us to extract the lift and drag coefficients of bubbles in intense turbulence for a wide range of Weber and Reynolds numbers in situ.*

---

## INTRODUCTION

Leonardo da Vinci's famous drawing of bubbles entrained in turbulent water as it falls from a sluice into a pool clearly depicts a sophisticated interaction between organized turbulence structures and bubbles. This complex interaction has inspired decades of seemingly-parallel research on (i) coherent structures, which are often described as "eddies" or "vortices", in turbulence (She, Jackson, and Orszag, 1990) and (ii) the non-rectilinear rising motion of finite-sized deformable bubbles (Magnaudet and Eames, 2000; Mougin and Magnaudet, 2001; Ern et al., 2012). Although each subject represents a complex problem in and of itself, the coupling between them (Lohse, 2018; Mathai, Lohse, and Sun, 2020)—especially as bubbles get deformed by the nearby turbulent eddies—poses formidable challenges in relation to many applications, including aerobic reactors (Kawase and Moo-Young, 1990) and bubble-mediated gas transfer in the ocean (Woolf, 1997; Boettcher, Fineberg,

and Lathrop, 2000).

In turbulence, the bubble-vortex interaction is known to affect the ensemble-averaged mean bubble rise velocity $\langle w_b \rangle$. Wang and Maxey (1993b) showed that $\langle w_b \rangle$ of micro-bubbles in forced isotropic turbulence decreases by $33\%$ when compared to that seen in an otherwise quiescent medium, and this difference was attributed to bubbles being trapped in high-vorticity, low-pressure vortex cores. Spelt and Biesheuvel (1997) proposed a different mechanism, suggesting that bubbles tend to preferentially sample the downward flows in turbulence, which effectively reduces $\langle w_b \rangle$ by up to 50%. In addition to these simulation results, similar experimental studies were also carried out by measuring $\langle w_b \rangle$ in water tunnels driven by passive (Aliseda and Lasheras, 2011) or active grids (Poorte and Biesheuvel, 2002; Prakash et al., 2012). Despite the difference in bubble sizes (0.5 mm–1.5 mm), the findings are both qualitatively and quantitatively consistent with the numerical results. These results support the notion that $\langle w_b \rangle$ decreases due to either vortex trapping or preferential sampling.

Bubbles traveling in turbulence are subjected to multiple hydrodynamic forces including buoyancy, drag, lift, added mass, Basset history, and pressure forces (Magnaudet and Eames, 2000; Sridhar and Katz, 1995). It is often difficult to isolate the effects of individual forces on $\langle w_b \rangle$ from experimental results because, compared with the number of unknowns, not many quantities can be directly measured. Mazzitelli, Lohse, and Toschi (2003) performed direct nu-

merical simulations (DNS) to account for two-way couplings. By switching the lift force on and off, they demonstrated that the addition of lift force enhances the probability of bubbles preferentially sampling downward flows in turbulence. When lift was turned off, the bubbles accumulated at the center of the eddies (Wang and Maxey, 1993b).

Loisy and Naso (2017) conducted a DNS of deformable bubbles rising in turbulence. Their work confirmed the earlier results obtained by Wang and Maxey (1993b) and Spelt and Biesheuvel (1997), indicating that both preferential sampling and vortex trapping are present in turbulent bubbly flows. Furthermore, they suggested that the velocity ratio $\beta = u'/\langle w_b \rangle$ ($u'$ is the turbulent fluctuation velocity) determines which mechanism is at play. The reduction in velocity is primarily driven by preferential downward sampling for $\beta < 1$, whereas vortex trapping dominates for $\beta > 1$.

Most prior studies have focused on understanding the bubble dynamics in high-$Re_\lambda$ turbulence ($Re_\lambda = u'\lambda/\nu$), where $\lambda$ is the Taylor micro-scale and $\nu$ is the kinematic viscosity. $u'$ is the velocity scale that is typically associated with eddies of size $L$ (the integral length scale) (Frisch, 1995). However, bubbles with size $D$ in the inertial subrange ($\eta \ll D \ll L$, $\eta$ is the Kolmogorov length scale) interact more frequently with eddies of a similar size $D$ rather than with flow structures much larger or much smaller. Based on this argument, a more relevant velocity scale would be the eddy velocity scale at the bubble

size: $u_D \sim (\epsilon D)^{1/3}$ (Frisch, 1995). In most previous experiments conducted in systems with small $\epsilon$, the bubble rise velocity $\langle w_b \rangle$ is much larger than $u_D$, which indicates that the bubble dynamics is primarily dominated by buoyancy rather than turbulence.

The objective of this research is to experimentally study $\langle w_b \rangle$ of finite-sized bubbles in a different regime $\langle w_b \rangle / u_D 1$. It happens that, in this regime, bubble deformation induced by turbulence starts to become important. In §4, the relevant dimensionless numbers will be introduced and explained. In §4, we provide in-depth discussions of our two-phase simultaneous measurements. Details concerning the data analysis process and a simple model are then addressed in §4. In particular, we describe how we extract the lift and drag coefficients of deforming bubbles in turbulence.

---

## DIMENSIONLESS NUMBERS

The first dimensionless number that comes to mind for virtually any fluid dynamics problems is the Reynolds number, more specifically the Taylor-scale Reynolds number $R_\lambda$ as is customary in homogeneous and isotropic turbulence. $R_\lambda$ sets the scale separation between $L$ and $\eta$. In the context of bubble dynamics in turbulence, as long as $R_\lambda$ is large enough so that $\eta \ll D \ll L$ is satisfied, $R_\lambda$

is not important.

For bubbles with $\langle w_b \rangle / u_D 1$, turbulence stresses turn out to be sufficiently large to deform bubbles. The key dimensionless number to quantify deformation is the Weber number, $We = 2.13\rho(\epsilon D)^{2/3} D/\sigma$ (2.13 is the Kolmogorov constant for the second-order longitudinal structure function), which measures the ratio between the dynamic pressure gradients and the restoring Laplace pressure driven by the surface tension (Kolmogorov, 1949; Hinze, 1955). When $We 1$, the turbulence-induced deformation starts to become important. Meanwhile, given that we focus primarily on air bubbles in water with large density difference between the two phases, the buoyancy-induced deformation, measured by the Eötvös number $Eo = \Delta\rho g D^2/\sigma$, could also be important.

For weak turbulence (small $\epsilon$; $\epsilon \ll 0.5$ m$^2$/s$^3$), millimeter-sized bubbles are either solely deformed by buoyancy $Eo > 1 \gg We$ or completely spherical $1 > Eo \gg We$. Since $We \sim D^{5/3}$, $We$ can be larger than one for large centimeter-sized bubbles, which may lead to a conclusion that the turbulence-induced deformation can still be important in weak turbulence. However, $Eo \sim D^2$ grows faster than $We$ as $D$ increases; for bubbles with $We > 1$ in weak turbulence, their $Eo$ is significantly larger. For example, in turbulence with $\epsilon \approx 10^{-3}$ m$^2$/s$^3$ (Mercado et al., 2012), $We$ becomes larger than one if $D > 33$ mm. At that size, $Eo = 148$, which is more than two orders of magnitude larger than $We$, indicating a dominant role played by buoyancy.

The turbulence-induced deformation starts to play a role if $WeEo > 1$. This relationship can actually be solved to determine the range of the bubble size and minimum $\epsilon$ needed: $\epsilon > 0.57$ m$^2$/s$^3$. Much lower than this number, bubbles will either stay spherical or be deformed primarily by buoyancy, never by turbulence, regardless of the bubble size. Throughout the rest of this chapter, weak turbulence refers to turbulence with low $\epsilon \ll 0.5$ m$^2$/s$^3$, which also means $Eo \gg We$ and $We \ll 1$. Strong turbulence represents turbulence with high $\epsilon \sim 0.5$ m$^2$/s$^3$. At this $\epsilon$, there will be a range of bubble sizes ($D \approx 2$–3 mm) that satisfies the criterion of $We \sim Eo > 1$.

It would be tempting to relate the non-dimensionalized velocity $\langle w_b \rangle / u_D$ to either $We$ or $Eo$. But it is easy to show that $Eo/We = (\langle w_b \rangle / u_D)^2 / 2.13$ if $\langle w_b \rangle = \sqrt{gD}$. This relationship implies that these dimensionless groups are not independent. In other words, $\langle w_b \rangle / u_D < 1$ and $We > Eo$ are equivalent conditions. So rather than adopting the dimensionless forms, in this work, we decide to present $\langle w_b \rangle$ as a function of bubble physical size $D$. Nevertheless, the dimensionless lift and drag coefficients can still be linked to $We$, $Eo$, and the bubble-scale Reynolds number $Re_b$.

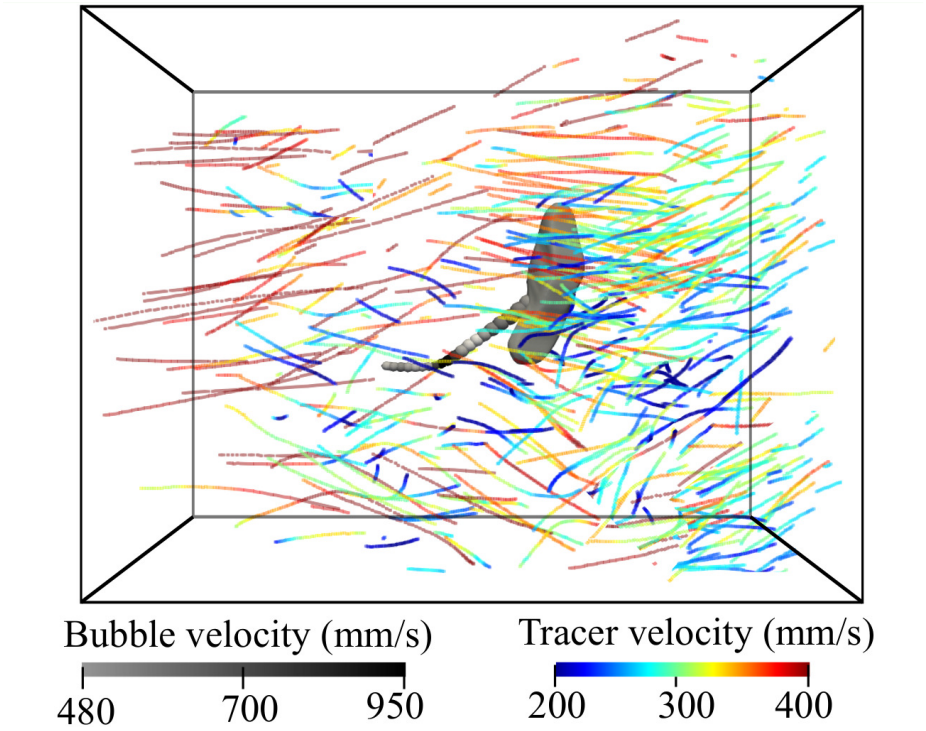


**Figure 4.1:** (Sample of reconstructed 3D tracer tracks around a bubble (Masuk, Salibindla, and Ni, 2019). The instantaneous velocity magnitude of both the bubble and surrounding tracers are color coded.

.

## EXPERIMENTALLY MEASURED QUANTITIES

The experiments were conducted in the V-ONSET setup that was discussed in section §2. Furthermore, in section §2.0.3, we mentioned that six high-speed cameras were used to capture the flow via back-lighting that simultaneously casts a shadow of the bubbles and surrounding tracer particles onto the cameras. The collected images were processed by a virtual-camera visual hull method (Masuk, Salibindla, and Ni, 2019) to optimize the geometry by enforcing constraints imposed by the surface tension. After reconstruction, we tracked the center of mass of roughly 47,000 bubbles (an example of such is shown in figure 4.1). The trajectory of each bubble, on average, consists of 200–250 frames. In total, about $10^7$ data points of the local vertical bubble velocity $u_{z,b}$ were collected. Simultaneously, the mean volumetric flow rate of water through the tunnel is monitored by a digital flow meter, from which the mean vertical flow velocity $\overline{w}$, averaged over the entire cross section, can be determined. $\overline{w}$ has to be subtracted from $u_{z,b}$ to obtain the bubble rise velocity $w_b = u_{z,b} - \overline{w}$.

In addition, in each frame, over 7,000 tracer particles were tracked simultaneously using our in-house high-concentration particle tracking code (Tan et al., 2020a, 2019). A snapshot of our 3D reconstructed results, including both 3D bubble geometry and 3D tracks of surrounding tracers, is shown in figure

4.1. Within a certain search radius (SR=1.5–3 D) from the center of a bubble, $N$ tracer particles can be identified ($N$ ranges from 5 to 30 particles). Averaging the velocity of all these tracer particles $u^p_{z,l}$ helps to estimate the local flow velocity $u_{z,l} = \sum_{p=1}^{N} u^p_{z,l}/N$ at the center of the bubble. In the governing equation (equation 4.1 in Sec. §4) for bubbles (Magnaudet and Eames, 2000), it is clearly stated that the fluid velocity used has to be the unperturbed ambient flow taken at the center of a bubble if the bubble was not there. The local flow velocity $\overline{w_s}$, averaged across a small region where bubbles passed by, is found to be larger than $\overline{w}$ for the remaining regions because rising bubbles always drag surrounding fluid with them (Liu et al., 2005; Lewandowski et al., 2018; Risso, 2018). This perturbed flow $\overline{w_s}$ has to be subtracted from $u_{z,l}$ to estimate the unperturbed vertical flow velocity, i.e. $w_l = u_{z,l} - \overline{w_s}$.

---

## RESULTS AND DISCUSSION

Figure 4.2 shows the ensemble average of bubble rise velocity $\langle w_b \rangle$ as a function of bubble size. Three groups of data, including bubbles rising in a quiescent medium (Clift, Grace, and Weber, 2005), weak turbulence ($We \ll Eo$, $\epsilon = 1.3\times10^{-4}$–$6\times10^{-3}$ m$^2$/s$^3$) (Poorte and Biesheuvel, 2002; Prakash et al., 2012; Aliseda and Lasheras, 2011), and our experiments (strong turbulence, $\epsilon = 0.5$

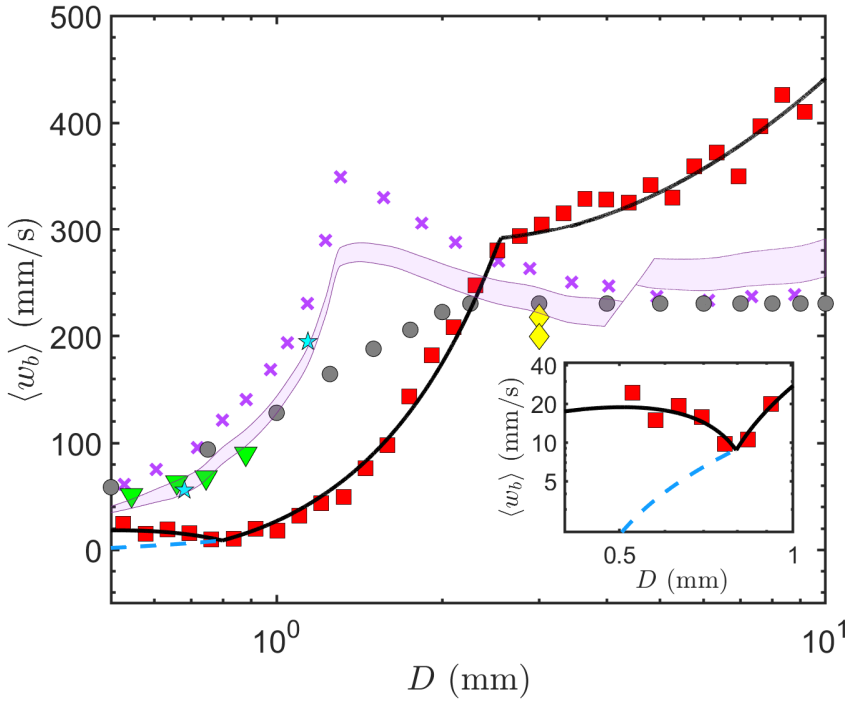


**Figure 4.2:** Mean bubble rise velocity $\langle w_b \rangle$ as a function of bubble diameter $D$ in purified water (Clift, Grace, and Weber, 2005)(purple crosses); contaminated water (Clift, Grace, and Weber, 2005)(grey circles); weak turbulence ($We \ll 1 < Eo$), including Aliseda and Lasheras (2011)(green down triangles), Poorte and Biesheuvel (2002)(cyan stars), and Prakash et al. (2012)(yellow diamonds); and our experiments for intense turbulence (red squares). Lines represent the model prediction for different conditions. The solid black line is calculated from our model, based on equations 4.3 –4.5 at a high $\epsilon = 0.5$ m$^2$/s$^3$. The purple shaded area represents the model prediction for weak turbulence ($We \ll 1 < Eo$) with $\epsilon = 1.3 \times 10^{-4}$–$6 \times 10^{-3}$ m$^2$/s$^3$ in clean water. Inset: It shows the same model prediction but using two lift models as shown in equation 4.8 and figure 4.3(b).

$m^2/s^3$), are shown and compared to each other. For bubbles rising in a quiescent medium, $\langle w_b \rangle$ of small bubbles increases as $D$ grows because of buoyancy. For large bubbles, the pressure drag induced by flow separation and wake formation limits $\langle w_b \rangle$. When the background flow becomes weakly turbulent, $\langle w_b \rangle$ still maintains a trend similar to what has been observed for bubbles rising in an otherwise quiescent medium, but the magnitude is about 30–40 % smaller.

Once $\epsilon$ reaches 0.5 $m^2/s^3$ ($We$ becomes important), a clear deviation from both the quiescent and weakly turbulent cases is observed; not just the magnitude, the entire dependence of $\langle w_b \rangle$ on the bubble size $D$ is altered. Three regimes are clearly observed: (i) $\langle w_b \rangle$ drops by a factor of two as $D$ grows from 0.5 mm (13.5 $\eta$) to 0.8 mm (21.3 $\eta$), as shown in the inset of figure 4.2; (ii) $\langle w_b \rangle$ increases by over an order of magnitude for $D$ =0.8–2.2 mm (21.3–58.5 $\eta$); at 2.2 mm, $\langle w_b \rangle$ finally recovers the value in a quiescent medium; (iii) For $D$ =2.2–10 mm (58.5–266 $\eta$), $\langle w_b \rangle$ continues to grow, exceeding the bubble rise velocity in a quiescent medium, although at a reduced growth rate. In sum, $\langle w_b \rangle$ varies from a factor of 11 (small bubbles) below that in a quiescent medium to almost two times above.

The observed change of $\langle w_b \rangle$ in intense turbulence must be a result of the coupling between bubbles and surrounding turbulent flows. To estimate the nearby flow velocity, similar to $\langle w_b \rangle$, $\langle w_l \rangle$ is determined by performing an ensemble average of $w_l$ over all bubbles of a particular size $D$. Figure 4.3(a)

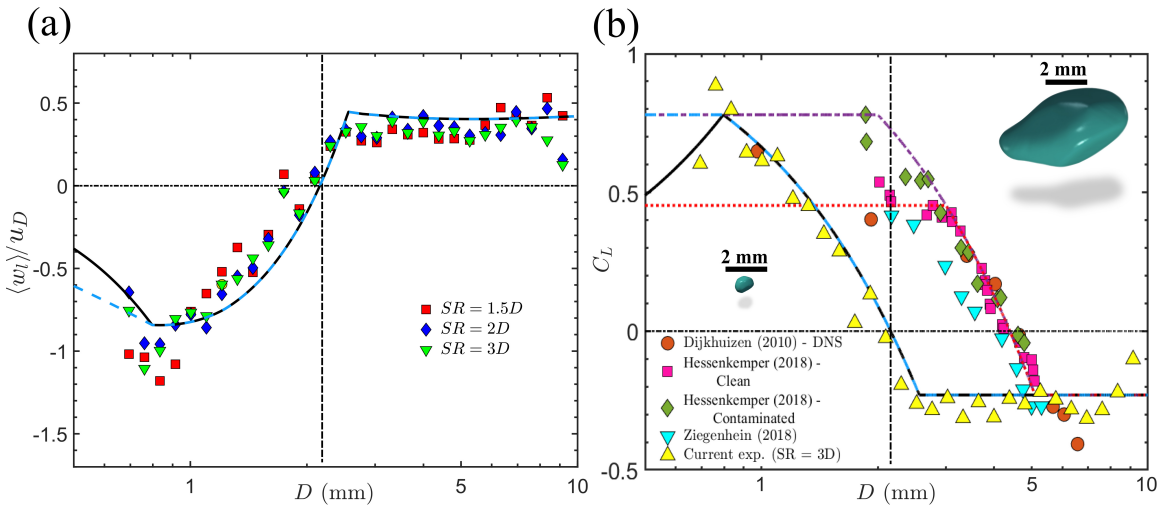


**Figure 4.3:** (a) The normalized mean vertical flow velocity $\langle w_l \rangle$ as a function of the bubble size $D$. $\langle w_l \rangle$ are calculated based on three different search radii (SR) to find tracer particles around bubbles. (b) The lift coefficient $C_L$ as a function of bubble size. Yellow triangle is obtained from $\langle w_l \rangle$ and $\langle w_b \rangle$ based on equation 4.4. Other symbols represent results from laminar shear flows for air-water systems, which were fitted with a piece-wise linear function for purified (dotted red line, equation 4.6) and contaminated water (dash-dotted purple line, equation 4.7). Cyan dashed line and black solid line (equation 4.9) are the revised lift models for intense turbulence. The vertical dashed lines in both plots mark the transition point where turbulence-based $We$ increases beyond 1. Two 3D green blobs show the reconstructed 3D shape of small and large bubbles.

shows $\langle w_l \rangle$ as a function of the bubble size $D$. $\langle w_l \rangle$ being negative for small bubbles clearly shows that the nearby flows around small bubbles, on average, move downward. $\langle w_l \rangle$ increases, crosses zero, and finally becomes positive as $D$ grows, implying that the flows switch from hindering to assisting the rising motion of bubbles, which qualitatively explains why $\langle w_b \rangle$ exhibits such a dramatic change in figure 4.2. Different symbols in figure 4.3(a) correspond to different search radii (SR) used for selecting tracer particles around a bubble to estimate $w_l$. Note that very few particles can be triangulated within $1D$ away from the bubble center as tracers close to a bubble can be easily shadowed by the bubble itself. Nevertheless, as flows in the close vicinity of a bubble (SR$< 1D$) are heavily modulated by the bubble motion, excluding these tracers from the statistics could help to avoid the statistical bias. From SR = 1.5D to 3D, although with some variations, the observed trend of $\langle w_l \rangle$ seems to be consistent and insensitive to SR for bubbles with $D > 1$ mm. As SR also affects the number of tracer particles included for calculating $\langle w_l \rangle$, this consistent trend also implies well-converged statistics for bubbles with $D > 1$ mm. For small bubbles, results become sensitive to $SR$ because of the insufficient number of tracers found within such a small $SR$.

Independent measurements of bubbles and surrounding tracers provide a consistent picture that bubbles of different sizes seem to be preferentially swept to regions with apparently opposing flow directions. The proposed mechanism

of preferential sampling seems to be borne out by the observed trend of $\langle w_l \rangle$. The surprising new finding is that bubbles do not always preferentially sample the downward flow side; The flow direction can be reversed for bubbles of large sizes. On the other hand, it may also imply that the vortex trapping idea does not apply to large bubbles, as vortex trapping is often linked to the pressure gradient force without considering the lift force. As a result, bubbles of all sizes would end up being trapped in the center of eddies with an overall reduced rise velocity, which does not agree with our observation.

To understand the reason behind the reversal of the preferential sampling direction, we start from the governing equation for finite-sized bubbles reported in equation 1.9:

$$V_b(\rho_b + C_A\rho_l)\frac{D\mathbf{u}_b}{Dt} = \rho_l V_b C_A \frac{D\mathbf{u}_l}{Dt} + V_b(\rho_l - \rho_b)g\hat{\mathbf{e}}_z + \frac{\rho_l}{2}AC_D(\mathbf{u}_l - \mathbf{u}_b)|\mathbf{u}_l - \mathbf{u}_b| + \rho_l C_L(\mathbf{u}_l - \mathbf{u}_b) \times (\nabla \times \mathbf{u}_l) - \frac{1}{2}V_b\nabla P_w + \mathbf{F}_b \tag{4.1}$$

where $\rho_l$ and $\rho_b$ are the density of water and gas, respectively. $V_b$ is bubble volume; A is the projected area of a sphere with an equivalent volume of the bubble. $\mathbf{u}_l$ is the velocity of the unperturbed ambient flow taken at the centre of the bubble; $\mathbf{F}_b$ is the Basset history force. $C_D$, $C_L$, and $C_A$ are the drag coefficient, lift coefficient, and added mass coefficient, respectively.

Taking an ensemble average of both sides of equation 4.1 yields

$$0 = V_b(\rho_l - \rho_b)g\hat{\mathbf{e}}_z + \frac{\rho_l}{2}AC_D\langle(\mathbf{u}_l - \mathbf{u}_b)|\mathbf{u}_l - \mathbf{u}_b|\rangle + \rho_l C_L\langle(\mathbf{u}_l - \mathbf{u}_b)\times(\nabla\times\mathbf{u}_l)\rangle - \frac{1}{2}V_b\langle\nabla P_w\rangle \tag{4.2}$$

as $\langle D\mathbf{u}_l/Dt\rangle = 0$ and $\langle D\mathbf{u}_b/Dt\rangle = 0$ in homogeneous and isotropic turbulence, and the unsteady forces, including added mass and the Basset history force, become zero. In addition, the slip velocity between the two phases $\langle\mathbf{u}_l - \mathbf{u}_b\rangle$ is zero along the lateral directions and nonzero only along the vertical direction, which have been directly calculated from experiments and confirmed: $\langle\mathbf{u}_l - \mathbf{u}_b\rangle = \langle(w_l - w_b)\rangle = \langle w_l\rangle - \langle w_b\rangle$. The same principle applies to $\langle(\mathbf{u}_l - \mathbf{u}_b)|\mathbf{u}_l - \mathbf{u}_b|\rangle$: only the vertical direction survives after the ensemble average: $\langle(\mathbf{u}_l - \mathbf{u}_b)|\mathbf{u}_l - \mathbf{u}_b|\rangle \approx (\langle w_b\rangle - \langle w_l\rangle)^2$.

The remaining two terms, both lift and the pressure force, are associated with $\langle\nabla\times\mathbf{u}_l\rangle$. We assume that the interaction between a bubble and its surrounding flows can be modeled as a bubble interacting with local shear with shear rate of $\gamma = \langle\nabla\times\mathbf{u}_l\rangle = d\langle w_l\rangle/dx$, as depicted in figure 4.4. In the mean pressure force $\mathbf{F}_p = V_b\langle\nabla P_w/2\rangle$, solving the Poisson equation for pressure yields $\nabla P_w = \partial P_w(x)/\partial x = \rho_l\gamma^2 x\hat{\mathbf{e}_x}$. It indicates that the pressure force acts mainly along the horizontal direction $\hat{\mathbf{e}_x}$. For the same configuration, the ensemble average of lift $\mathbf{F}_L = \rho_l C_L(\mathbf{u}_l - \mathbf{u}_b)\times(\nabla\times\mathbf{u}_l)$ can be approximated as $\rho_l C_L(\langle w_l\rangle -$

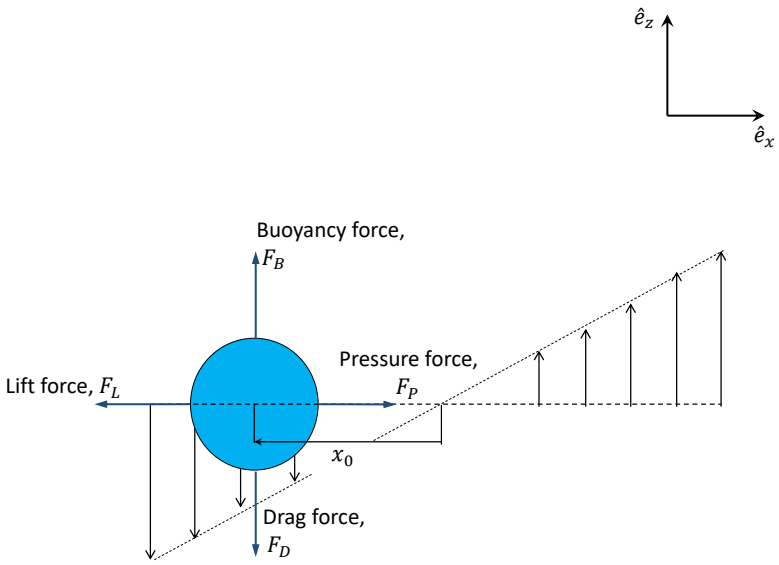


**Figure 4.4:** Schematic of a model for bubble interacting with a uniform shear flow of constant shear rate ($\gamma$) to represent the ensemble-averaged bubble-eddy interaction. Four forces experienced by the bubble in equation 4.2 must balance with each other along two orthogonal directions.

$\langle w_b \rangle)|\gamma|\hat{\mathbf{e_x}}$. In figure 4.4, it may seem that we picked the flow orientation so that the direction of $\mathbf{F_L}$, i.e. $\hat{\mathbf{e_x}}$, aligns with that of $\mathbf{F}_p$. But this is not a coincidence. As shown in the vector equation 4.2, out of four terms, buoyancy and the ensemble-averaged drag are along the vertical direction, $\hat{\mathbf{e_z}}$ . The remaining two terms either have to share the same direction, or both of them have to be zero.

Following this argument, equation 4.2 can be written as two explicit equations along the vertical and lateral directions:

$$V_b(\rho_l - \rho_b)g\hat{\mathbf{e}}_z = \frac{1}{2}AC_D(\langle w_b \rangle - \langle w_l \rangle)^2\hat{\mathbf{e_z}} \tag{4.3}$$

$$\rho_l C_L(\langle w_l \rangle - \langle w_b \rangle)|\gamma|\hat{\mathbf{e_x}} = \rho_l \gamma^2 x_0 \hat{\mathbf{e_x}} \tag{4.4}$$

where $x_0$ represents the steady lateral location of bubbles within the shear flow (figure 4.4). The mean flow velocity $\langle w_l \rangle$ at this location can be calculated:

$$\langle w_l \rangle = \gamma x_0 \tag{4.5}$$

Positive or negative values of $x_0$ represent a bubble being swept to the upward or downward side of the shear, respectively. $\gamma$ scales with the velocity gradient of scale $D$, which can be related to the transverse second-order structure function $D_{NN} = 4(\epsilon D)^{2/3}/3$ in the form of $\gamma \sim 2(\sqrt{D_{NN}})/D = \sqrt{16/3}(\epsilon/D^2)^{1/3}$.

This is where $\epsilon$ enters the model.

Equations 4.3 to 4.5 provide a simple model for the ensemble-averaged fluid and bubble velocity, which can be measured directly from our experiments. There are three unknowns in these three equations: $C_D$, $C_L$, and $x_0$. This indicates that these three unknowns can be linked to the measured results exactly without any fitting parameters. Solving these linear equations is straightforward. For example, from equation 4.4, $x_0 = C_L(\langle w_l \rangle - \langle w_b \rangle)/\gamma$. As shown in figure 4.4, once $x_0$ is known based on equation 4.5, the flow velocity experienced by bubbles is simply the velocity at location $x_0$: $\langle w_l \rangle = \gamma x_0 = C_L(\langle w_l \rangle - \langle w_b \rangle)$.

This relationship suggests that $C_L$ can be directly obtained from our measurements of $\langle w_l \rangle$ and $\langle w_b \rangle$. The results are shown as yellow triangles in figure 4.3(b). Only one search radius $SR = 3D$ is used as $\langle w_l \rangle$ is not very sensitive to $SR$. For small bubbles ($D < 2$ mm), $C_L$ is positive. As $D$ increases, $C_L$ continues to drop until it reaches a negative value of -0.23. This transition indicates an inversion of the direction of this lateral lift.

Similar lift direction inversion has also been observed in different types of flows: bubbles rising in laminar shear flows (Tomiyama et al., 2002; Dijkhuizen, Sint Annaland, and Kuipers, 2010; Hessenkemper, Ziegenhein, and Lucas, 2019; Ziegenhein, Tomiyama, and Lucas, 2018) and bubbles in channel flows (Lu and Tryggvason, 2013, 2008; Dabiri, Lu, and Tryggvason, 2013). Although neither one of these two cases is turbulent, the mean shear is large

enough to allow for the lift force to drive bubbles in the lateral directions. It was shown that small spherical bubbles tend to migrate towards low-speed side whereas large deforming bubbles favor the opposing high-speed side (Tomiyama et al., 2002) because of the interaction between shear and bubble deformation (Lu and Tryggvason, 2008; Adoua, Legendre, and Magnaudet, 2009). Although no mean shear exists in our system—flow is close to homogeneous and isotropic (Masuk et al., 2019)—deformable bubbles could respond to the local shear created by turbulent eddies.

To compare $C_L$ in the two systems more quantitatively, in figure 4.3(b), several recent datasets of $C_L$ for bubbles rising in laminar shear flows (limited to air-water systems) (Dijkhuizen, Sint Annaland, and Kuipers, 2010; Hessenkemper, Ziegenhein, and Lucas, 2019; Ziegenhein, Tomiyama, and Lucas, 2018) are also shown. All results are consistent—$C_L$ decays as $D$ grows and eventually it becomes negative, which marks the direction reversal of the bubble transverse migration driven by lift. The transition location of $C_L$ is believed to be associated with the buoyancy-induced deformation measured by $Eo$.

$C_L$ inversion seems to occur at a larger $D$ for the buoyancy-induced deformation than for the turbulence-driven cases. This difference can be attributed to different driving mechanisms of bubble deformation. In laminar shear flows, bubble deformation is only driven by buoyancy, measured by $Eo$. In our experiments, the lift inversion occurs when the bubble size increases from $2.2$

($We = 0.71$) to 2.7 mm ($We = 1.00$). As $We$ crosses from below to above one, turbulence-induced bubble deformation becomes important. Note that this $We$ does not account for bubble slip velocity or turbulence intermittency, which will only intensify the turbulence-induced deformation. Nevertheless, even without other compounding effects, this Weber number alone already indicates a possibility of an early lift inversion thanks to turbulence.

Other than the transition diameter, the trend of $C_L$ from our experiments is very similar to that from laminar shear flows, both of which can be fitted with piece-wise linear functions. For laminar shear flows, given the difference between contaminated water and purified water, two separate fits can be provided:

$$C_L = \begin{cases} 0.45, & Eo < 1.25 \text{ (pure water)} \\ 1.453 - 0.9\sqrt{Eo} & 1.25 < Eo < 4 \\ -0.23 & 4 < Eo \end{cases} \tag{4.6}$$

$$C_L = \begin{cases} 0.78, & Eo < 0.5 \text{ (contaminated)} \\ 1.453 - 0.9\sqrt{Eo} & 0.5 < Eo < 4 \\ -0.23 & 4 < Eo \end{cases} \tag{4.7}$$

In figure 4.3(b), equations 4.6 and 4.7 are shown as the red dotted line and purple dash-dotted line, respectively. The two equations are essentially the

same; the only difference resides at the small-$Eo$ limit. Note that these two equations are different from the proposed more complicated correlations by Tomiyama et al. (2002), Hibiki and Ishii (2007), and Legendre and Magnaudet (1998); and Dijkhuizen, Sint Annaland, and Kuipers (2010) (All these proposed models are not compatible among themselves). But the piece-wise linear correlations provide equally good fits for the data.

When turbulence becomes important ($WeEo$), the lift equation is adjusted to using $We$ rather than $Eo$. Since many tracer particles are present in our system, bubble behaviors in our system should be similar to that in a contaminated case (equation 4.7). Based on this argument, by adopting the same two limiting values of $C_L$ from equation 4.7, a new equation of $C_L$ for the turbulence-induced deformation is obtained:

$$C_L = \begin{cases} 0.78 \quad (2.671We^{3/5}) & We < 0.1, \\ 1.25 - 1.608We^{3/5} & 0.1 < We < 0.9 \\ -0.23 & 0.9 < We \end{cases} \tag{4.8}$$

The equation is shown as the cyan dashed line in figure 4.3(b). Equation 4.8 seems to agree with the data very well. Note that both equations 4.7 and 4.8 are piece-wise linear as a function of the bubble size $D$. Once $Eo$ and $We$ are used, the equations become dependent on $\sqrt{Eo}$ and $We^{3/5}$ simply because $Eo \sim D^2$ and $We \sim D^{5/3}$.

The agreement between equation 4.8 and data is not perfect for small bubbles ($D < 1$ mm) because many bubbles do not have adequate number of tracer particles within a small search radius $SR = 3D$ to calculate $\langle w_l \rangle$. Unfortunately, this range is crucial to constrain the behavior of $C_L$ for small bubbles, regarding which the community has not reached a consensus. $C_L$ could either be constant (Ziegenhein, Tomiyama, and Lucas, 2018; Hibiki and Ishii, 2007) or drop down to zero (Tomiyama et al., 2002). Equation 4.8 lists two possibilities of $C_L$ for $We < 0.1$: $C_L$ either stays constant at 0.78 (cyan dashed line in figure 4.3(b)) or decreases from 0.78 to 0 linearly as $D$ decreases from 0.8 mm to zero: $2.671We^{3/5}$ (solid line). Both of these lines are also shown in figure 4.3(a).

Once $C_L$ is known, the last unknown $C_D$ can be determined from equation 4.3. Figure 4.5 shows the calculated $C_D$ (blue circles) as a function of the bubble-scale Reynolds number, defined as $Re_b = (\langle w_l \rangle - \langle w_b \rangle)D/\nu$. For comparison, $C_D$ from other experiments (Tomiyama et al., 1998; Ishii and Zuber, 1979; Ishii and Chawla, 1979; Loth, 2008), including both clean and contaminated water, are also compiled in the same figure.

For small bubbles ($Re_b < 400$), our results agree with Tomiyama's data (Tomiyama et al., 1998) on bubbles rising in contaminated water (magenta triangles) very well. As $Re_b$ exceeds 400, $C_D$ in intense turbulence becomes systematically lower. Since it occurs in the range of $Re_b$ where pressure drag

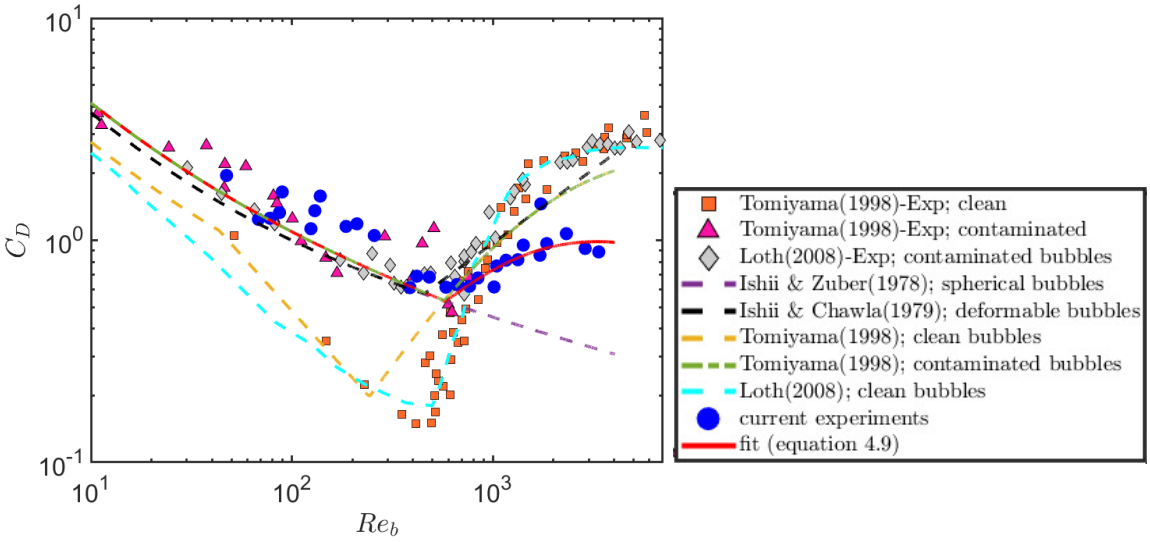


**Figure 4.5:** The drag coefficient for bubbles versus the bubble-size-based Reynolds number $Re_b$. Data obtained from our experiments are shown as blue circles. The proposed corrected drag model is shown as the red solid line (equation 4.9). Previous works on bubbles rising in clean and contaminated quiescent water as well as different models are shown as symbols and lines, respectively.

induced by bubble wake also significantly increases $C_D$, it may imply that turbulence modulates the bubble wake dynamics. The eddy turnover time ($\tau = \sqrt{4/3}(\epsilon^{-1/3}r^{2/3})$=36.7 ms for $D = 4$ mm) is much shorter than the wake shedding period based on the Strouhal number calculation ($\tau_w = 100$ ms for $D = 4$ mm) (Lindt, 1972; Brücker, 1999). This suggests that it is challenging for a bubble to develop an established wake as the incoming flow direction keeps varying. It may explain smaller $C_D$ observed in intense turbulence compared to what has been found in a quiescent medium.

Here, we propose a corrected $C_D$ curve based on the turbulence-based Weber

number. This revised drag coefficient model is:

$$C_D = \max\left(24/Re_b(1+0.15Re_b^{0.687}), \min\left(f(Eo), f(Eo)/We^{1/3}\right)\right) \tag{4.9}$$

where $f(Eo) = 8Eo/3(Eo+4)$. Although the formulation seems long, it is essentially a combination of three equations for three regimes: (i) solid sphere model $C_D = 24/Re_b(1+0.15Re_b^{0.687})$ (Clift and Gauvin, 1971) for small bubbles with slightly-contaminated interfaces, (ii) the phase velocity model $C_D = f(Eo) = 8Eo/3(Eo+4)$ for large bubbles (Tomiyama et al., 1998), (iii) Our corrected model based on the Weber number $We$. For $We < 1$, $C_D$ recovers the original formulation of $8Eo/3(Eo+4)$. For $We > 1$, drag for large $Re_b$ is corrected to account for the modified wake effect. As shown in figure 4.5, this revised curve fits well to the measured results of $C_D$ .

Based on equation 4.8 for $C_L$ and equation 4.9 for $C_D$, we can finally explain the surprising behavior of $\langle w_b \rangle$ shown in figure 4.2. First of all, the overall trend of this curve is determined primarily by the direction inversion of the lateral lift. Intense turbulence with a large $\epsilon$ brings in two effects: (i) strong local velocity gradient, which effectively increases the contribution of lift and pressure gradient, and (ii) enhanced eddy velocity. The first effect can drastically change the mean bubble rise velocity as bubbles being swept to different sides of eddies, and the second effect amplifies the magnitude change of $\langle w_b \rangle$.

The behavior of $\langle w_b \rangle$ for small bubbles ($D < 1$ mm) is shown in the zoomed-in figure 4.2 inset. Two lines correspond to two different $C_L$ curves provided in equation 4.8. The solid line ($C_L = 2.671We^{3/5}$ ($We < 0.1$)) seems to agree with $\langle w_b \rangle$ better.

Although our experiments were collected at a fixed $\epsilon$, we found three prior works (Poorte and Biesheuvel, 2002; Prakash et al., 2012; Aliseda and Lasheras, 2011) conducted at different $\epsilon$ (ranges from $1.3 \times 10^{-4}$ to $6 \times 10^{-3}$ m$^2$/s$^3$) that can also be used to test the model. As $\epsilon < 0.1$ m$^2$/s$^3$, $We$ is much smaller than $Eo$ for bubbles of size $D = 0.5$–3 mm. Therefore, for these cases, bubble deformation is primarily driven by buoyancy, and the turbulence effect is secondary. Moreover, in weak turbulence, $We$ is not large enough to produce an early lift inversion. As a result, both $C_L$ and $C_D$ will recover that in a quiescent medium (red dotted line in figure 4.3(b) for $C_L$, and dashed green line in figure 4.5 for $C_D$). Taking both effects into consideration, the model prediction of $\langle w_b \rangle$ is shown in figure 4.2 as the purple shaded area (area covers the range of $\epsilon$ used in three works), which passes through all the reported values. This area is indeed systematically lower than that in a quiescent medium by 20–40%. This percentage change seems to be quite similar among these works despite a large range of $\epsilon$ used, which could be attributed to the saturation of $\langle w_l \rangle$. Since lift scales with $\gamma$ and the pressure force scales with $\gamma^2$, for small $\epsilon$, lift is always dominant, pushing bubbles to the edge of an eddy and saturating $\langle w_l \rangle$ at the

maximum eddy velocity, $\sim \gamma D/2$.

---

## SUMMARY

In summary, a new vertical water tunnel with a large energy dissipation rate was developed to study bubble dynamics in intense turbulence, in which turbulence-induced bubble deformation, measured by $We$, becomes close to or larger than the buoyancy-induced deformation, quantified by $Eo$. Unlike other previous works conducted in weak turbulence ($Eo \gg We$), a surprising new behavior of bubble rise velocity has been observed: within a small range of bubble sizes, bubble rise velocity transitions from an order of magnitude smaller to a factor of two larger than that in an otherwise quiescent medium.

Simultaneous measurements of dense tracer particles around bubbles show that flows around small bubbles move preferentially downward, hindering the rising motion of bubbles. Opposite upward flows are observed surrounding large bubbles, effectively increasing their rise velocity. This confirms the proposed preferential sampling mechanism that bubbles with different sizes tend to be swept to different regions in turbulence, rather than being trapped in the center of eddies.

A model was derived by taking the ensemble average of both sides of the

governing equation for bubble motion in turbulence. Since unsteady forces get averaged out in the process, only four forces, lift, buoyancy, drag, and pressure gradient, are left in the equation. Two pairs of forces, buoyancy versus drag and lift versus pressure gradient, can be balanced along two orthogonal directions, which helps to utilize the measurable quantities, i.e. mean bubble and flow vertical velocity to estimate the drag and lift coefficients.

The lift coefficient shows clear direction inversion, similar to what has been extracted from experiments studying bubbles migrating in laminar shear flows. But in intense turbulence, $WeEo$, the transition occurs at a smaller bubble size when turbulence $We$ switches from below to above one. The drag coefficient is also modified for large bubbles. Strong turbulence potentially affects the formation of bubble wakes, which leads to a smaller drag coefficient. This effect also contributes to the enhanced rise velocity of bubbles. Finally, the model has also been tested on other datasets from previous works conducted at lower $\epsilon$; excellent agreement between the model predictions and the experimental results is observed without using any fitting parameters.

# Chapter 5

# Experimental investigation of the added mass force of deformable bubbles in intense turbulence

*We present an experimental investigation of the added mass force and coefficient ($C_A$) of deformable gas bubbles in turbulence. Such a measurement is made possible through a system that can track both phases simultaneously in 3D. The measured results provide two independent ways of estimating the bubble acceleration: either directly determined from bubble trajectories or calculated from the surrounding tracers by using the added mass coefficient. The acceleration standard deviation determined from these two methods have to agree with each other, and such a constraint helps us to determine the added mass coefficient. We found that the acceleration standard deviation seems to increase*

*as bubble deformation becomes stronger, which suggests a reduced bubble apparent inertia and a decrease in $C_A$. To understand the dependence of $C_A$ with the bubble aspect ratio, the probability density function of the relative orientation between the semi-major axis of deformed bubbles and the slip acceleration in turbulence is shown. We clearly see that the bubble orientation is not random in turbulence; rather, they are preferentially aligned with the slip acceleration. The degree of this alignment increases as bubbles deform more. Finally, Lamb's analytical solutions for solid spheroids are employed to understand the trend of $C_A$. By using the measured bubble geometry and orientation, the predicted trend of $C_A$ shows a good agreement with the measured results, suggesting that the added mass force acting upon deformable bubbles in intense turbulence follows similar rules as those for solid spheroids with the same geometry and orientation statistically*

---

## INTRODUCTION

Two-phase flows with deformable gas bubbles dispersed in a turbulent medium are a common occurrence in natural flows, e.g. air bubbles entrained in breaking waves (Deane and Stokes, 2002) and industrial devices, e.g. chemical and nuclear reactors (Michiyoshi and Serizawa, 1986; Jakobsen, 2008). Given the

strong temporal and spatial flow fluctuations in intense turbulence, the dispersed phase is subject to intermittent flow accelerations, and thus experiences an additional inertial force in order to accelerate or decelerate an apparent mass of the surrounding fluid (Ishii and Hibiki, 2010). This unsteady force is often referred to as the added mass force, $F_A$ (Lamb, 1924; Batchelor and Batchelor, 1967; Brennen, 1982). In $F_A$, other than the bubble volume and the acceleration difference between the two phases (i.e. slip acceleration), a free parameter was introduced, which is often referred to as the added mass coefficient ($C_A$).

For an object accelerating even in a simplified otherwise quiescent medium, $C_A$ was found to be sensitive to (i) the object shape (Lamb, 1924; Brennen, 1982; Newman, 1977; Kendoush, 2007); (ii) the object's orientation with respect to the slip acceleration (Lamb, 1924; Brennen, 1982); (iii) the local object concentration, including the number of objects, the distance among themselves, and their configurations (Zuber, 1964; Sankaranarayanan et al., 2002; Kendoush, Sulaymon, and Mohammed, 2007; Pudasaini, 2019); and (iv) the boundary effects, including the object-boundary distance and boundary geometries (Ackermann and Arbhabhirama, 1964; Simcik, Ruzicka, and Drahoš, 2008). Furthermore, additional complications arise if any one of these parameters changes over time (Magnaudet and Eames, 2000; Ohl, Tijink, and Prosperetti, 2003).

Although $C_A$ has a complex relationship with many parameters, it does not

rely on the object size, as long as its volume does not change over time. $C_A$ is also independent of the object-size-based Reynolds number (Wakaba and Balachandar, 2007) and the material properties of either the object itself or its surrounding fluid (Magnaudet, Rivero, and Fabre, 1995). Note that, although $C_A$ does not depend on the material properties, the relative role of the added mass force, compared with other hydrodynamic forces, is sensitive to the density ratio between the two phases. For example, for heavy particles accelerating in the air, since the apparent mass of the surrounding gas ($m_A$) accelerated by the particles is much lighter than the mass of the heavy particles themselves ($m_p$), the added mass force can be neglected. In the other extreme of air bubbles accelerating in water, the added inertia far exceeds the inertia of the bubble itself ($m_A \gg m_p$), thus underscoring the importance of the added mass force. It is important to note that, for both extremes, as long as the shape of the object is the same, $C_A$ is identical (Mougin and Magnaudet, 2002; Mougin and Magnaudet, 2006). Whether the added mass force is important or not depends solely on the density ratio between the two phases.

Given the importance of the added mass force to bubble dynamics in water, attempts were made previously to investigate the effect of the bubble shape, orientation and void fraction on $C_A$, but limited to simple flow configurations. De Vries, Luther, and Lohse (2002) experimentally investigated an induced oscillation of a bubble after being tripped by a wire as it rises in water. The im-

portance of the added mass force was highlighted by showing that, without it, the observed bubble oscillation could not be reproduced. In addition, Sankaranarayanan et al. (2002) determined the added mass coefficient of a mixture of gas bubbles using the Lattice Boltzmann method. In this simulation, $C_A$ for bubbles is shown to be sensitive to both the bubble deformation and the void fraction. Other than these two cases, (Ohl, Tijink, and Prosperetti, 2003) performed experiments on an expanding bubble due to the sudden drop of the ambient pressure. The time-varying bubble volume is shown to affect the added mass force, although this effect is probably negligible in our case where the bubble volume does not significantly change over time.

Furthermore, the added mass force was shown to be important for the path instabilities of rising spheroidal bubbles in an otherwise quiescent medium (Mathai, Lohse, and Sun, 2020; Mougin and Magnaudet, 2006; Cano-Lozano et al., 2016). Lavrenteva, Prakash, and Nir (2016) studied the interaction of air bubbles in low-Reynolds-number Taylor-Couette flow and demonstrated that the added mass force played a key role in explaining the separation of neighboring bubbles observed experimentally (Prakash et al., 2013). Although these works clearly articulated the importance of the added mass force in a quiescent medium or low-Reynolds-number shear flows, it remains elusive how to prescribe a correct $C_A$ for a deformable bubble subject to strong turbulent accelerations where deformation and bubble orientations are also coupled with

the surrounding flows.

The main objective of this manuscript is to experimentally investigate how to characterize $C_A$ for deformable bubbles in turbulent bubbly flows. In §5, we compile the current knowledge and analytical results of the value of $C_A$ for a range of rigid geometries. In §5, we briefly provide a discussion of all the quantities needed to estimate $C_A$ experimentally. The procedure to determine $C_A$, the results, and how they depend on the bubble relative orientation in turbulence will be introduced in §5.0.1. §5.0.3 summarizes the work in this chapter and presents remarks for future research.

---

## ANALYTICAL SOLUTIONS OF THE ADDED MASS COEFFICIENT

Let us consider an object moving in an otherwise quiescent fluid at a constant slip velocity ($\mathbf{u}_s$). In such a steady scenario (the slip acceleration $\mathbf{a}_s = D\mathbf{u}_s/Dt$ is zero), the force that the object experiences is the steady drag force. However, when the object starts to accelerate ($\mathbf{a}_s \neq 0$), in addition to the drag force, the force acting on the object has to accelerate both the object and its surrounding fluid. This extra layer of accelerating fluid essentially adds to the object inertia (Newman, 1977), which is commonly referred to as the added mass force. Alternatively, the added mass can be viewed as

a way to measure the necessary work done by the object with volume $V_b$ to change the kinetic energy ($K$) of the surrounding fluid with density $\rho_l$ (Brennen, 2005). If $K = 1/2 C_A \rho_l V_b u_s^2$ is the kinetic energy injected by the object into the surrounding fluid, the added mass force can be estimated based on: $\mathbf{F}_A = (DK/Dt)/\mathbf{u}_s = C_A \rho_l V_b D\mathbf{u}_s/Dt = m_A D\mathbf{u}_s/Dt$. Here $m_A$ is the added mass, and $\mathbf{F}_A$ and $C_A$ are the force and coefficient associated with $m_A$, respectively.

The added mass coefficient, $C_A$, is not a single value but rather a $6 \times 6$ tensor, which includes the acceleration of translational and rotational components in all three directions (Lamb, 1924; Sadeghi and Incecik, 2005). In general, the off-diagonal elements of this tensor are non-zero, implying that the translational and rotational accelerations can be fully coupled. This property results in 36 unknowns that need to be determined at each time step for the instantaneous flow configuration and object orientation, which is impractical for experimental measurements. The number of unknowns can be reduced for simplified cases. For example, it has been found that the potential flow assumption renders the added mass tensor to be symmetric, thereby reducing the number of coefficients to 21 (Brennen, 1982; Brennen, 2005).

Another possible simplification can be made through geometric symmetries, such as spheres (Magnaudet, Rivero, and Fabre, 1995), cylinders (Sarpkaya, 1963, 1975), or spheroids (Lamb, 1924; Newman, 1977). The most simplified form of $C_A$ is available for a single spherical particle (with three axes of

symmetry), where the matrix becomes purely diagonal with no secondary induced accelerations. Lamb (1924) (article 92) analytically solved the added mass coefficient of a sphere accelerating through fluid following a rectilinear path and found that $C_A = 0.5$ in the direction of motion. This finding was followed by a series of experiments (Sridhar and Katz, 1995; Kendoush, Sulaymon, and Mohammed, 2007; Friedman and Katz, 2002) and numerical simulations (Sankaranarayanan et al., 2002; Magnaudet, 1997; Maliska and Paladino, 2006), and the value of $C_A = 0.5$ was consistently reported or used in different flow conditions.

A spheroid (oblate or prolate) or a cylinder is the simplest geometry to consider after a sphere. Potential flow solution for a cylinder accelerating perpendicular to its long axis showed that the added mass is equal to the mass of the fluid displaced by the cylinder (Brennen, 1982) i.e., $C_A = 1$. Furthermore, extensive work has also been conducted to analyze the dependence of $C_A$ for a cylinder under oscillating flows to understand the effect of vortex shedding on $C_A$ (Sarpkaya, 1975). In addition to a cylinder, Lamb (1924) analytically solved $C_A$ for both a prolate spheroid and an oblate spheroid in the articles 114 and 373 of his book, respectively. $C_A$ was found to be a function of the object aspect ratio and whether the spheroid particle is accelerating along its long axis (*end-on*) or its short axis (*broadside-on*). Figure 5.1 illustrates a prolate spheroid and an oblate spheroid moving *end-on* or *broadside-on*. The analytical solu-

tions for these four cases: prolate *end-on* (pe), prolate *broadside-on* (pb), oblate *end-on* (oe), and oblate *broadside-on* (ob) are given as:

$$C_A^{pe} = \alpha_1/(2-\alpha_1);\ C_A^{pb} = \beta_1/(2-\beta_1);\ C_A^{oe} = \alpha_2/(2-\alpha_2);\ C_A^{ob} = \beta_2/(2-\beta_2) \quad (5.1)$$

where, $\alpha_1 = (1-e^2)/e^3(\ln((1+e)/(1-e)) - 2e)$, $\beta_1 = (1-e^2)/e^3(e/(1-e^2) - 1/2\ln((1+e)/(1-e)))$, $\alpha_2 = 2/e^3(e - \sqrt{1-e^2}\sin^{-1}e)$, $\beta_2 = 1/e^3(\sqrt{1-e^2}\sin^{-1}e - e(1-e^2))$. Parameter $e = \sqrt{1-1/\chi^2}$ is the eccentricity of an object along its meridian, and $\chi = r_1/r_3$ is the object aspect ratio. Moreover, Kendoush (2007) provided a semi-analytical solution for oblate spheroidal bubbles rising in liquid and found that the Lamb's solution for oblate spheroids moving *broadside-on* overestimates the value of $C_A$ at higher aspect ratios.

Although the analytical solutions of $C_A$ seem to work well for rigid particles of different shapes (spheres, cylinders or spheroids) accelerating in different flow conditions, little is known how to correctly model $C_A$ for deformable objects whose shape keeps evolving, which is particularly challenging in a turbulent environment as deformation is coupled with a rather complicated surrounding flow. In this chapter, we intend to use simultaneous measurements of both the phases to test if we can provide any experimental constraints to the added mass coefficient of deforming bubbles in intense turbulence.

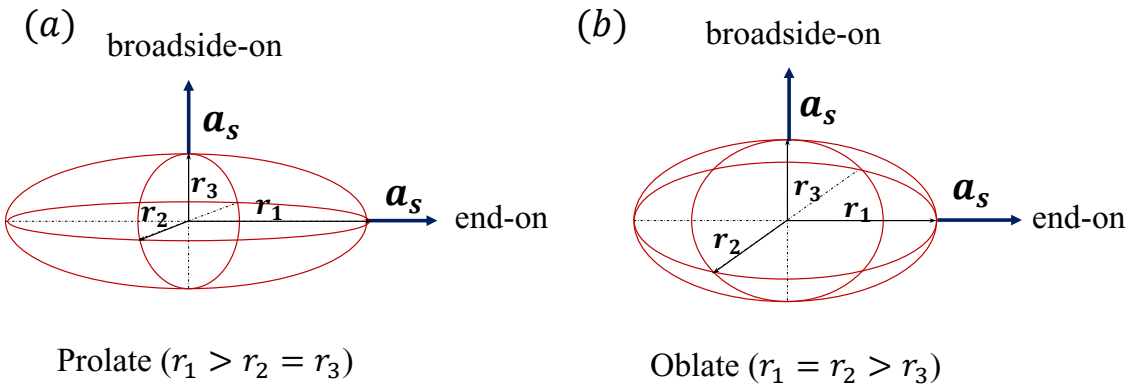


**Figure 5.1:** Schematics of four configurations of accelerating spheroids with known analytical solutions of $C_A$, including (a) a prolate spheroid, and (b) an oblate spheroid, accelerating along their semi-minor axis (*broadside-on*) or semi-major axis (*end-on*).

## EXPERIMENTAL METHODS

Similar to the other works in chapters 3 and 4, the experiments in this work were also conducted in the V-ONSET setup. From our flow measurements, we have 6942 reliable 3D bubble trajectories and about 30–40 tracer particles surrounding each bubble that will be used to extract the statistics of $C_A$.

### 5.0.1 Summary of measurable quantities

In this section, we summarize the physical quantities that can be measured through our experiments. Figure 5.2 shows an example trajectory of a bubble that is about 400 frames in length. Here, the 3D-reconstructed bubble geometries are plotted once every one hundred frames along the trajectory. From the geometry, bubble size ($D$), aspect ratio ($\chi = r_1/r_3$), and the orientation of both semi-major ($\hat{\mathbf{r}}_1$) and semi-minor ($\hat{\mathbf{r}}_3$) axes can be acquired. Moreover, the 3D locations of surface points on the reconstructed geometry can be averaged to obtain the center of mass of the bubble, which was tracked over time to construct the bubble trajectory.

Bubble tracks are then convoluted with a Gaussian kernel to obtain the bubble velocity ($\mathbf{u}_b$) and acceleration ($\mathbf{a}_b$) along their trajectories (Mordant, Crawford, and Bodenschatz, 2004). The Gaussian kernel acts effectively as a high-

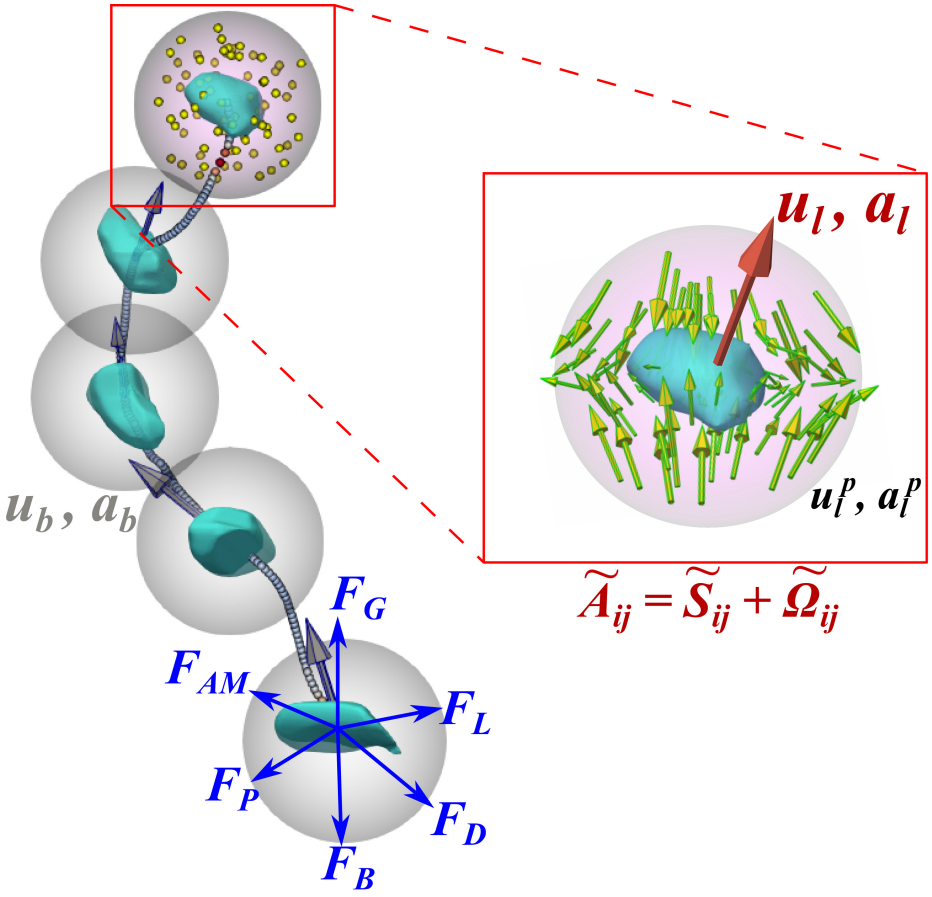


**Figure 5.2:** Reconstructed three-dimensional trajectory of a bubble ($D = 5.1$ mm) over 0.1 s (400 frames). The 3D reconstructed bubble geometries are only shown one every hundred frames as green blobs. The grey arrows protruding from the center of these 3D geometries represent the instantaneous bubble velocities. A grey sphere around each bubble represents a search volume that is used to seek tracer particles, whose locations for one time instant is marked as yellow dots. Their velocity $u_l^p$ vectors are indicated in the zoomed-in picture. The blue arrows on one bubble represents all the relevant forces that the bubble experiences.

pass filter that reduces the position uncertainties to allow for an accurate estimation of velocity and acceleration. It is well known that the acceleration variance is sensitive to noise and the selected filter length. To justify the filter length used, we follow the procedure introduced by (Voth et al., 2002). In figure 5.3(a), the standard deviation of the bubble acceleration $\sqrt{\langle a_b^2 \rangle}$ in the horizontal ($x$) direction is shown as a function of the temporal filter width ($\tau$) normalized by the Kolmogorov time scale, $\tau_\eta = 1.4$ ms. The initial sharp decay of $\sqrt{\langle a_b^2 \rangle}$ is due to the noise removal and the later gradual change is due to the actual signal being smoothed out. The results are consistent with other previous findings (Voth et al., 2002; Ni, Huang, and Xia, 2012). It was suggested that one can obtain a correct filter length by fitting the data with a superposition of a power law and an exponential function to respectively account for the fast and slow decays. The fit is shown as the solid line, and the contribution of only the exponential term is shown as the dashed line. The vertical intercept of the dashed line at $\tau/\tau_\eta = 0$ provides the best estimate of the acceleration variance. Based on the estimated value, the filter length of $\tau/\tau_\eta = 0.58$ was used consistently to smooth the bubble trajectories.

The same procedure can be repeated to calculate the tracer velocity ($\mathbf{u}_l^p$) and acceleration ($\mathbf{a}_l^p$), in which the superscript $p$ represents individual tracer particles to distinguish from the locally-averaged fluid properties that will be introduced later. In figure 5.3(a), the same filter-length test has also been per-

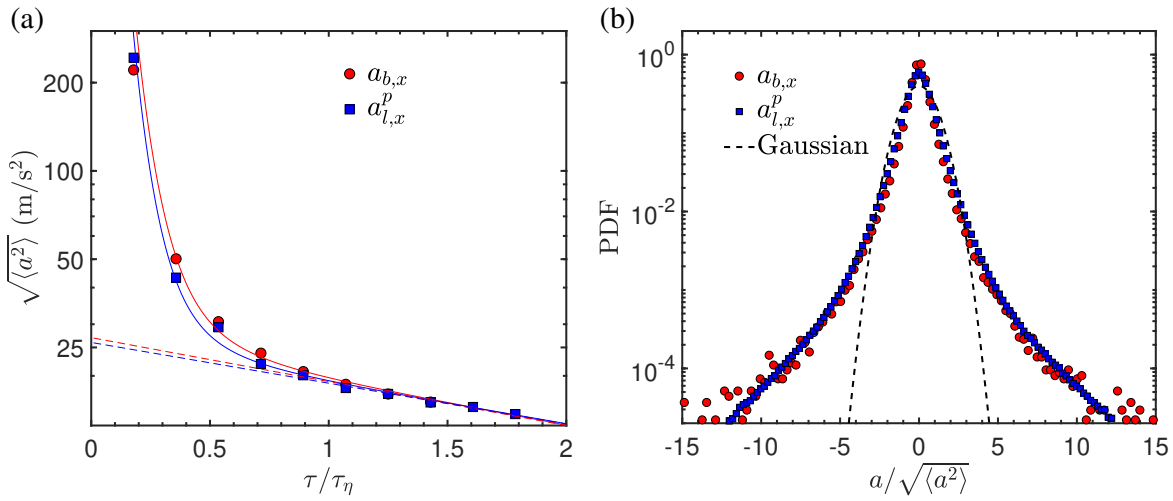


**Figure 5.3:** (a) The standard deviation of one horizontal component of the bubble and flow acceleration versus the filter length. For the solid lines and the dashed lines, please see text; (b) Probability density functions of the normalized bubble and tracer accelerations in the horizontal direction using a fixed filter width of $\tau = 0.58\tau_\eta$. The dashed curve represents a Gaussian function with the same variance as the corresponding data.

formed for tracer particles, and the results are very close to those of bubbles. Therefore, the same filter length was adopted for both the phases. Finally, the probability density functions (PDF) for $\mathrm{a}_b$ and $\mathrm{a}_l^p$ in two different directions are shown, both of which exhibit a stretched exponential shape that is consistent with previous works (Voth et al., 2002; Ni, Huang, and Xia, 2012).

As illustrated in figure 5.2, at each time instant along a bubble trajectory, a search volume (gray semi-transparent sphere) of radius $D_s/2$ ($D_s = 4D$, where $D$ is the equivalent bubble diameter) is used to seek tracer particles with velocity $\mathrm{u}_l^p$ in the vicinity of a bubble at location $\mathrm{x}_0$. By applying the Taylor expansion, the flow field within this range can be decomposed into leading terms:

$\mathbf{u}_l(\mathbf{x}_0)$ and $\widetilde{A}_{ij}x_j^p$, where $\mathbf{u}_l = \sum_{p=1}^{n} \mathbf{u}_l^p(\mathbf{x}_0 + \mathbf{x}^p)/N$ is the local mean flow averaged over $N$ selected tracer particles. The same procedure can be repeated to calculate the average flow acceleration $\mathbf{a}_l = \sum_{p=1}^{n} \mathbf{a}_l^p(\mathbf{x}_0 + \mathbf{x}^p)/N$. $\widetilde{A}_{ij}$ indicates the velocity gradient tensor around the bubble, and the tilde indicates that this gradient is coarse-grained at the bubble size. The symmetric component of $\widetilde{A}_{ij}$ is the coarse-grained strain rate tensor, $\widetilde{S}_{ij}$. In addition, $\mathbf{x}^p$ is the separation vector directed from the bubble center at $\mathbf{x}_0$ to the $p^{th}$ tracer particle. $\widetilde{A}_{ij}$ can be uniquely solved if we have four particles around a bubble. In practice, on average, 30–40 particles were used to perform least-squares fits by seeking the minimum value of the squared residuals $\sum_p [u_i^p - \widetilde{A}_{ij}x_j^p]^2$ (Ni et al., 2015a; Pumir, Bodenschatz, and Xu, 2013). Several stringent criteria have been enforced to ensure that only the results with reliable $\widetilde{A}_{ij}$ will be included in the statistics (Masuk, Salibindla, and R, 2020). Due to the limited particle concentration, applying a search diameter of $D_s$ tends to underestimate $\widetilde{A}_{ij}$ around a bubble with size of $D$ because of the larger-filter effect ($D_s > D$). Fortunately, since both $D_s$ and $D$ are in the inertial range, by assuming a constant local energy dissipation rate, $\widetilde{A}_{ij}$ can be corrected with a factor of $(D_s/D)^{2/3}$ to account for the scale difference. Additional details using different $D_s$ to confirm this correction has been reported by Masuk, Salibindla, and R (ibid.).

### 5.0.2 Governing equation

The governing force balance equation for a finite-sized bubble moving is again taken from 1.9:

$$V_b\rho_b\frac{D\mathbf{u}_b}{Dt} = \rho_l V_b C_A(\frac{D\mathbf{u}_l}{Dt} - \frac{D\mathbf{u}_b}{Dt}) + V_b(\rho_l - \rho_b)g\hat{\mathbf{e}}_z + \frac{\rho_l}{2}A_b C_D(\mathbf{u}_l - \mathbf{u}_b)|\mathbf{u}_l - \mathbf{u}_b| + \rho_l C_L(\mathbf{u}_l - \mathbf{u}_b) \times (\nabla \times \mathbf{u}_l) - \frac{1}{2}V_b\nabla P_w + \mathbf{F}_B \tag{5.2}$$

where six terms on the right side of the equation represent the added mass ($F_{AM}$), buoyancy ($F_G$), drag ($F_D$), lift ($F_L$), pressure ($F_P$), and the Basset history force ($F_B$), in that order. $\nabla P_w$ is the pressure gradient of flow around the bubble, and $\mathbf{u}_l$ is the velocity of the unperturbed ambient flow taken at the centre of the bubble if the bubble was not there. The equation also contains other constants, including the gravitational constant $g$ and the density of water and gas, i.e. $\rho_l$ and $\rho_b$. $V_b$ is the bubble volume and $A_b$ is the projected area of a sphere with an equivalent volume of the bubble. In addition, $C_D$, $C_L$, and $C_A$ are the drag, lift, and the added mass coefficient, respectively. In a previous work by Salibindla et al. (2020), as shown in chapter 4, $C_D$ and $C_L$ for bubbles in intense turbulent environments have already been determined based on the mean bubble and

flow velocity, and they are included here again for completeness:

$$C_D = \max\left(24/Re_b(1+0.15Re_b^{0.687}), \min\left(f(Eo), f(Eo)/We^{1/3}\right)\right) \tag{5.3}$$

$$C_L = \begin{cases} 2.671We^{3/5} & We < 0.1, \\ 1.25 - 1.608We^{3/5} & 0.1 < We < 0.9 \\ -0.23 & 0.9 < We \end{cases} \tag{5.4}$$

where $f(Eo) = 8Eo/3(Eo+4)$ is a function of the Eötvös number, $Eo = (\rho_l - \rho_b)gD^2/\sigma$. The bubble Reynolds number and Weber number are defined as: $Re_b = |u_b - u_l|D/\nu_l$ and $We = 2.13\rho(\epsilon D)^{2/3}D/\sigma$, respectively (2.13 is the Kolmogorov constant for the second-order longitudinal structure function). $We$ determines the turbulence-induced deformation.

Finally, rearranging equation 5.2 yields:

$$\frac{D\mathbf{u}_b}{Dt} = \frac{\rho_l V_b C_A \frac{D\mathbf{u}_l}{Dt} + V_b(\rho_l - \rho_b)g\hat{\mathbf{e}}_z + \frac{\rho_l}{2}A_b C_D(\mathbf{u}_l - \mathbf{u}_b)|\mathbf{u}_l - \mathbf{u}_b|}{V_b(\rho_b + C_A\rho_l)} + \frac{\rho_l C_L(\mathbf{u}_l - \mathbf{u}_b)\times(\nabla\times\mathbf{u}_l) - \frac{1}{2}V_b\nabla P_w}{V_b(\rho_b + C_A\rho_l)} \tag{5.5}$$

Here, compared with the added mass force, the Basset history force is assumed to be small and neglected, and such an assumption will be examined in §5.0.3. Most quantities on the right-hand side of equation 5.5 can be directly de-

termined for any given bubble trajectories (an example is shown in figure 5.2), including the instantaneous velocities ($\mathbf{u}_b$, $\mathbf{u}_l$) and accelerations ($\mathbf{a}_b = D\mathbf{u}_b/Dt$, $\mathbf{a}_l = D\mathbf{u}_l/Dt$) of both bubbles and surrounding flows. Velocity gradients ($\nabla \times \mathbf{u}_l$) can also be estimated based on the discussions in §5.0.1. For each time instant along a bubble trajectory, the bubble size ($D$) was determined from the 3D shape reconstruction, which was used in equation 5.3 and 5.4 to calculate the drag and lift coefficients, respectively. For this particular bubble shown in figure 5.2, tracers within 2D away from the center of the bubble were selected to calculate $\mathbf{u}_l$, $\mathbf{a}_l$ and $\nabla \times \mathbf{u}_l$. If $C_A$ is known, the entire right side of equation 5.5 can be calculated for each bubble trajectory.

Figure 5.4 shows two example time traces of the vertical bubble acceleration, one for a weakly-deformed bubble and the other one for a strongly-deformed case, in conjunction with the time trace of their respective aspect ratios. For both cases, the bubble acceleration directly measured from the bubble trajectory is shown as black circles, and the red dashed lines indicate the calculations based on the right side of equation 5.5 by using $C_A = 0.5$. For the weakly-deformed case (figure 5.4(a)), it is evident that the time trace of the calculated $a_b$ is close to that of the measured results. This agreement suggests that, although the measurement uncertainties of the second-order quantities, e.g. velocity gradients and acceleration, are relatively large, this framework seems to work well and provides a reasonable prediction of $a_b$. It also implies

that, at least for many bubbles that are close to the spherical shape, the assumption of using the added mass coefficient close to 0.5 seems to be reasonable. Note that it is difficult to extract $C_A$ at each time instant because the local acceleration could be affected by the fact that $C_A$ is a tensor instead of a constant—one component of translational acceleration could be affected by other components and surrounding rotational flows. Furthermore, compared with the weakly-deformed case, applying $C_A = 0.5$ seems to systematically under-predict the acceleration fluctuation of the strongly-deformed bubble, as shown in figure 5.4(b). This observation indicates that the acceleration fluctuation and the added mass coefficient may be coupled, and both of them may change as a function of the bubble deformation. Note that, strictly speaking, equation 5.5 should only be applied to microbubbles with their sizes below the Kolmogorov scale immersed in a surrounding linear flow. Here, we assume that this equation also works for finite-sized bubbles with their surrounding flows coarse-grained at the bubble size.

Before discussing the dependence of $C_A$ on the geometry of finite-sized deformable bubbles, we would like to identify a statistical quantity that can be used to constrain $C_A$. Given the fact that $C_A$ may play a role in determining the acceleration fluctuation, the PDFs of one component of the calculated accelerations using two different $C_A$ are shown in Figure 5.6(a). For comparison, the PDF of the measured bubble acceleration is also plotted. First of

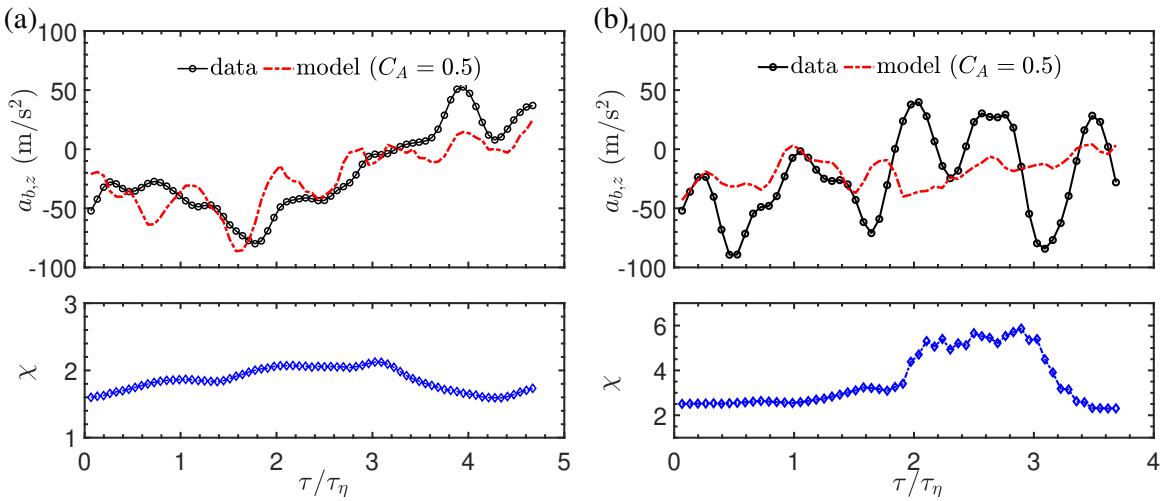


**Figure 5.4:** The time series of the vertical acceleration of (a) a weakly-deformed bubble and (b) a strongly-deformed bubble. In conjunction with the measured results, the calculated result of the acceleration from equation 5.5 using $C_A = 0.5$ and the measured time series of the aspect ratio are also shown.

all, for both $C_A$, the calculated acceleration PDFs show similar stretched exponential shape, which is consistent not only with our observation but also with many other previous fluid acceleration measurements in turbulence (La Porta et al., 2001; Voth et al., 2002; Ni, Huang, and Xia, 2012). Applying $C_A = 0.5$ appears to produce a PDF that shows an excellent agreement with the measured results. Since $C_A = 0.5$ was derived for rigid spherical particles, this agreement suggests that a large portion of our bubbles are not significantly deformed, which is consistent with the fact that 81% of bubbles have an aspect ratio smaller than $\chi = 2$. Despite the overall good agreement, some small deviation at the tails for large acceleration is observed, which indicates that $C_A = 0.5$ may not work as well for bubbles experiencing strong acceleration.

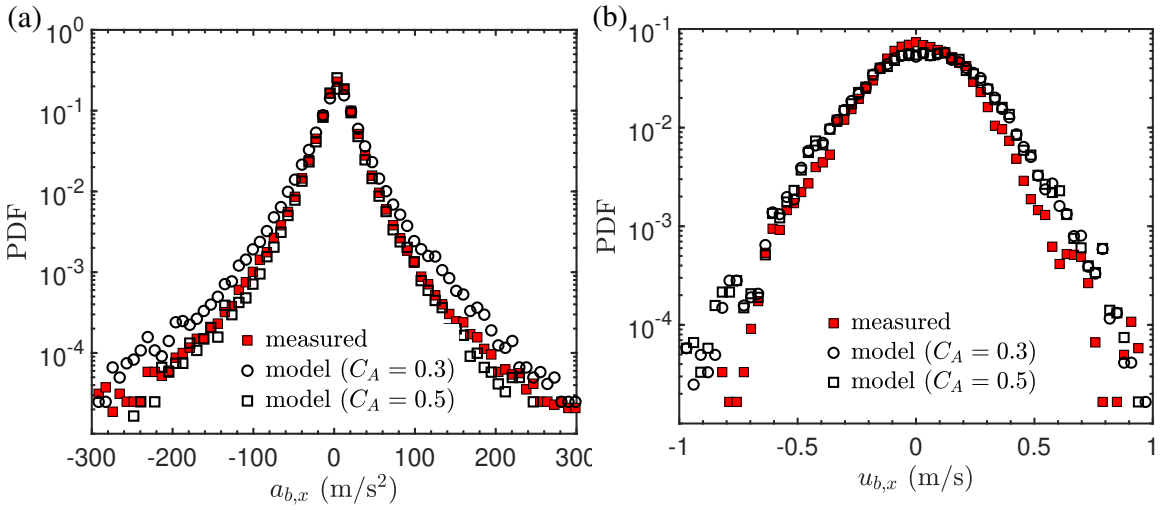


**Figure 5.5:** Probability density function of (a) the horizontal bubble acceleration and (b) the horizontal bubble velocity, obtained from the measured data (red square) and from equation 5.5 with two different $C_A$ of 0.3 (open circle) and 0.5 (open square).

This observation will be further discussed later in this section. Moreover, as one may clearly see, the calculated PDF by employing $C_A = 0.3$ seems to spread wider about the central value, systematically over-predicting the fluctuation of the bubble acceleration. This is expected as a smaller $C_A$ suggests a reduced effective bubble inertia; under the same hydrodynamic forces, bubbles tend to experience larger accelerations.

In addition to the bubble acceleration, the same calculation has been repeated for the PDF of the bubble velocity to examine its sensitivity to $C_A$. Similar to the acceleration calculation, the bubble velocity can either be determined directly from their trajectories, or by integrating the calculated bubble acceleration through equation 5.5. The PDF of one component of the horizontal bubble

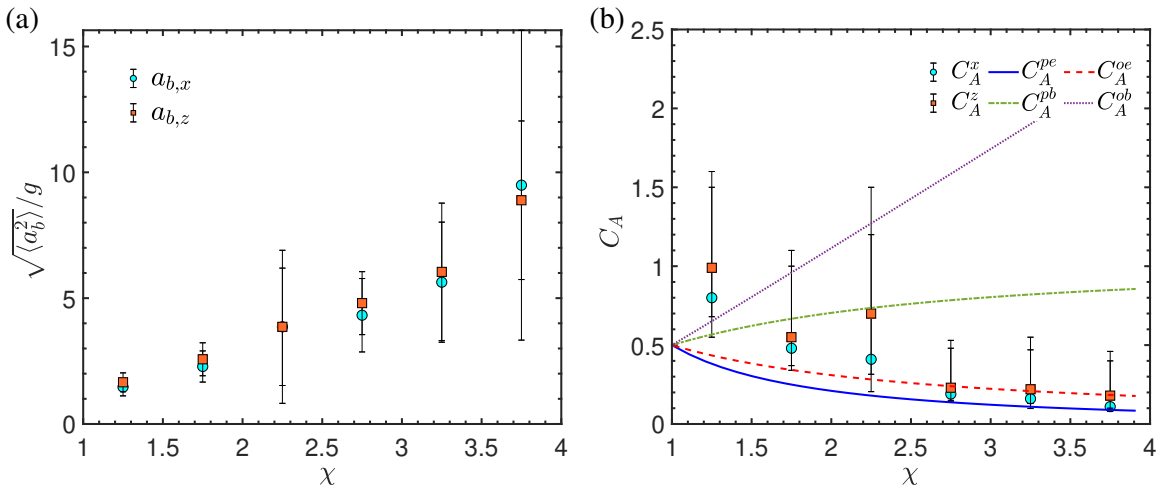


**Figure 5.6:** (a) The standard deviation of the bubble acceleration, normalized by the gravitational constant $g$, versus the bubble aspect ratio $\chi$. Two symbols represent two different directions. (b) The added mass coefficient, $C_A$, versus $\chi$. The symbols are the same as those in (a). Four different lines represent $C_A$ calculated based on Lamb's model for spheroids of different aspect ratios and configurations.

velocity calculated from such an integration using both $C_A = 0.3$ and 0.5 are shown in figure 5.5(b). Both PDFs agree well with each other and with the measured results. Compared with the acceleration PDFs, the velocity PDFs seem to be less sensitive to the value of $C_A$. This is not surprising as many events with strong acceleration fluctuations are probably smoothed out during integration and thus not reflected in the velocity PDF.

Based on the previous tests, we conclude that $C_A$ can be constrained by the spread of the acceleration PDF about the central value. The parameter to measure this spread is the acceleration standard deviation. Moreover, $C_A$ does not depend on the size of an object; it is only a function of its geometry.

Therefore, $\sqrt{\langle a_b^2 \rangle}$ in both horizontal and vertical directions are shown in figure 5.6(a) as a function of the bubble aspect ratio $\chi$. Note that $\chi$ here represents the track-averaged bubble aspect ratio. We also tried to condition $\sqrt{\langle a_b^2 \rangle}$ on the instantaneous bubble aspect ratio, and the results are very similar to what is shown in figure 5.6(a). It seems that $\sqrt{\langle a_b^2 \rangle}$ of both directions increase from about $\sim 2g$ to $\sim 10g$. Such a high value of $\sqrt{\langle a_b^2 \rangle}$ can be attributed to the strong ambient turbulence around bubbles with an average energy dissipation rate of $0.5$ m$^2$/s$^3$ (Masuk et al., 2019). (Prakash et al., 2012) also performed experiments to study the effect of ambient turbulence on bubble acceleration and reported that, for bubbles in weak turbulence ($\epsilon \sim 10^{-4}$ m$^2$/s$^3$), the standard deviation of the vertical acceleration exceeds their horizontal counterpart by $g \approx 10$ m/s$^2$. In our case, no significant difference in acceleration between two directions is observed, probably because the buoyancy effect is overwhelmed by the intense turbulence. The error bars in this figure were calculated by dividing the entire data set into six equal subsets and calculating $\sqrt{\langle a_b^2 \rangle}$ among these subsets, similar to what has been done before by Voth (2000).

To calculate $C_A$ for different $\chi$, an iterative fit was performed. At the beginning of each iteration, $C_A$ will be prescribed either based on the track-averaged $\chi$ or the previous iteration. $\sqrt{\langle a_b^2 \rangle}$ is then calculated from the right-hand side of equation 5.5. The difference of the calculated $\sqrt{\langle a_b^2 \rangle}$ and the ones measured from experiments is used to correct $C_A$. The iteration will continue until the

difference in $\sqrt{\langle a_b^2 \rangle}$ using two methods is too small. For each $\chi$, in addition to the mean value, the uncertainty of $C_A$ is estimated by repeating the same iterative fit to the upper and lower bounds of $\sqrt{\langle a_b^2 \rangle}$ (figure 5.6(a)).

The results of the estimated $C_A$ are shown in figure 5.6(b). First of all, in the limit of spherical and isolated bubbles, $C_A$ should be equal to 0.5 based on the analytical calculation that was discussed in §5. Although $C_A$ seems to have a trend of getting close to 0.5 as $\chi$ reduces to one, it clearly overshoots beyond 0.5 at $\chi = 1.25$. One possible explanation for such a result is that bubbles in our case are not exactly isolated. In our experiments, the bubble volume concentration ($\phi$) is kept close to 2%, striking a balance between acquiring enough statistics within an affordable time period and possible contamination due to bubble-bubble interaction. At this concentration, it has been shown that the bubble-bubble interaction could have non-negligible effect on $C_A$ with the largest reported value close to $C_A = 1$ at $\phi = 2$ % by Pudasaini (2019) and the smallest value close to $C_A = 0.6$ by Sankaranarayanan et al. (2002).

In addition, $C_A$ seems to gradually decrease as $\chi$ increases. To understand this trend, we seek solutions from Lamb's potential flow models. But in order to use these models, one would need to know if the shape of deformed bubbles in turbulence follows either prolate or oblate spheroids and along which direction they are accelerating. However, prolate and oblate spheroids are ideal approximations at extremes; a typical deformed bubble is somewhere in between. If

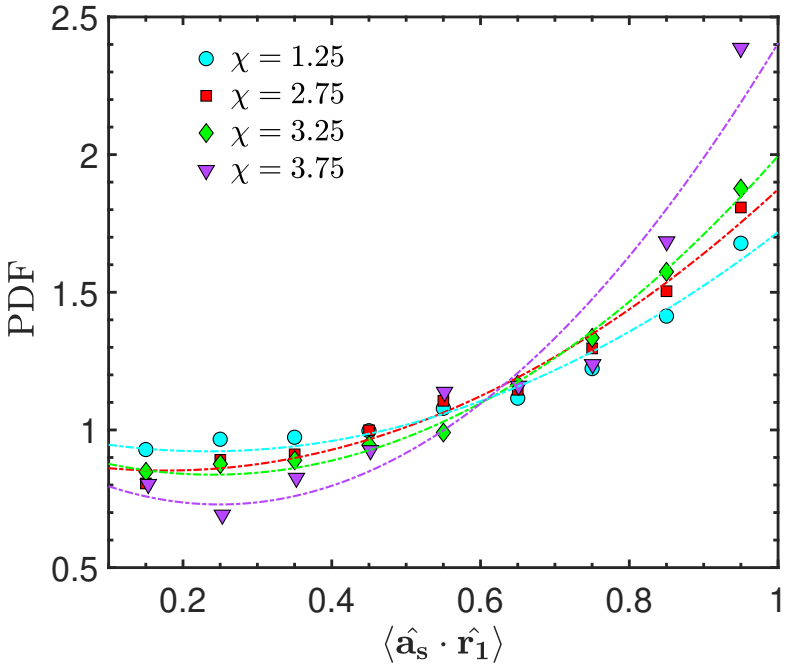


**Figure 5.7:** Probability density function of the cosine of the angle between the bubble semi-major axis ($\hat{\mathbf{r}}_1$) and the slip acceleration ($\hat{\mathbf{a}}_s$) for bubbles with different aspect ratios $\chi$.

a criterion of $r_2$ smaller or larger than $(r_1 + r_3)/2$ is used to separate prolate from oblate in our experimental results, about 59% bubbles are close to prolate spheroids, slightly higher than the remaining 41% oblate-like bubbles.

Figure 5.6(b) shows four lines calculated using the Lamb's potential flow model on spheroids (equation 5.1 in section §5) for prolate and oblate spheroids accelerating either *end-on* or *broadside-on*. All four lines start from $C_A = 0.5$ when $\chi = 1$ as expected. For either prolate or oblate spheroids accelerating *end-on*, $C_A$ reduces systematically as $\chi$ increases. For this case, an increasing $\chi$ works effectively as a reducing frontal area as spheroids accelerate through fluid, which results in a smaller volume of fluid that is being accelerated and hence a smaller $C_A$. The same principle also applies to the opposite limit, where spheroids accelerate *broadside-on*. In this limit, as $\chi$ increases, the frontal area increases and so does $C_A$. In addition, $C_A$ of oblate spheroids increases much more steeply compared to that of prolate spheroids because of the difference in their broadside projected area.

If the deformation and orientation of bubbles are completely random in turbulence, the estimated $C_A$ from our experiments should equal to the mean of all scenarios, including both oblate spheroids and prolate spheroids moving either *end-on* or *broadside-on*. However, figure 5.6(b) clearly shows that the measured results are closer to the *end-on* acceleration for either prolate or oblate spheroids, which suggests that, instead of being completely random, there may

be a preferential orientation between the bubble deformation and their relative acceleration in turbulence.

To confirm this conjecture, the PDF of the alignment between the bubble semi-major axis ($\mathrm{r}_1$) and slip acceleration ($\mathrm{a}_s$), i.e. $\langle \hat{\mathrm{a}_s} \cdot \hat{\mathrm{r}_1} \rangle$, for four different aspect ratios are shown in figure 5.7. If their orientations are completely random, the PDF of the dot product of the two unit vectors should follow a uniform distribution. A peak at around zero would suggest a perpendicular orientation, whereas a peak close to one would indicate an alignment between the two unit vectors. It can be seen that, in figure 5.7, a consistent preferential alignment between the bubble semi-major axis with the slip acceleration is observed for all aspect ratios considered, suggesting that bubbles prefer to accelerate along their semi-major axis (*end-on*). Moreover, such a preference seems to increase with $\chi$ as strongly-deformed bubbles align better with the slip acceleration. Therefore, putting together figures 5.7 and 5.6(b), it seems that the physical reason that $C_A$ of bubbles in intense turbulence gradually decreases as $\chi$ increases is because bubbles in strong turbulence prefer to deform and accelerate along their semi-major axis.

In figure 5.6(b), the results of $C_A$ seem to agree with but slightly higher than $C_A^{pe}$ (prolate, blue solid line) and $C_A^{oe}$ (oblate, red dashed line) predicted by the Lamb's theory for solid spheroids because these lines were calculated by assuming a perfect *end-on* acceleration. However, the distribution of the cosine

of the angle between $\hat{\mathbf{a}_s}$ and $\hat{\mathbf{r}_1}$ shown in figure 5.7 is not a perfect delta function at one; rather, bubbles in experiments have many other orientations that we do not have analytical solutions of. Averaging over all these orientations will inevitably make $C_A$ higher than the perfect *end-on* configuration where $C_A$ is the smallest. This qualitatively explains the observed similarities and differences in $C_A$ between the measured results for deformable bubbles and Lamb's solutions for rigid spheroids.

### 5.0.3 Basset History force

The added mass force is not the only unsteady force that bubbles will experience in intense turbulence. The additional contribution that comes from the history of boundary layer development induced by the varying slip acceleration between the two phases is the Basset history force, defined as:

$$\mathbf{F}_B = 6(D/2)^2\sqrt{\pi\rho_l\mu_l}\int_0^t \frac{(\mathbf{a}_b - \mathbf{a}_l)}{\sqrt{(t-\tau)}}\mathrm{d}\tau \tag{5.6}$$

where the slip acceleration $(\mathbf{a}_b - \mathbf{a}_l)$ is integrated with the Basset history kernel over previous time steps. For all the previous sections, this term is assumed to be zero. This assumption can be directly tested from our experimental results because all parameters in $F_B$, including the slip acceleration along each bubble trajectory, have already been acquired. In addition, rather than

integrating from 0 to the time instant $t$, we decide to integrate over $2\tau_\eta$ before $t$ because the acceleration of the fluid phase typically decorrelates at around $2\tau_\eta$ (Voth et al., 2002). After integrating over each bubble trajectory to estimate $F_B$, we calculate the standard deviation of $F_B$, which is about 20 times smaller than that of $F_A$. This difference suggests that the acceleration standard deviation is dominated by the added mass force. Since the Basset history force is associated with the history of the development of the viscous boundary layer, for our bubbles with the bubble Reynolds number $Re_b \sim 750$, this force becomes small. Moreover, in our calculation, including the Basset history force in the added mass force for finite-sized bubbles may cause $C_A$ to be overestimated by less than 5%, an uncertainty that is much smaller than other sources of error indicated by the error bar for $C_A$ shown in figure 5.6(b). Finally, although we can estimate $F_B$ from our experiments, our confidence of the calculated $F_B$ is rather low, as it requires an integration of acceleration. But we are certain that the standard deviation of $F_B$ is significantly overestimated because the standard deviation contains a large contribution from the measurement uncertainty that is accumulated and amplified through the integration. Given that an overestimated $F_B$ is still much smaller than $F_A$, ignoring the Basset history force for finite-sized bubbles transporting in turbulence is therefore well justified.

# CHAPTER 5. ADDED MASS COEFFICIENT OF DEFORMABLE BUBBLES IN TURBULENCE

## SUMMARY

Bubbles in turbulence are subject to multiple hydrodynamic forces that are sensitive to the bubble geometry. Among them, the unsteady forces, such as the added mass force and Basset history force, receive very little attention because of the technical challenges to extract them reliably and systematically from experiments, even though they could be important in turbulent flows. To address this problem, we developed an experimental framework combining a vertical water tunnel that produces intense turbulence with a diagnostic system that can measure gas bubbles and their surrounding turbulence simultaneously.

The lift and drag coefficients in the governing equation of motion for bubbles were determined from the mean velocity of bubbles and surrounding flows by Salibindla et al. (2020). Using these two coefficients, the bubble instantaneous acceleration can be estimated from the surrounding flow velocity and velocity gradients coarse-grained at the bubble size. The bubble acceleration can also be extracted from bubble trajectories directly. This independent estimation of the bubble acceleration from the two phases provides a unique way of evaluating the added mass force and coefficient. Note that the reliable extraction of the added mass coefficient requires an accurate measurement of turbulent velocity gradients, the acceleration of both the phases, and the full 3D bubble

shape reconstruction. This has really pushed the 3D flow measurements to the extreme.

The acceleration standard deviation determined from the two independent methods should be the same, and such a constraint helps to determine the added mass coefficient. We found that the bubble acceleration standard deviation appears to increase as the bubble aspect ratio grows. Based on this result, $C_A$ is found to decrease as bubbles deform more severely. Since $C_A$ is sensitive to both the shape and orientation of bubbles, we also investigate the relative orientation of the bubble semi-major axis, extracted from the 3D shape reconstruction, with the direction of their slip acceleration $\hat{\mathrm{a}}_s$. It turns out that deformed bubbles preferentially accelerate along their semi-major axis, and this preference seems to increase with the bubble aspect ratio. Based on the extracted bubble aspect ratio and assuming a perfect *end-on* configuration, $C_A$ is calculated from the Lamb's model, and the calculated trend shows a nice agreement with the measured results. Nevertheless, $C_A$ is slightly larger than the model prediction, which can be attributed to the fact that the Lamb's solutions only apply to a perfect *end-on* configuration where $C_A$ is the smallest. $C_A$ should increase if it is averaged over all possible bubble orientations in experiments that follow a wide distribution.

# Chapter 6

# Dissolution-driven convection in heterogeneous porous medium

*Motivated by the geological carbon sequestration, we study the dissolution-driven Rayleigh-Darcy convection in a Hele-Shaw cell with heterogeneous and anisotropic permeability by introducing a layer of discs. Even though adding one low-permeability layer changes the mean bulk permeability by less than 10%, its effect on the mass transfer rate can vary by more than 80%. In addition, the normalized permeability change, although collapsing a previous simulation with a uniform low permeability layer, does not work for our experimental results with a disc layer. We discover that our disc layer introduces several new length scales, and the coupling between the disc-disc distance and the finger width determines the mass transfer rate. With a simple model, we are able to decouple the effect of reduced number and density contrast of fingers. The over-*

*all trend of density contrast of fingers varying with disc-disc distance shows qualitative agreement with an independent measurement of the density contrast captured from the shadowgraph imaging. Our results show the importance of the length scale imposed by the heterogeneous porous medium and its roles in convective mass transfer.*

---

## INTRODUCTION

Fluid dynamics, such as flow instability (Riaz et al., 2006), Rayleigh-Bénard convection (Hidalgo et al., 2012), and multiphase flow (Cinar and Riaz, 2014), are critical in modeling subsurface carbon sequestration process. In practice, $CO_2$ is injected into aquifer filled with brine at a depth of more than 800 m underground. At such depth, $CO_2$ becomes supercritical ($scCO_2$) and it rises due to its smaller density comparing with ambient brine. If not controlled, this buoyant flow will eventually bring $CO_2$ back to the atmosphere, rendering an ineffective sequestration efforts. So most sequestration sites have an overlying caprock, a layer of low permeability rock, that the $CO_2$ cannot penetrate. $CO_2$ can only spread horizontally below the caprock, resulting in a two layer fluid system with $CO_2$ above brine.

At the interface, $CO_2$ slowly dissolves into brine and the density of the mix-

ture is higher than that of each individual fluid alone, thereby leading to an unstable configuration with heavier fluid on top of lighter one. This type of instability has been studied as a Rayleigh-Bénard convection problem and the key dimensionless number, Rayleigh number is defined as: $Ra = \Delta\rho g H k / \rho \nu D_m$, which represents the ratio of the buoyancy force to viscous and diffusive damping forces. Note that, since the flow stays in the Darcy flow regime, the definition of $Ra$ is slightly different with that of the turbulent convection problem (Ahlers, Grossmann, and Lohse, 2009; Lohse and Xia, 2010). In Ra, $\Delta\rho/\rho$ characterizes the ratio between the maximum density difference $\Delta\rho$ between the two-fluids mixture and the bottom fluid with density $\rho$. $k$ represents the permeability of the porous medium; $g$ and $H$ are the gravitational acceleration and height of the reservoir; $D_m$ is the mass diffusivity and $\nu$ is the viscosity of the mixture.

If Ra is small, the entire process is driven primarily by diffusion with any perturbations being damped by viscous forces and mass diffusion. When Ra approaches a critical number, any small disturbance will grow until it gains enough amplitude to set off the convection process (Emami-Meybodi et al., 2015). In addition to the Rayleigh number, another dimensionless number, the Sherwood number ($Sh$), is defined to represent convective mass flux of the dissolved $CO_2$ in brine, which is of practical importance. For Ra less than 1000, the convective mixing is transient and can be separated into several different

sub-processes: diffusive, early convective, and late convective (Meybodi and Hassanzadeh, 2013). However, we are interested in the high Rayleigh number Ra$\sim 10^4$, in which there is a so-called constant flux regime (Neufeld et al., 2010; Backhaus, Turitsyn, and Ecke, 2011; Hewitt, Neufeld, and Lister, 2014b). From experimental standpoint, this regime is ideal to study Sh-Ra relationship, since a constant flux lasts for a long period of time to provide sufficient statistics to estimate Sh accurately.

Figure 6.1 summarizes the Sh-Ra relationship over a wide range of Rayleigh number. This figure does not serve to review all the past work in this area, but to simply compile some existing data points to show the variations of Sh across different experiments (Neufeld et al., 2010; Backhaus, Turitsyn, and Ecke, 2011) and simulations (Hewitt, Neufeld, and Lister, 2014b; Graham and Steen, 1994; Otero et al., 2004; Farajzadeh et al., 2013). Even though these work focused primarily on the homogeneous and isotropic media with uniform permeability, the uncertainty of the Sherwood number across different work seems to be large. On the other hand, in practice, saline aquifers are highly heterogeneous and anisotropic across many different scales (Emami-Meybodi et al., 2015). This typically is manifested by the presence of multiple thin layers with high and low permeability (Jensen, Lake, et al., 1988). For example, the world's first $CO_2$ storage facility located in Sleipner offshore Norway has several layers of low permeability barriers in the entire reservoir, a configuration

that is hardly homogeneous or isotropic (Cavanagh and Haszeldine, 2014).

More recently, there have been several numerical work focussed on quantifying the effect of heterogeneity and anisotropy of the permeability field. The key in these simulations is to generate a 2D porous medium with a permeability distribution (Green and Ennis-King, 2014) or filled with many small flow barriers (Farajzadeh et al., 2011; Green and Ennis-King, 2014). For anisotropy, it was suggested that the dissolution flux should scale with the ratio of permeability in two different directions $k_v/k_h$ and independent of the configuration of the porous medium. The Dykstra-Parsons coefficient was utilized to quantify the heterogeneity (Farajzadeh et al., 2011). Depending on the range of this coefficient and correlation length, the dynamics of convection at Ra=5000 can be separated into three regimes: gravity fingering, channeling, and dispersive. In addition, the effect of a low permeability layer introduced in the middle of a Rayleigh-Bénard cell and the effects of this layer on the mixing rate and flow pattern was studied in depth (Hewitt, Neufeld, and Lister, 2014a; Guerrero-Martínez et al., 2017).

In this work, we tried to take a step back from generating a heterogeneous and anisotropic permeability field following a certain distribution, rather we conducted experiments on a simplified case by introducing just one low permeability layer. This simplified case can serve as a building block towards a more sophisticated permeability distribution and it will help us to gain more

insights into the dependence of convection on the interaction between the flow structures and flow barriers. We found that most previous models that tie the change of Sh to permeability cannot explain our experimental results. In addition, we discover the importance of the imposed length scale on the dissolution-driven convection. In §2, we introduce the parameters of two fluids mixture and how we estimate different dimensionless numbers. In §3, we present our experimental setup and the shadowgraph imaging method. Details of the experimental results and proposed model to describe the length scale effect are addressed in §4.

---

## PARAMETERS

It is quite challenging to conduct a laboratory experiment to study the dissolution-driven convection using supercritical $CO_2$ and brine at elevated pressure (100 bar). This motivates us to use a simpler analog fluid system, which maintains the key physics of the dissolution convection. Analogous fluids such as water - methanol, ethylene glycol (MEG) (Neufeld et al., 2010) and water - propylene glycol (PPG) (Agartan et al., 2015; Backhaus, Turitsyn, and Ecke, 2011) have been used before. These fluids are similar to the $CO_2$–brine fluid system, where the density of diffused interface is greater than the den-

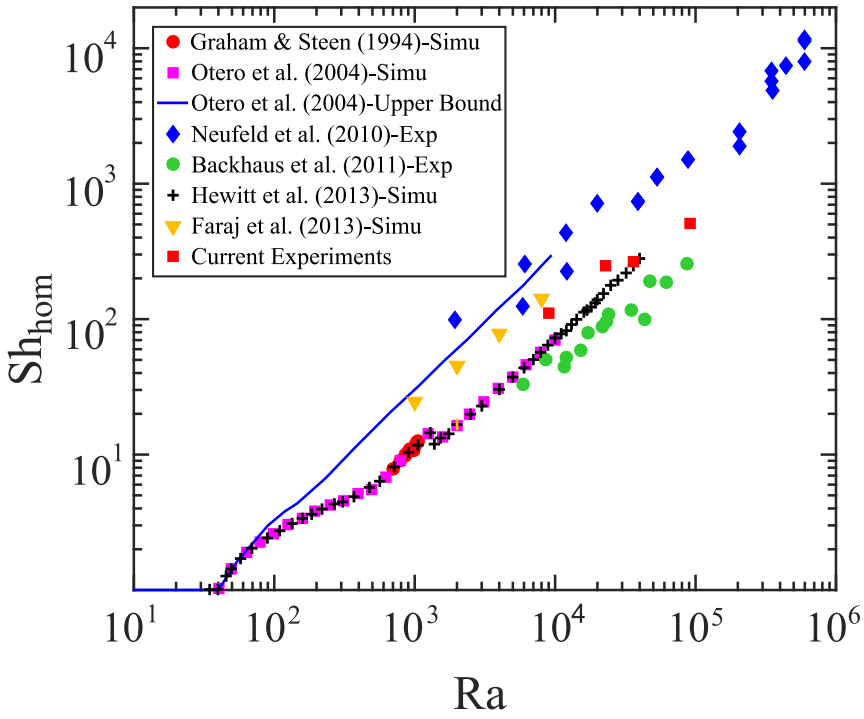


**Figure 6.1:** The compilation of existing data on the relationship between the Sherwood number (Sh) and the Rayleigh number (Ra) in a homogeneous porous medium from different simulations and experiments. Although the focus of this work is on dissolution rate in a heterogeneous medium at a fixed Rayleigh number, we have conducted the same Sh-Ra measurements on four different Rayleigh number (red squares).

sity of either fluids, thereby creating a positive buoyancy for dissolution-driven convection. In this study, water and PPG (Backhaus, Turitsyn, and Ecke, 2011) are used to replace $CO_2$ and brine. Density of water, $\rho_w = 1.00$ g/cc is lower than that of PPG, $\rho_{ppg} = 1.035$ g/cc. The diffusion of water in PPG at the interface results in a mixture. When water concentration $c_w$ in this mixture ranges from 0 to $\sim$50%, the density of mixture ($\rho_i$) becomes greater than either of these two liquids alone ($\rho_i \geq \rho_{ppg} > \rho_w$). The variation of mixture density as a function of $c_w$ can be estimated using an empirical equation:

$$\rho_i = 85.935{c_w}^3 - 217.62{c_w}^2 + 88.425c_w + 1034.1\ kg/m^3 \tag{6.1}$$

given by (Agartan et al., 2015).

Note that even though $\rho_i \geq \rho_{ppg}$ for $c_w = 0 \sim 50\%$, in this range, $\rho_i$ varies as a function of $c_w$ non-monotonically. It increases for $c_w$ =0 to 24 % and decreases for $c_w$=24 to 50% until it gets back to $\rho_{ppg}$. This density trend has been argued to result in a sub-linear Sh-Ra relation (Emami-Meybodi et al., 2015; Szulczewski, Hesse, and Juanes, 2013). But its effect on our study should be minimal, as we focus primarily on the heterogeneous and anisotropic porous medium at a constant Rayleigh number.

To simplify the parameter estimations, it is assumed that the concentration of the mixture $c_w$ at the interface is 0.3 with density $\rho_i = 1.044$ g/cm$^3$ (Back-

haus, Turitsyn, and Ecke, 2011). This results in a density difference between the mixture and underlying PPG: $\Delta\rho = \rho_i - \rho_{ppg} = 0.009$ g/cm$^3$. The terminal vertical velocity $v_c$ of a mixture finger with density $\rho_i$ is determined by a balance between buoyancy and viscous drag, $v_c = \Delta\rho g k/\rho_{ppg}\nu$. As the entire process is dominated by the fluid convection, $v_c$ is also referred to as the convective velocity. With such velocity, it takes the finger about $t_c = H/v_c$ time to travel the entire PPG layer with height $H$. On the other limit, if the mass transport is dominated solely by diffusion, it would take about time $t_d = H^2/D_m$ to pass the length scale H, thereby providing another velocity scale: the diffusive velocity $v_d = D_m/H$. $Ra$ can also be represented as the ratio between these two velocities Ra=$v_c/v_d$.

The dimensionless mass transfer rate is defined as the Sherwood number, Sh= $\dot{m}/\rho(D_m/H)bL$, the ratio between the total mass flux $\dot{m}$ and the diffusive mass flux. It is challenging to directly measure the value of mass flux, $\dot{m}$, from the experiments. So it is estimated from the interfacial velocity, because when the mass transfers downward across the interface, the incompressible fluid will cause the interface to move upward. The interfacial velocity is $v^* = dH^*/dt^*$, where $H^* = h(t^*)/H$ is the dimensionless height of the interface at any time instants. In this way, Sh is rewritten as a function of $Ra$ and interfacial velocity: Sh= $Ra(dH^*/dt^*)$, with the dimensionless timescale $t^* = t/t_c$. Although this estimation is not perfect, the time dependence of the interfacial position shows

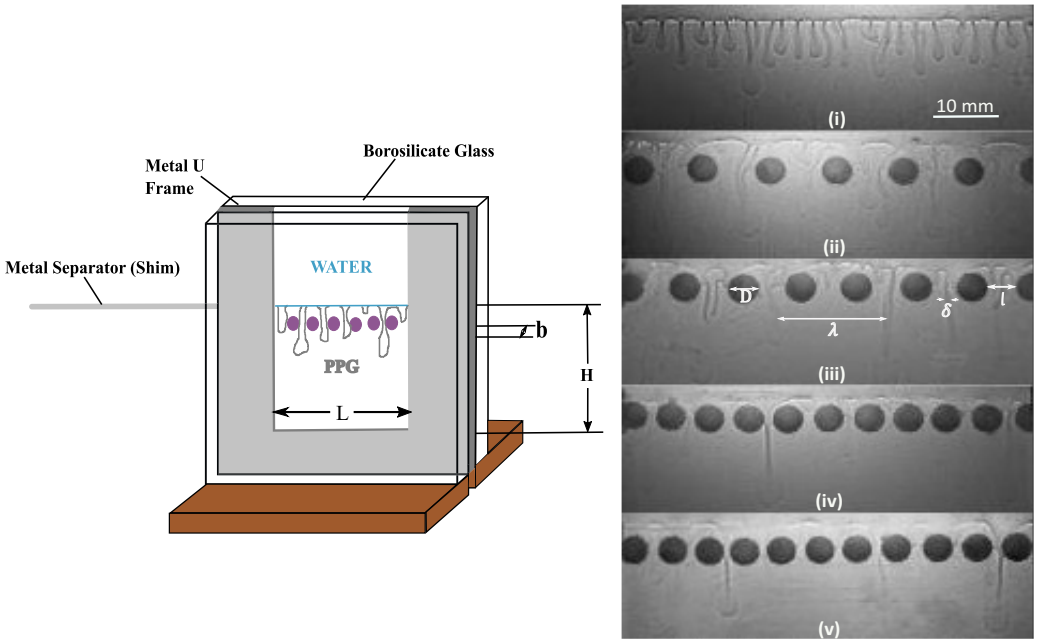


(a) (b)

**Figure 6.2:** (a) Schematic illustration of the experimental setup used as explained in section 6. (b) Shadowgraph images of water-PPG dissolution convection with i) no disc (homogeneous medium) and 4.5 mm discs placed at a distance of ii-v) $l = 5.50, 3.90, 1.49, 0.97$ mm.

significant portion of linear regime (>50% of the total timespan). It suggests that, after some time of development, the convective mass transfer reaches an asymptotic value that can be characterized by a single dimensionless number Sh. The slope of this linear curve represents $dH^*/dt^*$. Multiplying this number with the Rayleigh number gives Sh.

---

## EXPERIMENTAL SETUP: HELE-SHAW CELL

Figure 6.2a shows a schematic of the experimental setup in a vertical Hele-Shaw cell, made of two borosilicate glass pieces separated by a U-shaped metal frame. This metal frame sets the boundaries for the liquid layer with size 76 mm $\times$ 76 mm. The thickness, $b$, of the metal frames determines the thickness of the liquid layer, which are chosen to be $b = 0.254$ mm or $b = 0.508$ mm. This constant $b$ throughout the entire cell results in a uniform permeability $k = b^2/12$. This type of setup is referred to as the *homogeneous* configuration. Two layers of liquids (PPG and water) were filled into the Hele-Shaw cell. To avoid any perturbations at the interface and to provide a well-defined initial condition, a metal shim with the same thickness $b$ is used to separate two layers of liquids before experiments start. The initial height of the lower PPG layer, $H$, is an important parameter to determine the $Ra$. In this work, two different

heights with $H = 20$ mm and $50$ mm are used to extend the parameter regime.

A shadowgraph imaging system is constructed to visualize the convection process and quantify the mass flux. The system consists of a fiber optic light and a Fresnel lens to provide a parallel light source. The light transmits through the transparent fluid layers and projects a shadow onto a Mylar sheet. The refractive index mismatch at the interface between water and PPG will distort the light, resulting in changes of brightness at this thin layer. These changes will be used as a signature to detect the interfacial positions, as shown in figure 6.2b for various configurations. The interfacial position will help to quantify interfacial velocity and Sh. The shadow was captured by the Canon T5i camera. The camera was controlled in a time-lapse mode to take images at a framerate of 2 frames per minute. Each experiment takes about 7 hours in total.

---

EXPERIMENTAL RESULTS

### 6.0.1 Homogeneous Medium

In order to validate the measurements from the Hele-Shaw cell setup, we first conducted experiments without the disc layer. Figure 6.2 b(i) shows the shadowgraph image of the mixture in homogeneous medium with multiple

water-rich fingers flowing into the PPG below. Motivated by Utsira sand formation in Sleipner site of North Sea with the Rayleigh number of the order $\sim 10^4$ (Neufeld et al., 2010), a series of experimental setup with $H = 20,\ 50$ mm and $b = 0.254,\ 0.508$ mm were used to cover a range of $Ra = 10^4 \sim 10^5$. The Sherwood number calculated from these experiments were plotted and compared with the data from previous work as shown in figure 6.1. Both data scattering and the scaling exponent of Sh-Ra in our experiments are very similar to the one in the previous experiment with a similar configuration (Backhaus, Turitsyn, and Ecke, 2011). We do realize that our Sherwood number is systematically higher than the previous work (ibid.). To make sure that it is not due to the chemical differences, we have conducted several test experiments with different Propylene Glycol from different vendors (Essential Depot, Dow Chemicals) and different types of water, including tap water and distilled water. It turns out tap water will lead to about 11% overestimation of the mass dissolution rate. But as long as we use the distilled water, the reproducibility of our experiment remain in the 6.5% range, including two different types of PPG that we used. The systematic shift between our datasets and the one from Backhaus, Turitsyn, and Ecke (ibid.) is much larger than 6.5%, indicating that this shift may not be due to chemical differences. In addition, although our Sh is larger, they are still within the range set by two different experiments by Neufeld et al. (2010) and Backhaus, Turitsyn, and Ecke (2011). This implies

that the Sherwood number uncertainty, although remaining low for one setup, may still vary among different groups in different setups.

### 6.0.2 Heterogeneous Medium

We choose two Rayleigh numbers, $Ra = 9.87 \times 10^3$ and $Ra = 2.27 \times 10^4$, to study the heterogeneity effect. Motivated by those low permeability layers in actual reservoir for conducting carbon sequestration, heterogeneity is introduced to the Hele-Shaw cell by inserting some Latex rubber discs with the same thickness as the cell. So those discs will block the flow pathway, creating local zero permeability. Three disc diameter were used : $D = 2.5$ mm, $3.5$ mm and $4.5$ mm. In geological formation, low permeability layers are always filled with many high-permeability fractures in them. In our configuration, as shown in figure 6.2b(iii), the spacing between these discs $l$ represents the fracture width and the size of these discs $D$ represents the fracture distribution through the low permeability barrier. In this work, only one single layer of these discs were added at a distance of 2 mm from the interface. The effect of this distance will be discussed in §6.0.2.4. Besides those length scales, for the developed viscous fingers, $\lambda$ is the inter-finger distance and $\delta$ is the finger width.

From figure 6.2b(i) to 6.2b(v), $l$ decreases from $\infty$ (no disc) to less than the finger width ($< \delta$). From those shadowgraph images, we have observed two systematical changes: a) the number of downward moving viscous fingers de-

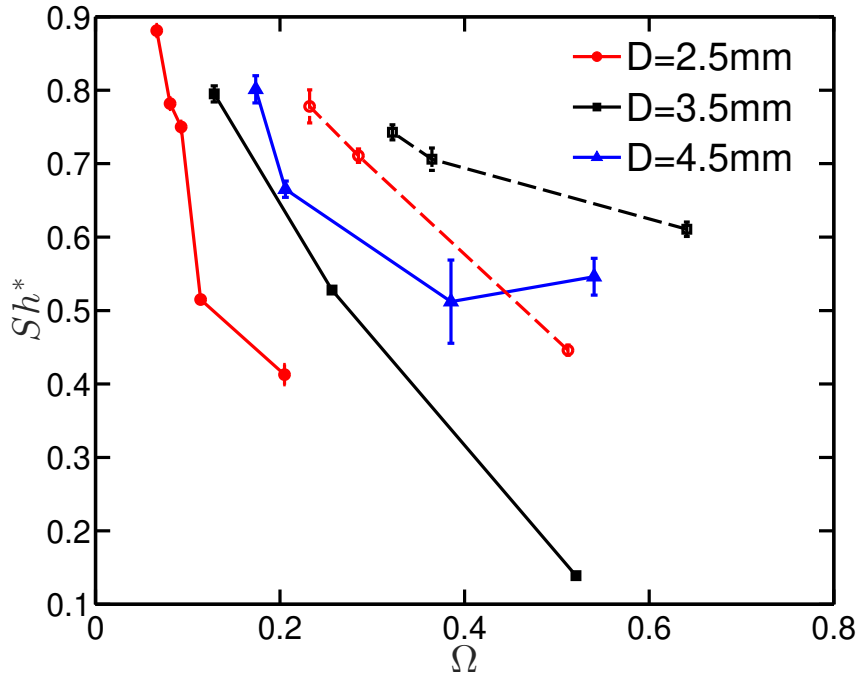


**Figure 6.3:** Normalized heterogeneous Sh number (normalized by $Sh_{hom}$) versus the normalized impedance, $\Omega$ for various disc sizes at $Ra = 9.87 \times 10^3$ (dashed lines) and $2.27 \times 10^4$ (solid lines).

creases with decreasing $l$, and b) the interface between water and PPG seem to blur as $l$ decreases. When $l$ becomes small, it is actually very challenging to detect the fluid interface in figure 6.2b(v). These two observations inspire our model, which will be introduced later in §6.4.

#### 6.0.2.1 Permeability

To connect those observations from some other measurable quantities, we first consider the permeability. Permeability measures the capability of the porous medium to allow the liquid to flow through. It is one of the most important parameters in porous flow, because of its connection to the Darcy's law. If

introducing those discs only affects the mean permeability $k$, incorporating this change in the Rayleigh number will help to predict the mass transfer rate for heterogeneous case. If this is indeed the case, the prediction of solubility trapping of geological carbon sequestration would depend only on the mean reservoir permeability. The details of our method to characterize the permeability of the entire cell and the disc layer are included in the Appendix. From those measurements, we realize that, since those discs only consist a small portion of volume of the entire cell, they would change the mean bulk permeability by less than $10\%$. This will be translated to $\sim 10\%$ change for the Rayleigh number and eventually the Sherwood number. This is inconsistent with our experimental findings that the mass flux can decrease over $80\%$, which is much larger than the prediction based on the mean permeability hypothesis.

It is possible that the mass transfer rate may still depend on the permeability, but more on the permeability of the disc layer alone $k_l$ rather than the mean value. This effect has been studied using the numerical method on a two-sided convection system (Hewitt, Neufeld, and Lister, 2014a). In this system, the authors have introduced a similar low-permeability layer. The difference is that they prescribe a uniform permeability throughout the entire layer, whereas our configuration employs a disc-gap design with alternating low and high permeability. The layer thickness, same as the disc diameter, is denoted by $D$, so the relative thickness is given by $D/H$ with respect to the total height of the

convection $H$.

One of the important conclusions in the previous simulation is that the permeability of the thin low-permeability layer determines the mass transfer rate (Hewitt, Neufeld, and Lister, 2014a). In order to explain the dependency of Sh on different $k_l$, Hewitt, Neufeld, and Lister (ibid.) introduces a non-dimensionalized impedance, $\Omega = (D/H)/(k_l/k)$. Note that the impedance denotes the inverse of the permeability.

It has been shown that, using $\Omega$ helps to collapse all data points onto one curve in the previous work (ibid.). This motivates us to utilize the same framework to explain the Sherwood number dependence. The measured Sherwood number from experiments with a disc layer ($Sh_{het}$) was normalized by its respective homogeneous Sherwood number without discs ($Sh_{hom}$), giving $Sh^* = Sh_{het}/Sh_{hom}$. In figure 6.3, $Sh^*$ is shown as a function of the impedance $\Omega$, calculated based on different combinations of disc gaps and sizes (details are listed in the Appendix).

Although the data seems to follow a similar trend, it is apparent that the our results with different disc configurations do not collapse, unlike the results from the previous simulation. There are two possible reasons: (a) the simulation work focused on two-sided thermal convection, whereas our experiment is driven by one-sided dissolution-driven convection. So our flow does not exhibit structures like large-scale circulation shown in the simulation. (b) The way

that the low-permeability layer is introduced is very different. This implies that there is a new parameter that cannot be lumped into the permeability. The question arises as to what this new parameter might be.

In addition, at $\Omega = 0.1 \sim 0.3$, it has been observed in the simulation that Sh can actually be slightly higher than that in the homogeneous case without the low-permeability barrier (Hewitt, Neufeld, and Lister, 2014a). However, in our case, Sh of all heterogeneous cases are lower than their homogeneous counterpart. This has been attributed to the ordered cellular flow structure, which is again a unique flow feature of the two-sided convection. Nevertheless, the key idea of using permeability to explain the difference of Sh used in multiple other simulations (Farajzadeh et al., 2011; Green and Ennis-King, 2014) does not work for our experimental results, and it is the goal of this chapter to answer why.

#### 6.0.2.2 New length scales

To approach this problem from a new perspective other than the permeability, we need to understand the details of the dynamics. The convective mass transfer from water to PPG is primarily through those downward moving fingers. They can be clearly visualized in figure 6.2b. Near the interface at onset, instability occurs across many different wavelengths, and as a result, many closely spaced fingers emerge. They cannot all come down because the

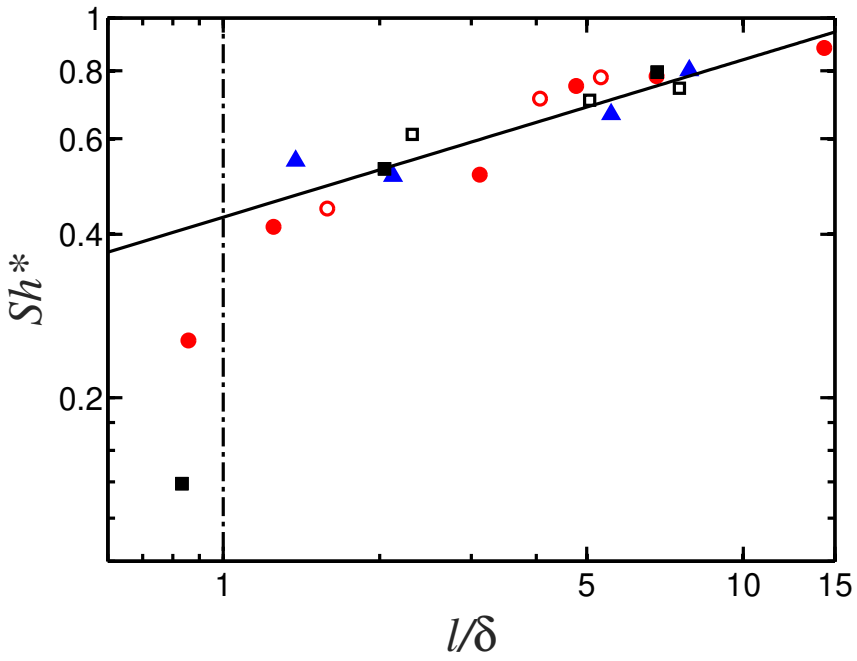


**Figure 6.4:** The relation between normalized Sh number ($Sh^*$) and the dimensionless length scale, $l/\delta$ imposed by the low permeability disc layer. The error bar indicates the uncertainty of Sh estimated by calculating mass transfer rate at shorter time windows.

incompressible flow condition requires some flow moving upward to balance the mass transfer of downward moving fingers. Those flows will push against fingers, leaving them with no choice, but to move aside, collide and merge with others, resulting in small number of long standing fingers in the PPG layer.

At the steady state when the mass transfer rate is constant, the number of fingers reaches an asymptotic value, and this can be quantified using a dimensionless length scale $\delta/\lambda$, ratio between finger width $\delta$ and finger-to-finger separation $\lambda$. It is obvious that the mass transfer rate from water to PPG should be proportional to number of fingers as they carry most water and travel down at a much faster velocity comparing with diffusion. In this sense, $Sh \sim \delta/\lambda$ and the length scale plays an important role in determining Sh.

For our configuration, experiments were conducted using various disc size ($D$) and spacing ($l$). As the disc layer contains alternating low and high permeability zones, the fingers can only pass through those gaps between discs and that introduces new length scales. If the disc layer is so close to the interface that the fingers cannot naturally develop and merge into the final value of $\delta/\lambda$, they have to comply with the length scale that is imposed by the disc layer. So our next hypothesis is that the $l/D$ might be a new parameter to collapse all the results. However, it does not work either, as the normalized permeability of the disc layer $k_l$ is related to $l/D$ (the details of their relationship can be found in the Appendix). In another word, it implies that $l/D$ provides a similar mea-

sure of the disc layer as the permeability ($k_l$), so it does not introduce a new parameter that we need.

After watching the shadowgraph movies for many times, we observe some interesting results. When the gap size $l$ is wide enough, some fingers that developed from the water-PPG interface can pass straight from liquid interface through disc layer via those gaps. However, when we make $l$ smaller and smaller, eventually no fingers emerged from interface can freely pass the gap. Based on this observation, we realize that each finger is very unlikely to be affected by another one that is several times disc diameter away, because those zero-permeability discs essentially prevent any hydrodynamic interactions across. Therefore, each finger is independent, and they only care if the gap size is large enough to pass. So it is the ratio between plume width and gap size that matters. This introduces a new dimensionless parameter $l/\delta$.

The normalized Sherwood number ($Sh^*$) from the experiments was then plotted against this parameter, $l/\delta$, as shown in figure 6.4. Note that the value of $\delta$ was found to be approximately a constant at $0.7$ mm for all experiments. In this plot, the data from all combinations of disc configurations and Rayleigh number collapse very well onto each other. This implies that $l/\delta$ is indeed the new parameter introduced by the disc layer. The surprising part is that the results are independent of the disc size $D$, at least in the range of $D$ that we used. Note that $D$ represents both the gap spacing and thickness

of the low-permeability layer. This potentially can bring an important implication to the carbon sequestration or any types of hydrodynamic instability in the porous medium. If the formation has some low permeability layers filled with fractures, the layer thickness and fractures-to-fractures spacing might be secondary. It is possible that the ratio between the mean fracture width and typical flow length scale matters the most. This implication is not conclusive, but it does provide a prediction that can be tested in field experiments.

As shown in figure 6.4, the dynamics exhibit two different behaviors that can be divided into two regions by the vertical dashed line represented by $l/\delta = 1$, which is consistent with our observations that the fingering dynamics have a transition at $l \approx \delta$. To the right of this line, where $l > \delta$, the disc spacing is wide enough to allow fingers to pass freely through those gaps, resulting in a relatively high convective mass flux. In this regime, $Sh^*$ seems to scale with $l/\delta$ in a power-law relationship.

$$Sh^* = 0.46(l/\delta)^{0.29} \tag{6.2}$$

The scaling exponent is not fixed, but varies with the distance between the disc layer to the two-fluids interface, which will be discussed in §6.0.2.4 and requires further research. In addition to this regime, to the left of vertical dashed line ($l < \delta$), no plumes can freely pass through these gaps. They are

forced to mix with the PPG above the disc layer. But after some time, the new mixture can penetrate through those small gaps by forming new fingers. Those new fingers have the same width as the disc gap $l$ and they tend to contain less density contrast comparing with those from the water-PPG interface. That is why the convective mass flux is much smaller.

To understand the relationship between $Sh^*$ and $l/\delta$, we start by modeling the mass transfer rate and relating it to finger characteristics. As mentioned before, fingers carry high concentration of water and its motion in PPG layer can be translated to the convective mass transfer rate. The mass transfer rate carried by those fingers should depend on their size (including width $\delta$ and thickness $b$), number $n$, velocity $u_f$, and density. In sum, Sh is proportional to $\rho b c_w u_f n \delta$, resulting in $Sh/Ra = c_w(\delta/\lambda)(u_f/u_c)$ (Backhaus, Turitsyn, and Ecke, 2011). Therefore, two main contributions for mass flux rate is the finger width and velocity. The density contrast between the mixture in fingers and the background PPG is lumped in the Rayleigh number.

In the homogeneous configuration, $u_f/u_c$ is not independent; rather, it is a result of viscous contrast of two fluids and the relative finger width. The convective velocity $u_c$ is an effective bulk velocity taking finger velocity $u_f$ and back flow velocity $u_b$ into account. They can be related as $u_f/u_c = 1/[1 + (\nu_{PPG}/\nu_w)\delta/(\lambda - \delta)]$ by conducting a path integral of the Darcy's law from finger center to back flow center. As $u_b$ can also be related back to $u_f$ with incom-

pressible flow condition, this leads to a new equation: $Sh = Ra\{c_w(\delta/\lambda)/[1 + (\nu_{PPG}/\nu_w)(\delta/\lambda)/(1 - \delta/\lambda)]\}$ (Backhaus, Turitsyn, and Ecke, 2011). In this equation, it can be observed that the effects of number of plumes ($n_p \propto 1/\lambda$ ) and plume velocity ($v_c \propto Ra$) were decoupled. We assume that the same equation can be used to decouple these two effects in heterogeneous and anisotropic medium.

Adding the low permeability disc layer is found to reduce both the factors mentioned above. From the shadowgraph images shown in figure 6.2b, it is evident that as the distance between the $4.5$ mm discs is reduced from $l = 5.5$ mm to $0.97$ mm, the number of plumes reduces and the wavelength $\lambda$ increases. In fact, when compared with the homogeneous case, number of plumes reduce from $n_p = 25$ (figure 6.2b(i)) to $n_p = 3$ (figure 6.2b(v)).

The low permeability layer also reduces the plume density and velocity, which is explained as shown in figure 6.5(a). The disc layer divides the PPG layer into top and bottom regions. When fingers hit those discs, they have to turn back and mix with the rest of the top PPG region, thereby increasing the density of the top PPG region $\rho_{top}$, at the expense of decreasing density contrast of fingers ($\rho_i$ reduces to $\rho_{top}$). This reduced density contrast leads to smaller buoyancy force and thus smaller convective velocity $v_c$ of fingers on average. In order to account for this mixing, we define an effective Rayleigh number as

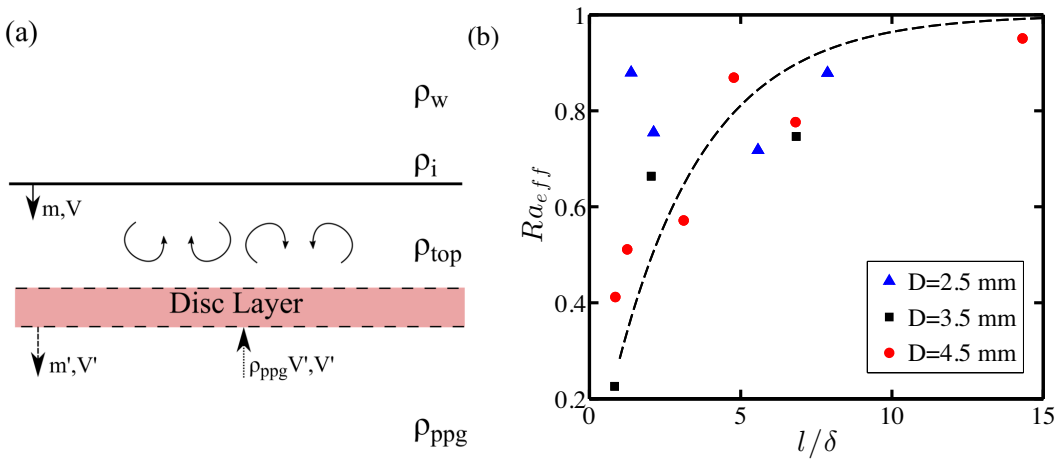


**Figure 6.5:** (a) The sketch of the mixing induced by the disc layer and its impact on the mass dissolution rate, (b) The normalized effective Rayleigh number ($Ra_{eff}$) versus $l/\delta$. The Ra$_{eff}$ is normalized in such a way that it will range from 0 to 1, instead of from the lower limit at 908 ($l = 0$) to the upper limit at $2.27 \times 10^4$ ($l = \infty$ with no discs). The dashed line is the exponential fit to all data points, Ra$_{eff} = 1 - exp(l/3\delta)$.

$$Ra_{eff} = \frac{(\rho_i - \rho_{top})\ gkH}{\nu D_m} \tag{6.3}$$

We define $Sh_{het}$ as:

$$Sh_{het} = f(\delta/\lambda)\ Ra_{eff} \tag{6.4}$$

In equation 6.3, the density difference is between the fluid mixture at the water-PPG interface $\rho_i$ and the mean density in the top PPG region $\rho_{top}$. In order to get the values of $Ra_{eff}$, equation 6.4 is rearranged to give $Ra_{eff}$ as a ratio of $Sh_{het}$ and $f(\delta/\lambda)$. Both the heterogeneous Sh number, $Sh_{het}$ and inter-plume distance, $\lambda$ can be measured from the experiments with various disc configurations. As the plume width, $\delta$ was found to be constant at 0.7 mm for

all the cases, the values of $\lambda$ were used to calculate $f(\delta/\lambda)$.

Experimentally acquired $Sh_{het}$ and $f(\delta/\lambda)$ were then substituted to calculate $Ra_{eff}$ and plotted as a function of $l/\delta$ for all three disc sizes in figure 6.5(b). The $Ra_{eff}$ is normalized by calculating $(Ra_{eff} - 908)/(2.27 \times 10^4 - 908)$, so it will range from the lower limit at 0 to the upper limit at 1, rather than from 908 to $2.27 \times 10^4$. The upper limit represents the Rayleigh number for the homogeneous case with no discs, which is about $2.27 \times 10^4$. The buoyancy force is maximum when no discs are introduced and there is no enhanced mixing in the top PPG region. The lower limit, on the other hand, is about 908, when there is no gap between discs ($l = 0$ mm). This is equivalent to set the cell height $H = 2$ mm. It can be seen that the trend of $Ra_{eff}$ in figure 6.5 for all three sizes indeed approaches these two limits as we expected. This trend can be fitted with an exponential function:

$$Ra_{eff} = 1 - exp(-l/3\delta). \tag{6.5}$$

#### 6.0.2.3 Density gradient

An independent way to confirm the calculated trend of $\mathrm{Ra}_{eff}$ is to directly measure $\mathrm{Ra}_{eff}$ through the density gradient $\rho_i - \rho_{top}$ for each disc configuration. Acquiring this density gradient, however, is very challenging. In this study, we decide to use shadowgraph imaging to indirectly infer the density

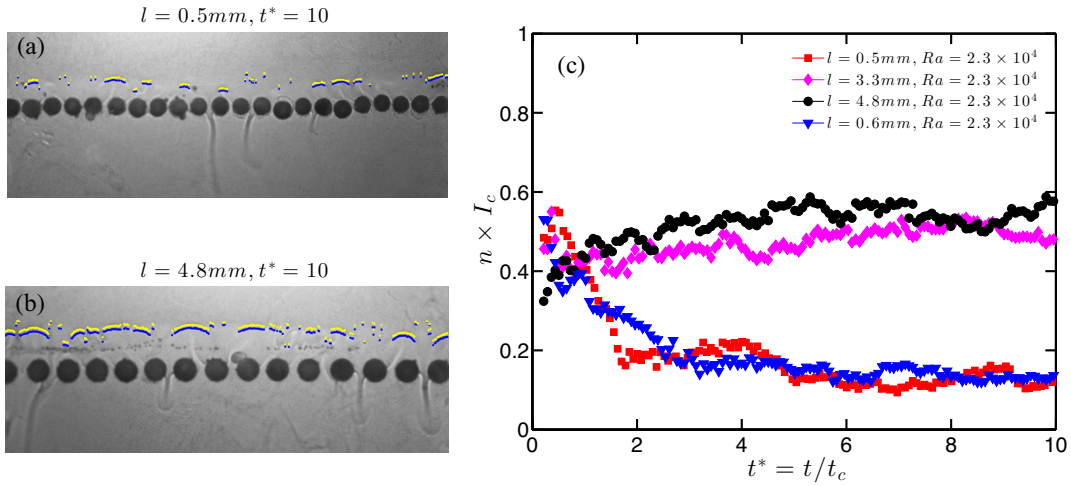


**Figure 6.6:** Interface location and contrast detection. (a-b) The refractive index gradient across the interface is extracted and the bright and dark areas on the interface is illustrated by a pair of yellow and blue dots. The number of dots ($n$) shows the length of the fragmented interface and the brightness contrast ($I_c$)between a pairs of dots indicate the density gradient . (c) The total density contrast $n \times I_c$ evolves as a function of dimensionless timescale $t^*$

gradient across the interface. The intensity gradient in the shadowgraph image is related to the second spatial derivative of refractive index (Settles, 2012). For the liquids used, the refractive index gradient is related to the density gradient with a nontrivial relationship (Dow, 2000). But we assume that $\rho_i - \rho_{top}$ monotonically changes with intensity gradient in the image for simplicity.

Figure 6.6 (a-b) show the interface development in two disc configurations, with $l = 0.5$ mm and $l = 4.8$ mm respectively. The interface with strongest density gradient shows as a dark line above a white line, because light is preferably refracted from the upper layer to the lower layer. This signature can be utilized in the interface extraction code to identify the interface location. The code runs through each vertical line of pixels above the disc layer and identify the loca-

tion of the strongest intensity gradient. Along this strongest gradient, the peak is marked as blue dot, whereas the valley is marked as yellow dot. Repeating the same calculation over all vertical lines will lead to the identified interfaces, as shown in these two figures as a series of blue and yellow dots. In both cases with a disc layer, it can be seen that the interface is broken into segments, in contrast with a single and continuous interface in the homogeneous configuration with no disc layer. This interface fragmentation is worse for the case with small disc distance. It is because of the reduced density gradient caused by the enhanced mixing in the upper PPG layer above the discs. Number of pixels ($n$) that can be successful detected at the interface is used to quantify the interface fragmentation. In addition, each detected interface comes with the pixel brightness at the peak and the valley, whose differences can be used to quantify the intensity contrast across the interface $I_c$. So combining two effects $n \times I_c$ provides an evaluation of the intensity and density contrast. For the following discussion, we refer $n \times I_c$ as a measure of density gradient.

Figure 6.6 (c) shows the time evolution of $n \times I_c$ as a function of $t^*$. Four disc configurations are used and they are separated as two groups. For large disc separation $l > 2$ mm, the density gradient does not change much. This is consistent with the small time variation of density gradient across the interface for the extreme case $l \to \infty$ in the homogeneous configuration. The other group for small disc separation $l < 2$ mm shows a large drop of density gradient. This

is due to the enhanced mixing of the top PPG layer forced by the added disc layer. This process occurs primarily in the short time limit $t^* < 3$. It suggests that, after $t^* \sim 3$, the density of top PPG layer $\rho_{top}$ does not change much because the fresh water coming in from the interface mixes with the fresh PPG exchanged at the disc layer will result in a similar $\rho_{top}$. Although these results are based on intensity gradient and are rather indirect on density gradient, it supports our model and the calculated trend of $\mathrm{Ra}_{eff}$: the reduced density contrast results in a smaller buoyancy force and thus smaller convective velocity, and this effect becomes stronger for small disc separation.

#### 6.0.2.4 Interface position

In the end, we would like to study the effect of relative distance between the disc layer to the fluids interface $h$. There are two extreme cases, $h = 0$ and $h = H$. Complex disc and boundary layer interaction will lead to uncontrolled dynamics at $h = 0$, which is not in the scope of the current work. We decide to start with $h = 3\delta$ (2 mm), which is three times boundary layer thickness away to ensure that the disc does not interfere with boundary layer dynamics. All the previous discussions are on this specific $h$. The other limit is $h = H$. In this case, the disc is at the bottom of PPG layer, and it will do very little to the fingering dynamics. In order to investigate how the Sherwood number transits from one limit to the other, we have measured the Sherwood number

as a function of $h$.

As shown in figure 6.7(a), the interface height rises as a function of time for four different $h$. But instead of following a linear curve through the entire constant-flux convective regime, it switches from one linear regime to the other, and the transition time delays longer for a larger $h$. This transition time is shown in table 6.1 along with other two timescales that are related to the time it takes for the fingers to reach the disc layer ($t_1$) and leave the disc layer ($t_2$). Before the fingers touch the disc layer, they do not feel its existence, because the disc layer has very small effect to the overall permeability. In this regime, the slope of the linear curve is exactly the same as that of the no-disc homogeneous case.

The transition time is roughly two times of $t_2$. If it takes fingers $t_2$ to move from the interface to the bottom of the disc layer, it will take another $t_2$ time to bring the disc layer effect back to the interface to complete the mixing. After the transition, the curve in figure 6.7(a) turns into a different linear regime with a much smaller slope. $\mathrm{Sh}^*$ based on this slope is shown as a function of $h$ in figure 6.7(b). We have tested it in two disc configurations with different disc-to-disc separations $l/\delta$, and it shows a similar trend towards an asymptotic value of $\mathrm{Sh}^*$. Since one might expect that disc layer effect is vanishing and $\mathrm{Sh}^*$ gets to one as the disc layer gets farther and farther away, it is very surprising that the asymptotic value of $\mathrm{Sh}^*$ is not even close to one. It suggests that the

| $h$ | $t_1$ (s) | $t_2$ (s) | Transition time (s) |
|---|---|---|---|
| 2 mm | 0.47 | 0.87 | 1.65 |
| 7 mm | 0.76 | 1.31 | 2.78 |
| 10 mm | 1.96 | 2.43 | 4.83 |
| 20 mm | 4 | 4.54 | 10.03 |

**Table 6.1:** The list of key timescales as a function of the vertical distance $h$ between the disc layer and the interface. $t_1$ and $t_2$ represent the time when the fingers reach and leave the disc layer, respectively; The transition time is the time that separates two linear regimes, as shown in figure 6.7(a).

disc layer effect only gets delayed, but not disappears, as long as those fingers have not fully mixed with the background fluid.

---

## SUMMARY

In this chapter, we have conducted experimental investigations to study the dissolution-driven convection in a heterogeneous and anisotropic porous medium. A disc layer with alternating low and high permeability gaps is introduced, and the disc size ($D$) and the disc spacings ($l$) were systematically varied in order to study the dependence of the dimensionless mass transfer rate, i.e, Sh on those parameters.

Since the flow is in the Darcy's regime, it is natural starting point to study the dependence of Sh with the changes of permeability. We find that, even though the permeability change due to disc layer is less than 10%, it can bring

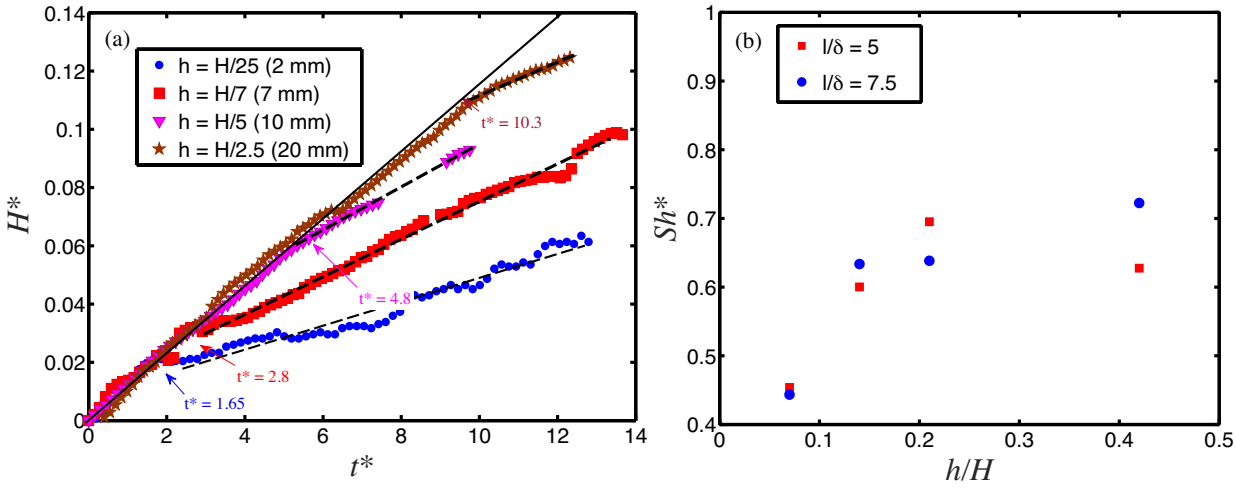


**Figure 6.7:** (a) The interface height $H^*$ rises as a function of time for the disc layer that locates at $h$ away from the interface. The slope of the curve represents the dissolution rate, and thus the Sh. In each curve, there is a transition time (indicated by the arrows) that separates the curve into two linear regimes. The slope of the one before transition is the same as that of the no-disc homogeneous case, as shown by the solid line. Dashed lines show the linear fit to all curves after the transition. (b) The normalized Sherwood number (obtained from the slope of the curve after the transition) is shown as a function of $h$.

over 80% changes to Sh. In addition, the normalized impedance used in previous simulation result does not help to collapse our experimental results, indicating that we have some important parameters in our experiments that cannot be explained by permeability alone.

It turns out that this missing parameter is the ratio between disc spacing $l$ and the finger width $\delta$. In other words, the coupling between the imposed length scale and the flow length scale decides the mass transfer rate. There are two different regimes that are separated by $l/\delta \approx 1$, below which the fingers cannot freely pass the gap and be forced to mix with the fluid above the disc. For $l/\delta > 1$, Sh scales with $l/\delta$ following a power law relationship.

To explain the dependence of Sh with $l/\delta$, we utilize the model developed by Backhaus, Turitsyn, and Ecke (2011) to decouple the effect of reduced fingers' number and density due to mixing. The number of fingers can be determined from the experimental results. To capture the reduced density of fingers, we introduce a new effective Rayleigh number $\mathrm{Ra}_{eff}$. Two ways have been used to estimate the trend of $\mathrm{Ra}_{eff}$, one indirectly calculated from Sh and number of fingers and the other one infered from the intensity gradient in the shadowgraph imaging. These two results show qualitative agreement that the small disc spacing tends to drive the mixing of fluids above the disc layer, thus reducing the density gradient of the fingers.

Our result shows clearly that introducing low permeability flow barriers in

otherwise homogeneous medium can bring effects more than just altering the permeability distribution. The length scale of the flow barriers can couple with the flow length scale and lead to significant change of the flow characteristics. In the end, we realize that the relative location of the disc layer has a surprising effect on the dissolution rate. As disc layer becomes far away from the interface, its effect on Sh only gets delayed but not disappears, and the transition time is related to the time it takes for the fingers to penetrate the disc layer.

# Chapter 7

# Summary and conclusions

In this thesis, we experimentally investigated the closure models for interfacial mass and momentum transfer of two-phase flows under two different flow conditions, namely, (i) high-$Re$ turbulent flows, and (ii) low-$Re$ porous medium flows. The former case focused on immiscible air-water system in the limit of intense turbulent medium, where the momentum exchange term in two-phase flow equations 1.1 to 1.3 is very important but the mass exchange term could be ignored. In the opposite limit, we explored the mixing of water-propylene glycol in a heterogeneous porous medium with the mass exchange term being of prime importance. Each system came with its own experimental framework that was carefully designed to reliably extract quantitative information about both the phases. Most of the current work that encompasses chapters 2 to 5 focused on the former case, where finite-size deformable air bubbles tumble and

deform in intense turbulent environments.

In chapter 2, we provided a summary of existing experimental setups that were formerly used to study turbulent multi-phase flows with dispersed particles. The discussions in this chapter were limited to two-phase flows and setups with homogeneous isotropic turbulence. The key challenge was to use these classical experimental facilities that were designed for investigating single-phase turbulence and adapt them to probe multi-phase flows. More importantly, the design of diagnostic system was crucial to simultaneously probe all the phases over a wide range of void fractions. Therefore, a significant part of this chapter was dedicated to review some established diagnostic systems that were based on the optical, electrical and other radiation based measurements like X-rays. Each technique comes with its own strengths and limitations and the decision of choosing the appropriate system depends on multiple factors such as the (i) the physical and optical parameters of the two phases; (ii) the void fraction of dispersed phase; (iii) the size and complexity of the system; (iv) how invasive is the measurement system; (v) required spatio-temporal resolutions; (vi) two or three dimensional measurements; and (vii) desired quantities to be measured like the void fraction distribution, particle size and shapes, flow velocity, interfacial area, and flow topology to name a few. Thus, one needs to keep in mind the type of measurements that are needed for their analysis before deciding on the type of diagnostic system.

Subsequently, in chapter 2, we also described the design and working of our experimental setup called the vertical octagonal non-corrosive stirred energetic turbulence (V-ONSET) that was built with the purpose of exploring the dynamics of finite-sized bubbles deforming in intense turbulent environments. A key features of our facility is its high energy homogeneous isotropic turbulence ($\epsilon \sim O(0.1)$ m$^2$/s$^3$) in conjunction with a controllable mean flow. This ensured that the finite-sized bubbles injected into the flow within the size range of 1 to 10 mm were primarily deformed by the turbulent fluctuations in the surrounding flow rather than the buoyancy induced forces. In addition, the V-ONSET diagnostic system uses six high-speed cameras placed strategically around an octagonal test-section in order to obtain 3D Lagrangian measurements of both the phases simultaneously. This was made possible by using the particle shadow technique with density matched tracer particles in the continuous water phase. Each camera had a dedicated LED to provide back-lighting that simultaneously casts the shadows of the bubbles and tracer particles.

Later on, two separate 3D reconstruction codes developed in-house by Masuk, Salibindla, and Ni (2019) and Tan et al. (2020a) were used to merge these images captured by the six cameras in order to acquire 3D Lagrangian information of each phase individually. The first code, called the virtual camera based visual hull (VCVH) method uses additional physical constraints imposed by the surface tension between the air and water to improve the quality of the recon-

structed 3D bubble geometries. Details of the VCVH method were not provided in this thesis and readers are redirected to Masuk et al. (2019) for more details. On the other hand, the second one is an open source Lagrangian particle tracking (openLPT) code that is based on the high-concentration particle tracking method called shake-the-box (Schanz, Gesemann, and Schröder, 2016). The details of this code, including its speed and performance on the synthetic and experimental data are provided in chapter 3. Using openLPT, we could simultaneously track about 7,000 tracer particles around the bubbles. These trajectories were later exploited to obtain the first and second order statistics such as the flow velocity, acceleration, and turbulence velocity gradients in addition to other derived statistics like the correlation and structure functions. On the other hand, the 3D locations of surface points on the reconstructed bubble geometry obtained from the VCVH code can be averaged to obtain the center of mass of the bubbles, which was tracked over time to construct their trajectories and eventually get their velocity and accelerations.

Looking back at equation 1.9 that governs the motion of air bubbles in turbulence, the aforementioned 3D measurements of both the phases, like the bubble geometries, Lagrangian velocity and accelerations of both the phases, and turbulent velocity gradients encompass all the variables that one would need to model the unclosed parameters of the interfacial momentum transfer such as the drag, lift and added-mass coefficients. However, the challenge in

extracting these coefficients is that they appear simultaneously in equation 1.9 and are coupled together. Therefore, in an attempt to decouple them, in chapter 4, we took an ensemble average of equation 1.9 that averaged the unsteady forces like the added-mass to zero. From this new equation, we then explored the drag and lift coefficients and modeled their dependence on the particle-based Reynolds number, $Re$ and turbulence Weber number, $We$ respectively. This was made possible by measuring the mean rise velocity of the bubbles in intense turbulence that showed a surprising trend as a function of the bubble sizes, which was never observed before. When compared to the rise velocity in quiescent medium, the new trend showed that with increasing bubble size, the rise velocity in turbulence changes from an order of magnitude slower for small bubbles to more than double the quiescent rise velocities for large bubbles. Thereafter, based on the mean vertical velocity of the flow surrounding the bubbles, the reason for this surprising behaviour was explained as preferential sampling, where small bubbles drift towards the downward flow side and large bubbles move towards upward flow side of an eddy. Later on, utilizing the bubble-eddy collision model, the hydrodynamic forces acting on the bubble were separated into the horizontal and vertical forces which decoupled the lift and drag coefficients and made it possible to model them.

Previous works like Tomiyama et al. (2002) showed that the transverse lift force acting on a deformable bubble in a mean shear flow exhibits a sign inver-

sion from a positive value for small spherical bubbles to a negative for large deformed bubbles. This inversion was related to the Eötvös number, $Eo$ which is a measure of the buoyancy induced bubble deformation. However, unlike the mean shear case, in our setup with intense turbulence, the fluctuations in the flow determine the bubble deformation. This turbulence induced deformation was measured by the Weber number, $We$ that is the ratio of deforming inertial force to resisting surface tension forces. Thereby, using the data from our experiments, we provided an empirical relation between the $C_L$ and $We$ in equation 4.8. Interestingly, we found that the lift inversion in our case occurred when $We$ gets close to one. On the other hand, the drag coefficient was also modified for large bubbles in turbulence, when compared to their quiescent counterpart. We speculate that this modification was due to the suppression of the wake behind large bubbles owing to turbulence fluctuations. In equation 4.9, we accounted for this change and presented an updated relation between relation among $C_D$, $Re_b$, $Eo$, and $We$.

The added-mass is an unsteady force that comes into play when a particle is accelerating relative to the surrounding flow and consequently exchanges energy in order to accelerate or decelerate the flow around it. After determining the closure models for the lift and drag coefficients from the mean vertical velocity of the bubbles and their surrounding flows, the only unclosed term in equation 1.9 is the added-mass coefficient. However, reliable estimation of the

added-mass requires an accurate estimation of the 3D bubble geometries, instantaneous accelerations of both the phases and turbulence velocity gradients, which pushes the Lagrangian 3D flow measurements to its extreme. Thankfully, the V-ONSET diagnostic system in conjunction with our in-house 3D reconstruction codes enabled the measurements of all these quantities. Eventually, we utilized these measurements and estimated the added-mass coefficient by matching the standard deviation of the bubble accelerations independently determined from two different methods, (i) the 3D Lagrangian trajectories of bubbles; and (ii) equation 1.9. Historically, the added-mass turned out to be sensitive to the bubble shape and orientation with respect to surrounding flows. Therefore, the added-mass coefficient determined from our experiments was plotted against the bubble aspect ratio and was found to reduce with increasing aspect ratio. Such a behaviour was previously observed for spheroidal bubbles (both prolate and oblate) preferentially accelerating along their semi-major axis (called end-on configuration). On further investigating the orientation of the bubbles with their relative acceleration, we found that the bubbles in our setup indeed accelerated preferentially along their semi-major axis. Moreover, despite the fact that the bubbles are deforming significantly due to turbulent fluctuations, the measured coefficient shows a good agreement with the analytical solution provided by Clift, Grace, and Weber (2005) for spheroids accelerating in a potential flow with an end-on configuration.

In chapter 6, we investigated the mass transfer rate of two miscible liquids driven by dissolution convection in a porous medium, where the momentum terms can be typically ignored. Such a convective mixing mechanism is characterized by plumes (or fingers) that originates from the instabilities at the liquid-liquid interface and slowly move downwards, thereby carrying the lighter liquid at the top into the heavier liquid at the bottom. According to previous studies, the mass transfer rate between the two liquids was found to be a function of the total number of fingers that carry the lighter fluid and their downward velocities. However, most prior studies in this field were focused on determining the mixing efficiency in homogeneous systems. Note that, the current study was motivated by the geological sequestration of $CO_2$ in underground saline aquifers which are usually riddled with multiple layers of alternating high and low permeabilities that can act as flow barriers and significantly reduce the mixing efficiency. Therefore, we naturally examined the dependence of dimensionless mass transfer rate called the Sherwood number ($Sh$) on the layered heterogeneity of the porous medium. This was achieved by placing a single layer of latex circular discs in a 2D Hele-Shaw cell. Additionally, since the two fluids were density mismatched, we used the shadowgraph technique to identify that interface between the two fluids and eventually quantify their mixing rate. Our results showed that the presence of these low permeability barriers in an otherwise homogeneous significantly

affected the mixing rate. A mere 10% reduction in bulk permeability can reduce the mixing efficiency by as much as 80%. Subsequently, we developed a physics based model that can explain this reduction by identifying their dependence on the flow length scales; finger width, $\delta$ and finger spacing, $\lambda$. Their ratio, $\delta/\lambda$ determines the number of fingers that can pass through the low permeability barrier. In addition, another non-dimensional parameter called the effective Rayleigh number, $Ra_{eff}$ was introduced to account for the effect of the disc layer on the plume velocities. Based on the experimental data, this non-dimensional plume velocity was found to have an exponential dependence on the ratio between the imposed length scale, i.e the disc spacing ($l$) and the flow length scale ($\delta$). Henceforth, the two parameters were put together in equations 6.4 and 6.5 in order to effectively connect the mass transfer rate, $Sh$ to the measurable heterogeneity properties of the medium.

In summary, this thesis has independently explored the interfacial mass and momentum transfer across deformable interfaces in two-phase flows. Moreover, we provided closure models constrained by experimental data to (i) predict the trajectories of gas bubbles rising in turbulent water, and (ii) examine the mass transfer rate between two liquids in heterogeneous porous medium. Nevertheless, many issues still remain unexplored that could be potentially investigated using the current experimental data. Some of them are listed here.

The simultaneous 3D Lagrangian data of both phases acquired from the ex-

periments conducted in the V-ONSET provides a unique framework to study many problems related to bubble-turbulence interactions. Pair dispersion is one such problem that has attracted a lot of attention in the past due to its importance in understanding the mixing and transport of particles in turbulent medium. The high-concentration 3D trajectories of tracer particles can be potentially used to study the dispersion between pairs of particles and subsequently shed light on the mixing phenomena in intense turbulent environments. Furthermore, although many previous works studied the dispersion between two inertial particles in isotropic turbulence (Salazar and Collins, 2009), very limited research is available on the dispersion of buoyant particles like bubbles. Therefore, with the help of 3D bubble trajectories in conjunction with 3D particle tracks, one can also study the bubble-bubble and bubble-particle pair dispersion in turbulence.

The mean energy dissipation rate in the V-ONSET setup was close to 0.16 $m^2/s^3$ for single-phase turbulence (Masuk et al., 2019). By injecting just 2% volume fraction of poly-dispersed bubbles into this system, its energy dissipation rate increased by more than 200% to 0.52 $m^2/s^3$. This increase in energy is attributed to the bubble-induced pseudo-turbulence. Therefore, by the means of surrounding flow information close to bubbles, one can investigate this pseudo-turbulence introduced by finite-sized deformable bubbles rising in an otherwise turbulent water. Additionally, this experimental data can also be used to study

other turbulent two-phase phenomena such as, (i) the temporal evolution of bubble shapes due to their complex interaction with surrounding turbulent structures, (ii) the underlying physics behind bubble breakup and coalescence in turbulence, and also (iii) the dynamics of bubble-bubble collisions.

Moreover, the OpenLPT code discussed in chapter 3 is available for public use at Tan (2020 (accessed June 10, 2020)). It is the first open-source code based on the STB algorithm. The code has been parallelized to run on high performance clusters that can significantly speed up the data processing. We hope that this code can be potentially used in the future for algorithm development, data assimilation, and uncertainty analysis.

# References

Rüdisüli, Martin, Tilman J Schildhauer, Serge MA Biollaz, and J Ruud van Ommen (2012). “Scale-up of bubbling fluidized bed reactors—A review”. In: *Powder Technology* 217, pp. 21–38.

Besagni, Giorgio, Fabio Inzoli, and Thomas Ziegenhein (2018). “Two-phase bubble columns: A comprehensive review”. In: *ChemEngineering* 2.2, p. 13.

Merritt, Wendy S, Rebecca A Letcher, and Anthony J Jakeman (2003). “A review of erosion and sediment transport models”. In: *Environmental Modelling & Software* 18.8-9, pp. 761–799.

Gong, Yanyan, Xiao Zhao, Zhengqing Cai, SE O’reilly, Xiaodi Hao, and Dongye Zhao (2014). “A review of oil, dispersed oil and sediment interactions in the aquatic environment: influence on the fate, transport and remediation of oil spills”. In: *Marine pollution bulletin* 79.1-2, pp. 16–33.

Ishii, M and K Mishima (1984). “Two-fluid model and hydrodynamic constitutive relations”. In: *Nuclear Engineering and design* 82.2-3, pp. 107–126.

REFERENCES

Enwald, Hans, Eric Peirano, and A-E Almstedt (1996). “Eulerian two-phase flow theory applied to fluidization”. In: *International Journal of Multiphase Flow* 22, pp. 21–66.

Magnaudet, J and I Eames (2000). “The motion of high-Reynolds-number bubbles in inhomogeneous flows”. In: *Annual Review of Fluid Mechanics* 32.1, pp. 659–708.

Poorte, REG and A Biesheuvel (2002). “Experiments on the motion of gas bubbles in turbulence generated by an active grid”. In: *Journal of Fluid Mechanics* 461, pp. 127–154.

Prakash, VN, Y Tagawa, E Calzavarini, J Mercado, Federico Toschi, D Lohse, and C Sun (2012). “How gravity and size affect the acceleration statistics of bubbles in turbulence”. In: *New journal of physics* 14.10, p. 105017.

Lu, J and G Tryggvason (2013). “Dynamics of nearly spherical bubbles in a turbulent channel upflow”. In: *Journal of Fluid Mechanics* 732, pp. 166–189.

Loisy, A and A Naso (2017). “Interaction between a large buoyant bubble and turbulence”. In: *Physical Review Fluids* 2.1, p. 014606.

Riaz, A, M Hesse, HA Tchelepi, and FM Orr (2006). “Onset of convection in a gravitationally unstable diffusive boundary layer in porous media”. In: *Journal of Fluid Mechanics* 548.1, pp. 87–111.

REFERENCES

Riaz, Amir and Yildiray Cinar (2014). “Carbon dioxide sequestration in saline formations: Part IâReview of the modeling of solubility trapping”. In: *Journal of Petroleum Science and Engineering* 124, pp. 367–380.

Farajzadeh, Rouhollah, Panneer Ranganathan, Pacelli Lidio Jose Zitha, and Johannes Bruining (2011). “The effect of heterogeneity on the character of density-driven natural convection of CO 2 overlying a brine layer”. In: *Advances in Water Resources* 34.3, pp. 327–339.

Agartan, Elif, Luca Trevisan, Abdullah Cihan, Jens Birkholzer, Quanlin Zhou, and Tissa H Illangasekare (2015). “Experimental study on effects of geologic heterogeneity in enhancing dissolution trapping of supercritical CO2”. In: *Water Resources Research* 51.3, pp. 1635–1648.

Masuk, Ashik Ullah Mohammad, Ashwanth Salibindla, and Rui Ni (2019). “A robust virtual-camera 3D shape reconstruction of deforming bubbles/droplets with additional physical constraints”. In: *International Journal of Multiphase Flow*, p. 103088.

Tan, S, A Salibindla, AUM Masuk, and R Ni (2020a). “Introducing OpenLPT: new method of removing ghost particles and high-concentration particle shadow tracking”. In: *Experiments in Fluids* 61.2, p. 47. ISSN: 0723-4864. DOI: 10.1007/s00348-019-2875-2.

Tan, Shiyong, Ashwanth Salibindla, Ashik Ullah Mohammad Masuk, and Rui Ni (2020b). “Introducing OpenLPT: new method of removing ghost parti-

cles and high-concentration particle shadow tracking". In: *Experiments in Fluids* 61.2, p. 47.

Schanz, Daniel, Sebastian Gesemann, and Andreas Schröder (2016). "Shake-The-Box: Lagrangian particle tracking at high particle image densities". In: *Experiments in fluids* 57.5, p. 70.

Wyngaard, John C (2010). *Turbulence in the Atmosphere*. Cambridge University Press.

Deane, GB and MD Stokes (2002). "Scale dependence of bubble creation mechanisms in breaking waves". In: *Nature* 418.6900, p. 839.

Launder, BE (1991). "Current capabilities for modelling turbulence in industrial flows". In: *Applied Scientific Research* 48.3-4, pp. 247–269.

Michiyoshi, Itaru and Akimi Serizawa (1986). "Turbulence in two-phase bubbly flow". In: *Nuclear Engineering and design* 95, pp. 253–267.

Jakobsen, Hugo A (2008). "Chemical reactor modeling". In: *Multiphase Reactive Flows*.

Gils, Dennis PM van, Gert-Wim Bruggert, Daniel P Lathrop, Chao Sun, and Detlef Lohse (2011). "The Twente turbulent Taylor–Couette (T3C) facility: strongly turbulent (multiphase) flow between two independently rotating cylinders". In: *Review of scientific instruments* 82.2, p. 025105.

Anantharaman, Arjun (2019). "Suspension Taylor-Couette flow: Investigation of particle loading effects on transitions between flow regimes". In:

REFERENCES

Murai, Y, H Oiwa, and Y Takeda (2005). “Bubble behavior in a vertical Taylor-Couette flow”. In: *Journal of Physics: conference series*. Vol. 14. 1. IOP Publishing, p. 143.

Verschoof, Ruben A., Roeland C. A. van der Veen, Chao Sun, and Detlef Lohse (2016). “Bubble Drag Reduction Requires Large Bubbles”. In: *Phys. Rev. Lett.* 117 (10), p. 104502. DOI: 10.1103/PhysRevLett.117.104502. URL: http://link.aps.org/doi/10.1103/PhysRevLett.117.104502.

Ravelet, Florent, Rene Delfos, and Jerry Westerweel (2010). “Influence of global rotation and Reynolds number on the large-scale features of a turbulent Taylor–Couette flow”. In: *Physics of Fluids* 22.5, p. 055103.

Mehel, Amine, Celine Gabillet, and Henda Djeridi (2006). “Bubble effect on the structures of weakly turbulent Couette Taylor flow”. In:

Gils, Dennis P. M. van, Daniela Narezo Guzman, Chao Sun, and Detlef Lohse (2013). “The importance of bubble deformability for strong drag reduction in bubbly turbulent Taylor–Couette flow”. In: *Journal of Fluid Mechanics* 722, pp. 317–347. ISSN: 1469-7645. DOI: 10.1017/jfm.2013.96. URL: http://journals.cambridge.org/article_S0022112013000967.

Bakhuis, Dennis, Ruben A. Verschoof, Varghese Mathai, Sander G. Huisman, Detlef Lohse, and Chao Sun (2018). “Finite-sized rigid spheres in turbulent Taylor–Couette flow: effect on the overall drag”. In: *Journal of Fluid Mechanics* 850, 246–261. DOI: 10.1017/jfm.2018.462.

Verschoof, Ruben A., Dennis Bakhuis, Pim A. Bullee, Sander G. Huisman, Chao Sun, and Detlef Lohse (2018). “The influence of wall roughness on bubble drag reduction in Taylor–Couette turbulence”. In: *Journal of Fluid Mechanics* 851, 436–446. DOI: 10.1017/jfm.2018.515.

Bullee, Pim A., Ruben A. Verschoof, Dennis Bakhuis, Sander G. Huisman, Chao Sun, Rob G. H. Lammertink, and Detlef Lohse (2020). “Bubbly drag reduction using a hydrophobic inner cylinder in Taylor–Couette turbulence”. In: *Journal of Fluid Mechanics* 883, A61. DOI: 10.1017/jfm.2019.894.

Bakhuis, Dennis, Varghese Mathai, Ruben A. Verschoof, Rodrigo Ezeta, Detlef Lohse, Sander G. Huisman, and Chao Sun (2019). “Statistics of rigid fibers in strongly sheared turbulence”. In: *Phys. Rev. Fluids* 4 (7), p. 072301. DOI: 10.1103/PhysRevFluids.4.072301. URL: https://link.aps.org/doi/10.1103/PhysRevFluids.4.072301.

Wang, Lian-Ping and Martin R Maxey (1993b). “The motion of microbubbles in a forced isotropic and homogeneous turbulence”. In: *Applied Scientific Research* 51.1-2, pp. 291–296.

Aliseda, A and JC Lasheras (2011). “Preferential concentration and rise velocity reduction of bubbles immersed in a homogeneous and isotropic turbulent flow”. In: *Physics of Fluids* 23.9, p. 093301.

Wang, Lian-Ping and Martin R Maxey (1993a). “Settling velocity and concentration distribution of heavy particles in homogeneous isotropic turbulence”. In: *Journal of fluid mechanics* 256, pp. 27–68.

Aliseda, A, Alain Cartellier, F Hainaux, and Juan C Lasheras (2002). “Effect of preferential concentration on the settling velocity of heavy particles in homogeneous isotropic turbulence”. In: *Journal of Fluid Mechanics* 468, pp. 77–105.

Yang, TS and SS Shy (2003). “The settling velocity of heavy particles in an aqueous near-isotropic turbulence”. In: *Physics of fluids* 15.4, pp. 868–880.

La Porta, Arthur, Greg A Voth, Alice M Crawford, Jim Alexander, and Eberhard Bodenschatz (2001). “Fluid particle accelerations in fully developed turbulence”. In: *Nature* 409.6823, pp. 1017–1019.

Voth, Greg A, Arthur la Porta, Alice M Crawford, Jim Alexander, and Eberhard Bodenschatz (2002). “Measurement of particle accelerations in fully developed turbulence”. In: *Journal of Fluid Mechanics* 469, pp. 121–160.

Calzavarini, Enrico, Romain Volk, Mickaël Bourgoin, Emmanuel Lévêque, J-F Pinton, and Federico Toschi (2009). “Acceleration statistics of finite-sized particles in turbulent flow: the role of Faxén forces”. In: *Journal of Fluid Mechanics* 630, pp. 179–189.

Squires, Kyle D and John K Eaton (1991). “Preferential concentration of particles by turbulence”. In: *Physics of Fluids A: Fluid Dynamics* 3.5, pp. 1169–1178.

Wood, AM, W Hwang, and JK Eaton (2005). “Preferential concentration of particles in homogeneous and isotropic turbulence”. In: *International journal of multiphase flow* 31.10-11, pp. 1220–1230.

Villermaux, E, B Sixou, and Y Gagne (1995). “Intense vortical structures in grid-generated turbulence”. In: *Physics of fluids* 7.8, pp. 2008–2013.

Mercado, Julian Martinez, Vivek N Prakash, Yoshiyuki Tagawa, Chao Sun, Detlef Lohse, and (International Collaboration for Turbulence Research) (2012). “Lagrangian statistics of light particles in turbulence”. In: *Physics of fluids* 24.5, p. 055106.

Zimmermann, Robert, Haitao Xu, Yoann Gasteuil, Mickaël Bourgoin, Romain Volk, Jean-François Pinton, Eberhard Bodenschatz, et al. (2010). “The Lagrangian exploration module: An apparatus for the study of statistically homogeneous and isotropic turbulence”. In: *Review of Scientific Instruments* 81.5, p. 055112.

Frisch, Uriel (1995). *Turbulence: the legacy of AN Kolmogorov*. Cambridge university press.

Kolmogorov, A (1949). “On the breakage of drops in a turbulent flow”. In: *Dokl. Akad. Navk. SSSR*. Vol. 66, pp. 825–828.

REFERENCES

Variano, Evan A and Edwin A Cowen (2008). “A random-jet-stirred turbulence tank”. In: *Journal of Fluid Mechanics* 604, pp. 1–32.

Bellani, Gabriele and Evan A Variano (2014). “Homogeneity and isotropy in a laboratory turbulent flow”. In: *Experiments in fluids* 55.1, pp. 1–12.

Masuk, AUM, A Salibindla, S Tan, and R Ni (2019). “V-ONSET (Vertical Octagonal Noncorrosive Stirred Energetic Turbulence): A vertical water tunnel with a large energy dissipation rate to study bubble/droplet deformation and breakup in strong turbulence”. In: *Review of Scientific Instruments* 90.8, p. 085105.

Pérez-Alvarado, Alejandro, Laurent Mydlarski, and Susan Gaskin (2016). “Effect of the driving algorithm on the turbulence generated by a random jet array”. In: *Experiments in Fluids* 57.2, p. 20.

Miller, N and RE Mitchie (1970). *Measurement of local voidage in liquid/gas two-phase flow systems using a universal probe.* Tech. rep. Atomic Power Constructions Ltd., Heston, Eng.

Li, Xiangyang, Chao Yang, Shifang Yang, and Guozheng Li (2012). “Fiber-optical sensors: basics and applications in multiphase reactors”. In: *Sensors* 12.9, pp. 12519–12544.

Hagemeier, Thomas, Matthias Börner, Andreas Bück, and Evangelos Tsotsas (2015). “A comparative study on optical techniques for the estimation of granular flow velocities”. In: *Chemical Engineering Science* 131, pp. 63–75.

Prakash, Baranivignesh, Harisinh Parmar, Milinkumar T Shah, Vishnu K Pareek, Lefebvre Anthony, and Ranjeet P Utikar (2019). “Simultaneous measurements of two phases using an optical probe”. In: *Experimental and Computational Multiphase Flow* 1.4, pp. 233–241.

Westerweel, Jerry, Gerrit E Elsinga, and Ronald J Adrian (2013). “Particle image velocimetry for complex and turbulent flows”. In: *Annual Review of Fluid Mechanics* 45, pp. 409–436.

Zhou, Xinquan, Benjamin Doup, and Xiaodong Sun (2013). “Measurements of liquid-phase turbulence in gas–liquid two-phase flows using particle image velocimetry”. In: *Measurement Science and Technology* 24.12, p. 125303.

Charogiannis, Alexandros, Jae Sik An, and Christos N Markides (2015). “A simultaneous planar laser-induced fluorescence, particle image velocimetry and particle tracking velocimetry technique for the investigation of thin liquid-film flows”. In: *Experimental Thermal and Fluid Science* 68, pp. 516–536.

Hu, H, T Kobayashi, T Saga, S Segawa, and N Taniguchi (2000). “Particle image velocimetry and planar laser-induced fluorescence measurements on lobed jet mixing flows”. In: *Experiments in fluids* 29.1, S141–S157.

Ibarra, Roberto, Ivan Zadrazil, Omar K Matar, and Christos N Markides (2018). “Dynamics of liquid–liquid flows in horizontal pipes using simultaneous

two–line planar laser–induced fluorescence and particle velocimetry". In: *International Journal of Multiphase Flow* 101, pp. 47–63.

Law, Adrian Wing-Keung and Hongwei Wang (2000). "Measurement of mixing processes with combined digital particle image velocimetry and planar laser induced fluorescence". In: *Experimental thermal and fluid science* 22.3-4, pp. 213–229.

Hessenkemper, H and T Ziegenhein (2018). "Particle Shadow Velocimetry (PSV) in bubbly flows". In: *International Journal of Multiphase Flow* 106, pp. 268–279.

Sathe, Mayur J, Iqbal H Thaker, Tyson E Strand, and Jyeshtharaj B Joshi (2010). "Advanced PIV/LIF and shadowgraphy system to visualize flow structure in two-phase bubbly flows". In: *Chemical Engineering Science* 65.8, pp. 2431–2442.

Bröder, D and M Sommerfeld (2007). "Planar shadow image velocimetry for the analysis of the hydrodynamics in bubbly flows". In: *Measurement Science and Technology* 18.8, p. 2513.

Ziegenhein, Thomas, Dirk Lucas, Giorgio Besagni, and Fabio Inzoli (2020). "Experimental study of the liquid velocity and turbulence in a large-scale air-water counter-current bubble column". In: *Experimental Thermal and Fluid Science* 111, p. 109955.

REFERENCES

Lindken, R and W Merzkirch (2002). “A novel PIV technique for measurements in multiphase flows and its application to two-phase bubbly flows”. In: *Experiments in fluids* 33.6, pp. 814–825.

Poelma, Christian (2020). “Measurement in opaque flows: a review of measurement techniques for dispersed multiphase flows”. In:

Poelma, C, J Westerweel, and G Ooms (2006). “Turbulence statistics from optical whole-field measurements in particle-laden turbulence”. In: *Experiments in Fluids* 40.3, pp. 347–363.

Ziegenhein, Thomas and Dirk Lucas (2016). “On sampling bias in multiphase flows: Particle image velocimetry in bubbly flows”. In: *Flow Measurement and Instrumentation* 48, pp. 36–41.

Voulgaropoulos, Victor and Panagiota Angeli (2017). “Optical measurements in evolving dispersed pipe flows”. In: *Experiments in Fluids* 58.12, p. 170.

Katz, Joseph and Jian Sheng (2010). “Applications of holography in fluid mechanics and particle dynamics”. In: *Annual Review of Fluid Mechanics* 42, pp. 531–555.

Truscott, Tadd T, Jesse Belden, Rui Ni, Jonathon Pendlebury, and Bryce McEwen (2017). “Three-dimensional microscopic light field particle image velocimetry”. In: *Experiments in Fluids* 58.3, p. 16.

Angeli, P and GF Hewitt (2000). “Flow structure in horizontal oil–water flow”. In: *International journal of multiphase flow* 26.7, pp. 1117–1140.

REFERENCES

Nasr-El-Din, H, CA Shook, and J Colwell (1987). “A conductivity probe for measuring local concentrations in slurry systems”. In: *International journal of multiphase flow* 13.3, pp. 365–378.

Costigan, G and PB Whalley (1997). “Slug flow regime identification from dynamic void fraction measurements in vertical air-water flows”. In: *International Journal of Multiphase Flow* 23.2, pp. 263–282.

Paglianti, A and S Pintus (2001). “An impedance probe for the measurements of liquid hold-up and mixing time in two/three-phase stirred tank reactors”. In: *Experiments in fluids* 31.4, pp. 417–427.

Abouelwafa, M Sami A and E John M Kendall (1980). “The use of capacitance sensors for phase percentage determination in multiphase pipelines”. In: *IEEE transactions on Instrumentation and Measurement* 29.1, pp. 24–27.

Strizzolo, Cristina N and Jose Converti (1993). “Capacitance sensors for measurement of phase volume fraction in two-phase pipelines”. In: *IEEE Transactions on instrumentation and measurement* 42.3, pp. 726–729.

Jaworek, A, A Krupa, and M Trela (2004). “Capacitance sensor for void fraction measurement in water/steam flows”. In: *Flow Measurement and Instrumentation* 15.5-6, pp. 317–324.

Strazza, Domenico, Marco Demori, Vittorio Ferrari, and Pietro Poesio (2011). “Capacitance sensor for hold-up measurement in high-viscous-oil/conductive-

water core-annular flows". In: *Flow Measurement and Instrumentation* 22.5, pp. 360–369.

Le Corre, J-M, E Hervieu, M Ishii, and J-M Delhaye (2003). "Benchmarking and improvements of measurement techniques for local-time-averaged two-phase flow parameters". In: *Experiments in fluids* 35.5, pp. 448–458.

Kataoka, Isao, Mamoru Ishii, and Akimi Serizawa (1986). "Local formulation and measurements of interfacial area concentration in two-phase flow". In: *International Journal of Multiphase Flow* 12.4, pp. 505–529.

Revankar, ST and M Ishii (1992). "Local interfacial area measurement in bubbly flow". In: *International journal of heat and mass transfer* 35.4, pp. 913–925.

Wu, Q and M Ishii (1999). "Sensitivity study on double-sensor conductivity probe for the measurement of interfacial area concentration in bubbly flow". In: *International Journal of Multiphase Flow* 25.1, pp. 155–173.

Jin, ND, Z Xin, Jun Wang, ZY Wang, XH Jia, and WP Chen (2008). "Design and geometry optimization of a conductivity probe with a vertical multiple electrode array for measuring volume fraction and axial velocity of two-phase flow". In: *Measurement science and technology* 19.4, p. 045403.

Manera, Annalisa, Basar Ozar, Sidharth Paranjape, Mamoru Ishii, and H-M Prasser (2009). "Comparison between wire-mesh sensors and conductive

needle-probes for measurements of two-phase flow parameters". In: *Nuclear Engineering and Design* 239.9, pp. 1718–1724.

Tan, Chao, Pengfei Li, Wei Dai, and Feng Dong (2015). "Characterization of oil–water two-phase pipe flow with a combined conductivity/capacitance sensor and wavelet analysis". In: *Chemical Engineering Science* 134, pp. 153–168.

Kim, Seungjin, XY Fu, X Wang, and M Ishii (2000). "Development of the miniaturized four-sensor conductivity probe and the signal processing scheme". In: *International journal of heat and mass transfer* 43.22, pp. 4101–4118.

Da Silva, MJ, S Thiele, L Abdulkareem, BJ Azzopardi, and U Hampel (2010). "High-resolution gas–oil two-phase flow visualization with a capacitance wire-mesh sensor". In: *Flow Measurement and Instrumentation* 21.3, pp. 191–197.

Da Silva, MJ, EN Dos Santos, U Hampel, IH Rodriguez, and OMH Rodriguez (2011). "Phase fraction distribution measurement of oil–water flow using a capacitance wire-mesh sensor". In: *Measurement Science and Technology* 22.10, p. 104020.

Barnea, Dvora, Elena Roitberg, and Lev Shemer (2013). "Spatial distribution of void fraction in the liquid slug in the whole range of pipe Inclinations". In: *International Journal of Multiphase Flow* 52, pp. 92–101.

Abdulkadir, M, V Hernandez-Perez, IS Lowndes, BJ Azzopardi, and ET Brantson (2014). "Detailed analysis of phase distributions in a vertical riser using

wire mesh sensor (WMS)". In: *Experimental thermal and fluid science* 59, pp. 32–42.

Ito, D, H-M Prasser, H Kikura, and M Aritomi (2011). "Uncertainty and intrusiveness of three-layer wire-mesh sensor". In: *Flow Measurement and Instrumentation* 22.4, pp. 249–256.

Peña, HF Velasco and OMH Rodriguez (2015). "Applications of wire-mesh sensors in multiphase flows". In: *Flow measurement and instrumentation* 45, pp. 255–273.

Schubert, Markus, Abhishek Khetan, Marco Jose Da Silva, and Holger Kryk (2010). "Spatially resolved inline measurement of liquid velocity in trickle bed reactors". In: *Chemical Engineering Journal* 158.3, pp. 623–632.

Hoppe, Dietrich, Alexander Grahn, and Peter Schütz (2010). "Determination of velocity and angular displacement of bubbly flows by means of wire-mesh sensors and correlation analysis". In: *Flow Measurement and Instrumentation* 21.1, pp. 48–53.

Tompkins, Casey, Horst-Michael Prasser, and Michael Corradini (2018). "Wire-mesh sensors: A review of methods and uncertainty in multiphase flows relative to other measurement techniques". In: *Nuclear Engineering and Design* 337, pp. 205–220.

REFERENCES

Dudlik, A, H-M Prasser, A Apostolidis, and A Bergant (2008). “Water hammer induced by fast-acting valves: Experimental studies at pilot plant pipework”. In: *Multiphase Science and Technology* 20.3-4.

Silva, Marco Jose da, Eckhard Schleicher, and Uwe Hampel (2009). “Advanced wire-mesh sensor technology for fast flow imaging”. In: *2009 IEEE International Workshop on Imaging Systems and Techniques*. IEEE, pp. 253–257.

Warsito, Warsito, Qussai Marashdeh, and Liang-Shih Fan (2007). “Electrical capacitance volume tomography”. In: *IEEE sensors journal* 7.4, pp. 525–535.

Saoud, A, V Mosorov, and K Grudzien (2017). “Measurement of velocity of gas/solid swirl flow using Electrical Capacitance Tomography and cross correlation technique”. In: *Flow Measurement and Instrumentation* 53, pp. 133–140.

Chowdhury, Shah, Qussai M Marashdeh, and Fernando L Teixeira (2016). “Velocity profiling of multiphase flows using capacitive sensor sensitivity gradient”. In: *IEEE Sensors Journal* 16.23, pp. 8365–8373.

Heindel, Theodore J (2011). “A review of X-ray flow visualization with applications to multiphase flows”. In: *Journal of Fluids Engineering* 133.7.

Mudde, RF (2011). “Bubbles in a fluidized bed: A fast X-ray scanner”. In: *AIChE journal* 57.10, pp. 2684–2690.

REFERENCES

Lau, YM, U Hampel, and M Schubert (2018). “Ultrafast X-ray tomographic imaging of multiphase flow in bubble columns-Part 1: Image processing and reconstruction comparison”. In: *International Journal of Multiphase Flow* 104, pp. 258–271.

Lau, YM, F Möller, U Hampel, and M Schubert (2018). “Ultrafast X-ray tomographic imaging of multiphase flow in bubble columns–Part 2: Characterisation of bubbles in the dense regime”. In: *International Journal of Multiphase Flow* 104, pp. 272–285.

Hampel, U (2015). “X-ray computed tomography”. In: *Industrial Tomography*. Elsevier, pp. 175–196.

Kastengren, Alan and Christopher F Powell (2014). “Synchrotron X-ray techniques for fluid dynamics”. In: *Experiments in fluids* 55.3, p. 1686.

Elkins, Christopher J and Marcus T Alley (2007). “Magnetic resonance velocimetry: applications of magnetic resonance imaging in the measurement of fluid motion”. In: *Experiments in Fluids* 43.6, pp. 823–858.

Bonn, Daniel, Stephane Rodts, Maarten Groenink, Salima Rafai, Noushine Shahidzadeh-Bonn, and Philippe Coussot (2008). “Some applications of magnetic resonance imaging in fluid mechanics: complex flows and complex fluids”. In: *Annu. Rev. Fluid Mech.* 40, pp. 209–233.

REFERENCES

Adrian, Ronald J (1984). “Scattering particle characteristics and their effect on pulsed laser measurements of fluid flow: speckle velocimetry vs particle image velocimetry”. In: *Applied optics* 23.11, pp. 1690–1691.

Papantoniou, D. and T. Dracos (1989). “Analyzing 3-D Turbulent Motions in Open Channel Flow by Use of Stereoscopy and Particle Tracking”. In: *Advances in Turbulence 2*. Ed. by Hans-Hermann Fernholz and Heinrich E. Fiedler. Berlin, Heidelberg: Springer Berlin Heidelberg, pp. 278–285. ISBN: 978-3-642-83822-4.

Nishino, Koichi, Nobuhide Kasagi, Masaru Hirata, and Yutaka Sata (1989). “Three-dimensional flow velocimetry based on digital image processing”. In: *Nippon Kikai Gakkai Ronbunshu, B Hen / Transactions of the Japan Society of Mechanical Engineers, Part B* 55.510, pp. 404–412.

Chiu, Wan-Cheng and Louis N Rib (1956). “The rate of dissipation of energy and the energy spectrum in a low-speed turbulent jet”. In: *Eos, Transactions American Geophysical Union* 37.1, pp. 13–26.

Sheu, Y-HE, TPK Chang, Gary B Tatterson, and DS Dickey (1982). “A three-dimensional measurement technique for turbulent flows”. In: *Chemical Engineering Communications* 17.1-6, pp. 67–83.

Chang, Thomas P, Neal A Wilcox, and Gary B Tatterson (1984). “Application of image processing to the analysis of three-dimensional flow fields”. In: *Optical Engineering* 23.3, pp. 283–0.

REFERENCES

Adamczyk, AA and L Rimai (1988). “Reconstruction of a 3-dimensional flow field from orthogonal views of seed track video images”. In: *Experiments in Fluids* 6.6, pp. 380–386.

Maas, HG, A Gruen, and D Papantoniou (1993). “Particle tracking velocimetry in three-dimensional flows”. In: *Experiments in Fluids* 15.2, pp. 133–146.

Malik, NA, Th Dracos, and DA Papantoniou (1993). “Particle tracking velocimetry in three-dimensional flows”. In: *Experiments in Fluids* 15.4-5, pp. 279–294.

Ouellette, Nicholas T, Haitao Xu, and Eberhard Bodenschatz (2006). “A quantitative study of three-dimensional Lagrangian particle tracking algorithms”. In: *Experiments in Fluids* 40.2, pp. 301–313.

Ni, Rui, Shi-Di Huang, and Ke-Qing Xia (2011). “Local energy dissipation rate balances local heat flux in the center of turbulent thermal convection”. In: *Physical review letters* 107.17, p. 174503.

Shen, Jikang and Rui Ni (2017). “Experimental investigation of clogging dynamics in homogeneous porous medium”. In: *Water Resources Research* 53.3, pp. 1879–1890.

Ni, Rui, James G Puckett, Eric R Dufresne, and Nicholas T Ouellette (2015b). “Intrinsic fluctuations and driven response of insect swarms”. In: *Physical review letters* 115.11, p. 118104.

REFERENCES

Hoyer, Klaus, Markus Holzner, Beat Lüthi, Michele Guala, Alexander Liberzon, and Wolfgang Kinzelbach (2005). “3D scanning particle tracking velocimetry”. In: *Experiments in Fluids* 39.5, pp. 923–934.

Ni, Rui, Stefan Kramel, Nicholas T Ouellette, and Greg A Voth (2015a). “Measurements of the coupling between the tumbling of rods and the velocity gradient tensor in turbulence”. In: *Journal of Fluid Mechanics* 766, pp. 202–225.

Kähler, Christian J, Tommaso Astarita, Pavlos P Vlachos, Jun Sakakibara, Rainer Hain, Stefano Discetti, Roderick La Foy, and Christian Cierpka (2016). “Main results of the 4th International PIV Challenge”. In: *Experiments in Fluids* 57.6, p. 97.

Elsinga, Gerrit E, Fulvio Scarano, Bernhard Wieneke, and Bas W van Oudheusden (2006). “Tomographic particle image velocimetry”. In: *Experiments in fluids* 41.6, pp. 933–947.

Wieneke, Bernhard (2012). “Iterative reconstruction of volumetric particle distribution”. In: *Measurement Science and Technology* 24.2, p. 024008.

Schneiders, Jan FG and Fulvio Scarano (2016). “Dense velocity reconstruction from tomographic PTV with material derivatives”. In: *Experiments in fluids* 57.9, p. 139.

Schneiders, Jan FG, Fulvio Scarano, and Gerrit E Elsinga (2017). "Resolving vorticity and dissipation in a turbulent boundary layer by tomographic PTV and VIC+". In: *Experiments in Fluids* 58.4, p. 27.

Van Gent, PL, Dirk Michaelis, BW Van Oudheusden, P-É Weiss, Roeland de Kat, Angeliki Laskari, Young Jin Jeon, Laurent David, Daniel Schanz, Florian Huhn, et al. (2017). "Comparative assessment of pressure field reconstructions from particle image velocimetry measurements and Lagrangian particle tracking". In: *Experiments in Fluids* 58.4, p. 33.

Schlueter-Kuck, Kristy L and John O Dabiri (2017). "Coherent structure colouring: identification of coherent structures from sparse data using graph theory". In: *Journal of Fluid Mechanics* 811, pp. 468–486.

Novara, M, D Schanz, CJ Kähler, and A Schröder (2015). "Shake-The-Box for multi-pulse tomographic systems: towards high seeding density particle tracking in high speed flows". In: *11th international symposium on PIV–IV15. Santa Barbara, USA*, pp. 14–16.

Novara, Matteo, Daniel Schanz, Nico Reuther, Christian J Kähler, and Andreas Schröder (2016b). "Lagrangian 3D particle tracking in high-speed flows: Shake-The-Box for multi-pulse systems". In: *Experiments in Fluids* 57.8, p. 128.

Tan, Shiyong (2020 (accessed June 10, 2020)). *OpenLPT GitHub repository*. URL: `https://github.com/JHU-NI-LAB/OpenLPT_Shake-The-Boxs`.

REFERENCES

Proakis, John G and D Manolakis (2007). *Digital Signal Processing, 4th ed*.

Novara, M, D Schanz, S Gesemann, KP Lynch, and A Schröder (2016a). "Lagrangian 3D particle tracking for multi-pulse systems: performance assessment and application of Shake-The-Box". In: *18th international symposium on applications of laser techniques to fluid mechanics*, pp. 4–7.

Li, Yi, Eric Perlman, Minping Wan, Yunke Yang, Charles Meneveau, Randal Burns, Shiyi Chen, Alexander Szalay, and Gregory Eyink (2008). "A public turbulence database cluster and applications to study Lagrangian evolution of velocity increments in turbulence". In: *Journal of Turbulence* 9, N31.

Schanz, Daniel, Sebastian Gesemann, Andreas Schröder, Bernhard Wieneke, and Matteo Novara (2012). "Non-uniform optical transfer functions in particle imaging: calibration and application to tomographic reconstruction". In: *Measurement Science and Technology* 24.2, p. 024009.

Wieneke, B (2008). "Volume self-calibration for 3D particle image velocimetry". In: *Experiments in fluids* 45.4, pp. 549–556.

Tsai, Roger (1987). "A versatile camera calibration technique for high-accuracy 3D machine vision metrology using off-the-shelf TV cameras and lenses". In: *IEEE Journal on Robotics and Automation* 3.4, pp. 323–344.

She, Z, E Jackson, and S Orszag (1990). "Intermittent vortex structures in homogeneous isotropic turbulence". In: *Nature* 344.6263, p. 226.

REFERENCES

Mougin, G and J Magnaudet (2001). “Path instability of a rising bubble”. In: *Physical review letters* 88.1, p. 014502.

Ern, P, F Risso, D Fabre, and J Magnaudet (2012). “Wake-induced oscillatory paths of bodies freely rising or falling in fluids”. In: *Annual Review of Fluid Mechanics* 44, pp. 97–121.

Lohse, Detlef (2018). “Bubble puzzles: From fundamentals to applications”. In: *Physical review fluids* 3.11, p. 110504.

Mathai, Varghese, Detlef Lohse, and Chao Sun (2020). “Bubble and buoyant particle laden turbulent flows”. In: *Annu. Rev. Condens. Matter Phys* 11.

Kawase, Y and M Moo-Young (1990). “Mathematical models for design of bioreactors: Applications of: Kolmogoroff’s theory of isotropic turbulence”. In: *The Chemical Engineering Journal* 43.1, B19–B41.

Woolf, DK (1997). “Bubbles and their role in gas exchange”. In: *The sea surface and global change*.

Boettcher, EJ, J Fineberg, and DP Lathrop (2000). “Turbulence and wave breaking effects on air-water gas exchange”. In: *Physical Review Letters* 85.9, p. 2030.

Spelt, PDM and A Biesheuvel (1997). “On the motion of gas bubbles in homogeneous isotropic turbulence”. In: *Journal of Fluid Mechanics* 336, pp. 221–244.

Sridhar, G and J Katz (1995). “Drag and lift forces on microscopic bubbles entrained by a vortex”. In: *Physics of Fluids* 7.2, pp. 389–399.

Mazzitelli, IM, D Lohse, and F Toschi (2003). “On the relevance of the lift force in bubbly turbulence”. In: *Journal of Fluid Mechanics* 488, pp. 283–313.

Hinze, JO (1955). “Fundamentals of the hydrodynamic mechanism of splitting in dispersion processes”. In: *AIChE Journal* 1.3, pp. 289–295.

Tan, S, A Salibindla, AUM Masuk, and R Ni (2019). “An open-source Shake-the-Box method and its performance evaluation”. In: *13th International Symposium on Particle Image Velocimetry – ISPIV 2019*.

Liu, Z, Y Zheng, L Jia, and Q Zhang (2005). “Study of bubble induced flow structure using PIV”. In: *Chemical Engineering Science* 60.13, pp. 3537–3552.

Lewandowski, B, M Fertig, G Krekel, and M Ulbricht (2018). “Analysis of wake structures in bubbly flows using Particle Image Velocimetry (PIV)”. In: *7th European Young Engineers Conference Monograph, Warsaw University of Technology, Faculty of Chemical and Process Engineering, Warsaw*, pp. 367–375.

Risso, F (2018). “Agitation, mixing, and transfers induced by bubbles”. In: *Annual Review of Fluid Mechanics* 50, pp. 25–48.

Clift, R, JR Grace, and ME Weber (2005). *Bubbles, drops, and particles*. Courier Corporation.

REFERENCES

Tomiyama, A, H Tamai, I Zun, and S Hosokawa (2002). “Transverse migration of single bubbles in simple shear flows”. In: *Chemical Engineering Science* 57.11, pp. 1849–1858.

Dijkhuizen, W, M van Sint Annaland, and JAM Kuipers (2010). “Numerical and experimental investigation of the lift force on single bubbles”. In: *Chemical engineering science* 65.3, pp. 1274–1287.

Hessenkemper, H, T Ziegenhein, and D Lucas (2019). “Contamination effects on the lift force of ellipsoidal air bubbles rising in saline water solutions”. In: *Chemical Engineering Journal*. ISSN: 1385-8947.

Ziegenhein, T, A Tomiyama, and D Lucas (2018). “A new measuring concept to determine the lift force for distorted bubbles in low Morton number system: Results for air/water”. In: *International Journal of Multiphase Flow* 108, pp. 11–24.

Lu, J and G Tryggvason (2008). “Effect of bubble deformability in turbulent bubbly upflow in a vertical channel”. In: *Physics of Fluids* 20.4, p. 040701.

Dabiri, S, J Lu, and G Tryggvason (2013). “Transition between regimes of a vertical channel bubbly upflow due to bubble deformability”. In: *Physics of Fluids* 25.10, p. 102110.

Adoua, R, D Legendre, and J Magnaudet (2009). “Reversal of the lift force on an oblate bubble in a weakly viscous linear shear flow”. In: *Journal of Fluid Mechanics* 628, pp. 23–41.

REFERENCES

Hibiki, T and M Ishii (2007). “Lift force in bubbly flow systems”. In: *Chemical Engineering Science* 62.22, pp. 6457–6474.

Legendre, D and J Magnaudet (1998). “The lift force on a spherical bubble in a viscous linear shear flow”. In: *Journal of Fluid Mechanics* 368, pp. 81–126.

Tomiyama, A, I Kataoka, I Zun, and T Sakaguchi (1998). “Drag coefficients of single bubbles under normal and micro gravity conditions”. In: *JSME International Journal Series B Fluids and Thermal Engineering* 41.2, pp. 472–479.

Ishii, M and N Zuber (1979). “Drag coefficient and relative velocity in bubbly, droplet or particulate flows”. In: *AIChE journal* 25.5, pp. 843–855.

Ishii, M and TC Chawla (1979). “Local drag laws in dispersed two-phase flow”. In: *Nasa Sti/Recon Technical Report N* 80.

Loth, E (2008). “Quasi-steady shape and drag of deformable bubbles and drops”. In: *International Journal of Multiphase Flow* 34.6, pp. 523–546.

Lindt, JT (1972). “On the periodic nature of the drag on a rising bubble”. In: *Chemical Engineering Science* 27.10, pp. 1775–1781.

Brücker, C (1999). “Structure and dynamics of the wake of bubbles and its relevance for bubble interaction”. In: *Physics of fluids* 11.7, pp. 1781–1796.

Clift, R and WH Gauvin (1971). “Motion of particles in turbulent gas streams”. In: *British Chemical Engineering* 16.2-3, p. 229.

REFERENCES

Ishii, Mamoru and Takashi Hibiki (2010). *Thermo-fluid dynamics of two-phase flow*. Springer Science & Business Media.

Lamb, Horace (1924). *Hydrodynamics*. University Press.

Batchelor, CK and GK Batchelor (1967). *An introduction to fluid dynamics*. Cambridge university press.

Brennen, CE (1982). *A Review of Added Mass and Fluid Inertial Forces.* Tech. rep.

Newman, John Nicholas (1977). "Marine hydrodynamics. 1977". In: *Massachusetts Institute of Technology, Cambridge, Massachusetts). Google Scholar* 19.

Kendoush, Abdullah Abbas (2007). "The virtual mass of an oblate-ellipsoidal bubble". In: *Physics Letters A* 366.3, pp. 253–255.

Zuber, Novak (1964). "On the dispersed two-phase flow in the laminar flow regime". In: *Chemical Engineering Science* 19.11, pp. 897–917.

Sankaranarayanan, K, X Shan, IG Kevrekidis, and Sankaran Sundaresan (2002). "Analysis of drag and virtual mass forces in bubbly suspensions using an implicit formulation of the lattice Boltzmann method". In: *Journal of Fluid Mechanics* 452, pp. 61–96.

Kendoush, Abdullah Abbas, Abbas H Sulaymon, and Sawsan AM Mohammed (2007). "Experimental evaluation of the virtual mass of two solid spheres accelerating in fluids". In: *Experimental thermal and fluid science* 31.7, pp. 813–823.

REFERENCES

Pudasaini, Shiva P (2019). “A fully analytical model for virtual mass force in mixture flows”. In: *International Journal of Multiphase Flow* 113, pp. 142–152.

Ackermann, Norbert L and Anat Arbhabhirama (1964). “Viscous and boundary effects on virtual mass”. In: *Journal of the Engineering Mechanics Division* 90.4, pp. 123–130.

Simcik, M, MC Ruzicka, and J Drahoš (2008). “Computing the added mass of dispersed particles”. In: *Chemical engineering science* 63.18, pp. 4580–4595.

Ohl, CD, A Tijink, and Andrea Prosperetti (2003). “The added mass of an expanding bubble”. In: *Journal of fluid mechanics* 482, pp. 271–290.

Wakaba, L and S Balachandar (2007). “On the added mass force at finite Reynolds and acceleration numbers”. In: *Theoretical and Computational fluid dynamics* 21.2, pp. 147–153.

Magnaudet, Jacques, Mayela Rivero, and Jean Fabre (1995). “Accelerated flows past a rigid sphere or a spherical bubble. Part 1. Steady straining flow”. In: *Journal of fluid mechanics* 284, pp. 97–135.

Mougin, G and Jacques Magnaudet (2002). “The generalized Kirchhoff equations and their application to the interaction between a rigid body and an arbitrary time-dependent viscous flow”. In: *International journal of multiphase flow* 28.11, pp. 1837–1851.

REFERENCES

Mougin, Guillaume and Jacques Magnaudet (2006). “Wake-induced forces and torques on a zigzagging/spiralling bubble”. In: *Journal of Fluid Mechanics* 567, pp. 185–194.

De Vries, J, S Luther, and Detlef Lohse (2002). “Induced bubble shape oscillations and their impact on the rise velocity”. In: *The European Physical Journal B-Condensed Matter and Complex Systems* 29.3, pp. 503–509.

Cano-Lozano, José Carlos, Carlos Martinez-Bazan, Jacques Magnaudet, and Joël Tchoufag (2016). “Paths and wakes of deformable nearly spheroidal rising bubbles close to the transition to path instability”. In: *Physical Review Fluids* 1.5, p. 053604.

Lavrenteva, Olga, Jai Prakash, and Avinoam Nir (2016). “Effect of added mass on the interaction of bubbles in a low-Reynolds-number shear flow”. In: *Physical Review E* 93.2, p. 023105.

Prakash, Jai, Olga M Lavrenteva, Leonid Byk, and Avinoam Nir (2013). “Interaction of equal-size bubbles in shear flow”. In: *Physical Review E* 87.4, p. 043002.

Brennen, Christopher Earls (2005). *Fundamentals of multiphase flow*. Cambridge university press.

Sadeghi, Keyvan and Atilla Incecik (2005). “Tensor properties of added-mass and damping coefficients”. In: *Journal of engineering mathematics* 52.4, pp. 379–387.

REFERENCES

Sarpkaya, Turgut (1963). “Lift, drag, and added-mass coefficients for a circular cylinder immersed in a time-dependent flow”. In: pp. 13–15.

Sarpkaya, Turgut (1975). “Forces on cylinders and spheres in a sinusoidally oscillating fluid”. In: pp. 32–37.

Friedman, PD and J Katz (2002). “Mean rise rate of droplets in isotropic turbulence”. In: *Physics of Fluids* 14.9, pp. 3059–3073.

Magnaudet, Jacques (1997). “The forces acting on bubbles and rigid particles”. In: *ASME Fluids Engineering Division Summer Meeting, FEDSM*. Vol. 97, pp. 22–26.

Maliska, Clovis R and Emilio E Paladino (2006). “The role of virtual mass, lift and wall lubrication forces in accelerated bubbly flows”. In: *Energy: Production, Distribution and Conservation-Milan* 2006, pp. 953–962.

Mordant, Nicolas, Alice M Crawford, and Eberhard Bodenschatz (2004). “Experimental Lagrangian acceleration probability density function measurement”. In: *Physica D: Nonlinear Phenomena* 193.1-4, pp. 245–251.

Ni, Rui, Shi-Di Huang, and Ke-Qing Xia (2012). “Lagrangian acceleration measurements in convective thermal turbulence”. In: *Journal of fluid mechanics* 692, pp. 395–419.

Pumir, Alain, Eberhard Bodenschatz, and Haitao Xu (2013). “Tetrahedron deformation and alignment of perceived vorticity and strain in a turbulent flow”. In: *Physics of Fluids* 25.3, p. 035101.

REFERENCES

Masuk, AUM, A Salibindla, and Ni R (2020). “Simultaneous measurements of deforming Hinze-scale bubbles with surrounding turbulence”. In: *Journal of Fluid Mechanics* submitted.

Salibindla, Ashwanth K. R., Ashik Ullah Mohammad Masuk, Shiyong Tan, and Rui Ni (2020). “Lift and drag coefficients of deformable bubbles in intense turbulence determined from bubble rise velocity”. In: *Journal of Fluid Mechanics* 894, A20. DOI: 10.1017/jfm.2020.244.

Voth, Greg Anthony (2000). *Lagrangian acceleration measurements in turbulence at large Reynolds numbers*. Cornell University.

Hidalgo, Juan J, Jaime Fe, Luis Cueto-Felgueroso, and Ruben Juanes (2012). “Scaling of convective mixing in porous media”. In: *Physical review letters* 109.26, p. 264503.

Cinar, Yildiray and Amir Riaz (2014). “Carbon dioxide sequestration in saline formations: Part 2â Review of multiphase flow modeling”. In: *Journal of Petroleum Science and Engineering* 124, pp. 381–398.

Ahlers, Guenter, Siegfried Grossmann, and Detlef Lohse (2009). “Heat transfer and large scale dynamics in turbulent Rayleigh-Bénard convection”. In: *Reviews of modern physics* 81.2, p. 503.

Lohse, Detlef and Ke-Qing Xia (2010). “Small-scale properties of turbulent Rayleigh-Bénard convection”. In: *Annual Review of Fluid Mechanics* 42, pp. 335–364.

REFERENCES

Emami-Meybodi, Hamid, Hassan Hassanzadeh, Christopher P Green, and Jonathan Ennis-King (2015). “Convective dissolution of CO 2 in saline aquifers: Progress in modeling and experiments”. In: *International Journal of Greenhouse Gas Control* 40, pp. 238–266.

Meybodi, Hamid Emami and Hassan Hassanzadeh (2013). “Mixing induced by buoyancy-driven flows in porous media”. In: *AIChE Journal* 59.4, pp. 1378–1389.

Neufeld, Jerome A, Marc A Hesse, Amir Riaz, Mark A Hallworth, Hamdi A Tchelepi, and Herbert E Huppert (2010). “Convective dissolution of carbon dioxide in saline aquifers”. In: *Geophysical research letters* 37.22.

Backhaus, Scott, Konstantin Turitsyn, and RE Ecke (2011). “Convective instability and mass transport of diffusion layers in a Hele-Shaw geometry”. In: *Physical Review Letters* 106.10, p. 104501.

Hewitt, DuncanR, JeromeA Neufeld, and JohnR Lister (2014b). “High Rayleigh number convection in a three-dimensional porous medium”. In: *Journal of Fluid Mechanics* 748, p. 879.

Graham, Michael D and Paul H Steen (1994). “Plume formation and resonant bifurcations in porous-media convection”. In: *Journal of Fluid Mechanics* 272, pp. 67–90.

Otero, Jesse, Lubomira A Dontcheva, Hans Johnston, Rodney A Worthing, Alexander Kurganov, Guergana Petrova, and Charles R Doering (2004).

"High-Rayleigh-number convection in a fluid-saturated porous layer". In: *Journal of Fluid Mechanics* 500, pp. 263–281.

Farajzadeh, R, B Meulenbroek, D Daniel, A Riaz, and J Bruining (2013). "An empirical theory for gravitationally unstable flow in porous media". In: *Computational Geosciences* 17.3, pp. 515–527.

Jensen, Jerry L, Larry W Lake, et al. (1988). "The influence of sample size and permeability distribution on heterogeneity measures". In: *SPE Reservoir Engineering* 3.02, pp. 629–637.

Cavanagh, Andrew J and R Stuart Haszeldine (2014). "The Sleipner storage site: Capillary flow modeling of a layered CO 2 plume requires fractured shale barriers within the Utsira Formation". In: *International Journal of Greenhouse Gas Control* 21, pp. 101–112.

Green, Christopher P and Jonathan Ennis-King (2014). "Steady dissolution rate due to convective mixing in anisotropic porous media". In: *Advances in Water Resources* 73, pp. 65–73.

Hewitt, Duncan R, Jerome A Neufeld, and John R Lister (2014a). "High Rayleigh number convection in a porous medium containing a thin low-permeability layer". In: *Journal of Fluid Mechanics* 756, pp. 844–869.

Guerrero-Martínez, Fernando J, Paul L Younger, Nader Karimi, and Sotirios Kyriakis (2017). "Three-dimensional numerical simulations of free convec-

tion in a layered porous enclosure". In: *International Journal of Heat and Mass Transfer* 106, pp. 1005–1013.

Szulczewski, ML, MA Hesse, and R Juanes (2013). "Carbon dioxide dissolution in structural and stratigraphic traps". In: *Journal of Fluid Mechanics* 736, pp. 287–315.

Settles, Gary S (2012). *Schlieren and shadowgraph techniques: visualizing phenomena in transparent media*. Springer Science & Business Media.

Dow (2000). *A Guide to Glycols–Safety Data Sheet*.

Salazar, Juan PLC and Lance R Collins (2009). "Two-particle dispersion in isotropic turbulent flows". In: *Annual review of fluid mechanics* 41, pp. 405–432.

# Appendix A

# The structure of the open-source STB code

In this appendix, we provide a brief summary of the open-source STB code structure that is available on the GitHub repository **Tan:OpenLPT:2020** for public use.

The input to our STB code include time-resolved image sequences of all cameras along with the camera calibration files. The calibration files include camera parameters and optical-transfer functions (OTF), which are acquired separately in MATLAB codes. These calibration parameters are given as input into the STB code via two basic classes named *Camera* and *OTF*, respectively.

In the open-source STB, based on the hierarchy, the highest level of classes that form the backbone of the code is level I. There are three level-I classes that correspond to three major components of the code: particle reconstruction

(*Calibration*), IPR (*IPR*), and STB (*STB*). Note that, all the text that have been italicized henceforth refer to the names of classes, subroutines or functions in the code.

Both *Calibration* and *STB* share four level-II classes to handle image loading (*Tiffload*), 2D particle identification (*Frame*), 3D particle positions (*Position*), and position refinement (*Shaking*). For each frame, images from all four cameras will go through the level-I class *Calibration* for image pre-processing.

In addition to image pre-processing, *Calibration* class also contains three subroutines namely, stereomatching, triangulation, and match pruning, all contained in a function called *Stereomatch*. During stereomatching, 2D points are matched with several possible combinations to find the 3D positions, but not all of these combinations are real. Match pruning only picks the combinations with the minimum triangulation error, and also optimizes the combinations to make sure that every 2D point can only be used in one combination. After match pruning, particle positions are refined in level-II class called *Shaking*. *Shaking* serves two purposes: (i) refines the particle 3D positions, and (ii) removes possible ghost particles that fail the intensity check.

After *Calibration*, the level-I class *IPR* implements the algorithm of iterative particle reconstruction. This class has a loop that iteratively corrects the 3D particle positions by shaking then using the class *Shaking* mentioned above.

The third level-I class named *STB* is the main component of this code. Within *STB*, there are two functions, *InitialPhase* and *ConvergedPhase*. *InitialPhase* only deals with the first four frames of the dataset as these four frames do not have velocity field to make predictions and connect particles to make tracks. *InitialPhase* first calls the class *IPR* to reconstructs 3D particle positions in the first four frames. Particles from the these frames are then fed to a class called *PredictiveField* (level-II), in which a particle-space correlation is conducted to get a velocity field and then connect the particles into tracks based on this field. After that, *ConvergedPhase* takes the short tracks over four frames obtained from *InitialPhase* and extends them to the following frames. The residual particles in each frame that cannot be connected to the existing tracks will be processed through *IPR* to initialize new tracks. A basic class called *Track* is designed to manage track data, including the decisions of terminating a bad track. Finally, the input and output are handled by an interface class called *DataIO*.

# Appendix B

## Permeability of a Hele-shaw and its dependence on the porosity

This appendix provides details on the estimation of bulk permeability ($k$) and permeability of the disc layer ($k_l$) in the Hele-Shaw cell with different configurations. For the homogeneous case, permeability of the cell follows a simple relationship $k = b^2/12$ as a function of the thickness of the cell, $b$. As $b$ is constant throughout the entire cell, $k$ is considered to be uniform. For the heterogeneous case, however, adding discs with the same thickness as the cell width blocks the flow in those area, thereby creating zero permeability regions. Putting those discs in a horizontal layer with small distances $l$ in between creates a layer with low, but nonzero, permeability $k_l < k$, because those gaps between discs can still allow flow to pass.

Both $k$ and $k_l$ can be evaluated from the Darcy's law: $k = \mu u/\nabla p$, where $\mu$

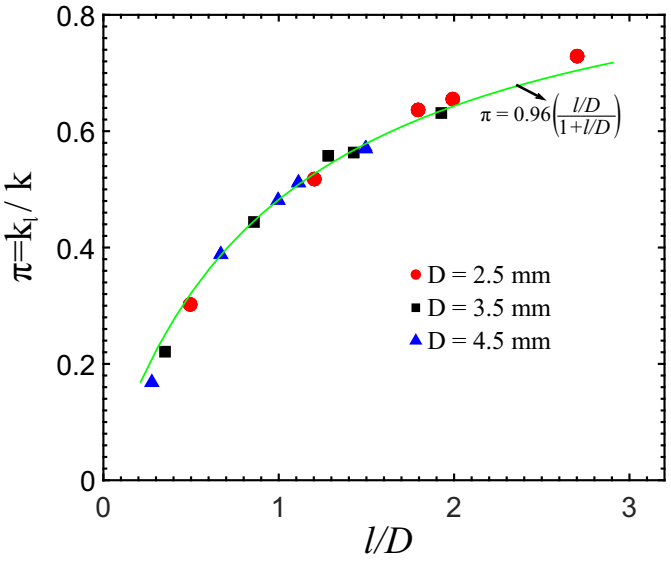


**Figure B.1:** The non-dimensional permeability of the disc layer, $\pi = k_l/k$ versus the non-dimensional length scale imposed by the disc layer ($l/D$) for different disc configurations.

is the fluid viscosity. In theory, we can measure the permeability, providing a constant flow velocity ($u$) and pressure gradient ($\nabla p$). We have attempted such experiment by using the same experimental setup, except only this time the PPG was the only fluid layer that falls under a constant hydrostatic pressure gradient, $\nabla p = \rho_{ppg} g$. However, we quickly realized that this experiment does not provide an idealized situation, as the PPG is in contact with air at two interfaces, thereby allowing the surface tension effects to affect the estimation. So it is difficult to experimentally measure the permeability in a Hele-Shaw cell.

To overcome this problem, we decide to use simulation to estimate the permeability of the single layer. Since the flow is in the Stokes flow limit, the

simulation should give very accurate estimation with relatively small computational cost. For simplicity, we chose to use the commercial CFD software, ANSYS Fluent. The simulations are set up in a 3D domain, exactly matched to the experiments. In order to validate the results obtained from the software, we first conducted the simulation for homogeneous case without discs. The fluid used in these simulations was PPG and it was subjected to a uniform pressure gradient: $\nabla p = \rho_{ppg} g$, ignoring the surface tension effects. It was found that the permeability matches perfectly with the analytic estimation $k = b^2/12$ for the homogeneous case.

After this validation, we then performed the same simulations on the disc layer, $k_l$. The simulations were repeated for different combinations of disc and gap sizes. This disc layer permeability was then normalized by $k$, which gives $\pi = k_l/k$ and eventually $\Omega$. $\pi$ is shown as a function of non-dimensionalized disc parameter $l/D$ in figure B.1. Based on Kozeny-Carman equation (**carman1956flow**), we know that the permeability of the packed bed of solid is related to its porosity. Although our setup is quasi-2D, we still expect the permeability should relate to 1D porosity. Here, $\pi$ for all used configurations can be fitted with a simple linear relationship with $l/(l + D)$, as shown in figure B.1.

Note that $k_1$ is the permeability of the disc layer. If the simulation is extended to the entire cell height with a disc layer inside, the permeability calculated becomes an mean value. As the thickness of the disc layer consists a

small portion of the total height (10 %) in the simulation, the addition of discs was found to affect the bulk permeability $k$ by less than 10 $\%$.

# Vita

---

## Education

| | |
|---|---|
| **Ph.D.**, Mechanical Engineering<br>Johns Hopkins University, Baltimore, MD | July 2020<br>GPA: NA |
| **M.S.**, Mechanical Engineering; Minor in Computational Science<br>The Pennsylvania State University, University Park, PA | May 2017<br>GPA: 3.93/4 |
| **B.Tech.**, School of Mechanical, Material & Energy Engineering<br>Indian Institute of Technology (IIT) Ropar, Punjab, India | May 2013<br>GPA: 8.94/10 |

---

## Technical Skills

High-speed Imaging | Image Processing | Statistical Analysis and Physics-based Modeling | Hands-on Laboratory Experience | Turbulent Flows | Multi-phase Flows | 3D Particle Tracking Velocimetry | 3D Complex Shape Recon-

struction | Photron / Phantom High-speed Cameras | Laser Diagnostics | Thermal and Fluid Engineering | Solar Thermal Systems | Carbon Sequestration | Heat and Mass Transfer | HVAC systems |

**Programming Languages:** C++, MATLAB, Python, R

**Softwares:** Simulink, SolidWorks, LabVIEW, Ansys Fluent, Abacus, AutoCAD, Minitab, Mathcad, Github, LaTeX

---

## KEY COURSE PROJECTS

1. Power train systems modeling & simulation of a McLaren F1 using Simulink.
2. Performed finite volume analysis to study the convective cooling of a PDIP28 integrated circuit.
3. Improved the efficiency of a solar-run absorption refrigerator by incorporating nano-particles into the fluid.
4. Designed and manufactured a fighting bot that won second place at IIT Bombay Robowars competition.

---

VITA

## PEER REVIEWED JOURNAL AND CONFERENCE PUBLICATIONS

- **Ashwanth Salibindla**, Ashik Ullah Mohammad Masuk, and Rui Ni. "Experimental investigation of the added mass force of deformable bubbles in intense turbulence." Journal of Fluid Mechanics - *Under review*

- **Ashwanth Salibindla**, Ashik Ullah Mohammad Masuk, Shiyong Tan, and Rui Ni. "Lift and drag coefficients of deformable bubbles in intense turbulence determined from bubble rise velocity." Journal of Fluid Mechanics 894 (2020).

- **Ashwanth Salibindla**, Rabin Subedi, Victor C. Shen, Ashik Ullah Mohammad Masuk, and Rui Ni. "Dissolution-driven convection in a heterogeneous porous medium." Journal of Fluid Mechanics 857 (2018): 61-79.

- Ashik Ullah Mohammad Masuk, **Ashwanth Salibindla**, Shiyong Tan, and Rui Ni. "V-ONSET (Vertical Octagonal Noncorrosive Stirred Energetic Turbulence): A vertical water tunnel with a large energy dissipation rate to study bubble/droplet deformation and breakup in strong turbulence." Review of Scientific Instruments 90, no. 8 (2019): 085105.

- Ashik Ullah Mohammad Masuk, **Ashwanth Salibindla**, and Rui Ni. "A robust virtual-camera 3D shape reconstruction of deforming bubbles/droplets with additional physical constraints." International Journal of Multiphase

Flow 120 (2019): 103088.

- Tan, Shiyong, **Ashwanth Salibindla**, Ashik Ullah Mohammad Masuk, and Rui Ni. “Introducing OpenLPT: new method of removing ghost particles and high-concentration particle shadow tracking.” Experiments in Fluids 61, no. 2 (2020): 47.

- Rahul Gulati, **Ashwanth Salibindla**, Vikrant Khullar, Vishal Bhalla, Himanshu Tyagi, Yuebin Zhao, Edward Law, and Robert A. Taylor. “ ”Enhancing the efficiency of absorption refrigeration cycle by ‘seeding’nanoparticles directly in the working fluid.” International journal of environmental studies 70, no. 5 (2013): 808-823

- Shiyong Tan, **Ashwanth Salibindla**, Ashik Ullah Mohammad Masuk, and Rui Ni. ”An open-source shake-the-box method and its performance evaluation.” In 13th international symposium on particle image velocimetry. 2019..

---

## SELECTED CONFERENCE AND SYMPOSIUM PRESENTATIONS

- **Ashwanth Salibindla**, Ashik Ullah Mohammad Masuk, Rui Ni, “How Fast Do Bubbles Rise in High Energy Turbulence?”, National Energy

VITA

Technology Lab, Multiphase Flow Science Workshop (2019)

- **Ashwanth Salibindla**, Ashik Ullah Mohammad Masuk, Rui Ni, "Bubble rise velocity in strong turbulence", Center for Environmental and Applied Fluid Mechanics - Burgers (2019)

- **Ashwanth Salibindla**, Ashik Ullah Mohammad Masuk, Rui Ni, "Interfacial mass transfer in a turbulent multiphase flow" American Physical Society - Division of Fluid Dynamics (2018).

- **Ashwanth Salibindla**, Ashik Ullah Mohammad Masuk, Rui Ni, "V-ONSET: Introducing turbulent multiphase flow facility focusing on Lagrangian interfacial transfer dynamics" American Physical Society - Division of Fluid Dynamics (2017).